ABSTRACT

Title of Document: COLLISIONAL QUENCHING DYNAMICS AND REACTIVITY OF HIGHLY VIBRATIONALLY EXCITED MOLECULES

Qingnan Liu, Doctor of Philosophy, 2008

Directed By: Professor Amy S. Mullin, Department of Chemistry and Biochemistry

Highly excited molecules are of great importance in many areas of chemistry including photochemistry. The dynamics of highly excited molecules are affected by the intermolecular and intramolecular energy flow between many different kinds of motions. This thesis reports investigations of the collisional quenching and reactivity of highly excited molecules aimed at understanding the dynamics of highly excited molecules. There are several important questions that are addressed. How do molecules behave in collisions with a bath gas? How do the energy distributions evolve in time? How is the energy partitioned for both the donor and bath molecules after collisions? How do molecule structure, molecule state density and intermolecular potential play the role during collisional energy transfer? To answer these questions, collisional quenching dynamics and reactivity of highly vibrationally excited azabenzene molecules have been studied using high resolution transient IR absorption spectroscopy. The first study shows that the alkylated pyridine molecules

that have been excited with E_{vib}~38,800 cm^{-1} impart less rotational and translational energy to CO_2 than pyridine does. Comparison between the alkylated donors shows that the strong collisions are reduced for donors with longer alkyl chains by lowering the average energy per mode but longer alkyl chain have increased flexibility and higher state densities that enhance energy loss via strong collisions. In the second study, the role of hydrogen bonding interactions is explored in collision of vibrationally excited pyridines with H_2O. Substantial difference in the rotational energy of H_2O is correlated with the structure of the global energy minimum. A torque-inducing mechanism is proposed that involves directed movement of H_2O between σ and π-hydrogen bonding interactions with the pyridine donors. In the third study the dynamics of strong and weak collisions for highly vibrationally excited methylated pyridine molecules with HOD are reported. Lower limits to the overall collision rate are directly determined from experimental measurements and compared to Lennard-Jones models which underestimate the collision rate for highly vibrationally excited azabenzenes with HOD. The fourth study explores reactive collisions of highly vibrationally excited pyridine molecules. D-atom abstraction reactions of highly vibrationally excited pyridine-d_5 molecules and chlorine radical show a rate enhancement of ~90 relative to the reaction of room temperature pyridine-d_5 with chlorine radical. A single quantum of C-D stretching vibration is observed to be used for the vibrational driven reaction. Reactions of 2-picoline-d_3 with chlorine radical do not show a similar enhancement. For this case, the fast rotation of $–CD_3$ group in highly vibrationally excited 2-picoline-d_3 inhibits the D-atom abstraction.

COLLISIONAL QUENCHING DYNAMICS AND REACTIVITY OF HIGHLY VIBRATIONALLY EXCITED MOLECULES

By

Qingnan Liu

Dissertation submitted to the Faculty of the Graduate School of the
University of Maryland, College Park, in partial fulfillment
of the requirements for the degree of
Doctor of Philosophy
2008

Advisory Committee:
Professor Amy S. Mullin, Chair
Professor Millard H. Alexander
Professor Michael A. Coplan
Professor Robert A. Walker
Professor Michael R. Zachariah

Acknowledgements

I would consider myself fortunate to being working under the guidance of my advisor, Professor Amy Mullin. Her enthusiasm and creativity in problem solving are inspirational. The challenges, supports, and encouragements from her over the past several years make this doctoral thesis possible. All the experiences in the lab will benefit the rest of my career.

I would also like to express my thanks to Dr. Liwei Yuan, Dr. Daniel Havey, and Dr. Ziman Li. Dr. Liwei Yuan and I systematically investigated the chlorine radical reactions. She has been extremely hard working. Her intelligence and diligence helped us getting through all the obstacles in the experiment. Chapter 6 would not exist without her help. Dr. Daniel Havey and I set up the F-center Spectrometer from scratch. He has been a fantastic science mentor to me. Our work on H_2O and HOD scattering experiments make Chapter 4 and Chapter 5 possible in this thesis. Dr. Ziman Li taught me when I first joined the lab and we set up the diode laser spectrometer to study CO_2 scattering experiment, which makes Chapter 3 in this thesis. I also got a lot of help from her during the start of the chlorine radical reaction experiments.

I want to express my thanks to all the former and present Mullin Group members, Professor Shizuka Hsieh, Juan Du, Samuel Teitlebaum, Elisa Miller, Nicholas Bennette, Mitchell Hayes and Felix Lin. I learned a lot from them in the lab.

I also want to thank Professor Millard Alexander and Dr. Jacek Klos for helping me with normal mode analysis for some molecules in Chapter 3.

Finally, I want to thank all the people around me, my families, my teachers and my friends, though they do not receive specific delineation in the acknowledgement here, I would like to express my appreciation from the bottom of my heart for their encouragements and supports.

Table of Contents

List of Tables

List of Figures

Abbreviations

A	rotational constant
α	absorption strength
AC	alternating current
B	rotational constant
c	speed of light
C	rotational constant
Cl	Chlorine
cm	centimeter
cm^{-1}	wavenumber
CO_2	carbon dioxide
cw	continuous wave
DC	direct current
DCl	deuterium chloride
D_2O	deuterium oxide
ΔE	energy change
E_a	activation energy
E_{rot}	rotational energy
E_{trans}	translational energy
E_{vib}	vibrational energy
ε	Lennard-Jones well depth
FWHM	full width at half maximum
HCl	hydrogen chloride
H_2O	water
HOD	hydrogen deuterium oxide
InSb	indium antimonide
IR	infrared
J	total angular momentum quantum number
K	Kelvin

k^{int}	integrated energy transfer rate constant
k_2^J	second order rate constant
K_a	limiting oblate top quantum number
k_B	Boltzmann constant
K_c	limiting prolate top quantum number
k_{LJ}	Lennard-Jones collision rate constant
ℓ	path length
LJ	Lennard-Jones
λ	wavelength
m	meter
mol	mole
μs	microsecond
μm	micrometer
MW	megawatt
ν	vibrational frequency
Nd	Neodymium
ns	nanosecond
p	pressure
P	probability
R	ideal gas constant
RT	rotation and translation
ρ_s	vibrational state density
S_0	electronic ground state
S_1	first excited singlet electronic state
S_2	second excited singlet electronic state
σ	Lennard-Jones diameter
s	second
t	time
T_0	initial temperature
T_1	first excited triplet electronic state

T_{rot}	rotational temperature
T_{trans}	translational temperature
UV	ultraviolet
v	velocity
V→V	vibration to vibration
V→RT	vibration to rotation and translation
YAG	yttrium aluminum garnet

Chapter 1: Introduction to Collisional Quenching Dynamics and Reactivity of Highly Vibrationally Excited Molecules

1.1 The Significance of Collisional Energy Transfer

Collisional energy transfer is of great importance in a variety of chemical systems, such as combustion processes, atmosphere chemistry, chemical lasers and unimolecular decomposition reactions.[1-3] It is well known that molecules with large amounts of internal energy typically have larger reaction rates than cool molecules. This observation is embodied in the Arrhenius equation that describes the temperature dependence of reaction rate constants. In 1922, Lindemann recognized that inelastic collisions play a key role in the mechanism of unimolecular decomposition. This thesis addresses the role of collisions on the chemistry of highly excited molecules.

The role of collisions in unimolecular reactions is described by the Lindemann-Hinshelwood model.[4] In a unimolecular reaction, collisions can activate a cold reactant, deactivate an excited intermediate or stabilize an energetic product. In a unimolecular reaction where A is transformed to B in the absence of collisions, the observed reaction rate is expressed using Eq. 1.1.

$$\text{rate} = k_{obs} \times [A] \qquad \text{(Eq. 1.1)}$$

where k_{obs} is the observed unimolecular reaction rate constant and [A] is the concentration of reactant A. In the presence of collisions, simple first order kinetics

are no longer observed. In the Lindemann-Hinshelwood model, reactant A becomes excited to A* through collisions with M,

$$A + M \xrightarrow{k_1} A^* + M \,. \qquad \text{(Eq. 1.2)}$$

The appearance of A* is given by

$$\frac{d[A^*]}{dt} = k_1[A][M] \,. \qquad \text{(Eq. 1.3)}$$

Excited A* can either be deactivated through collisions with M,

$$A^* + M \xrightarrow{k_{-1}} A + M \,, \qquad \text{(Eq. 1.4)}$$

or A* can react to form the product B,

$$A^* \xrightarrow{k_2} B \,. \qquad \text{(Eq. 1.5)}$$

The deactivation and reaction rates are given by Eq. 1.6 and Eq. 1.7.

$$\frac{d[A^*]}{dt} = -k_{-1}[A^*][M] \qquad \text{(Eq. 1.6)}$$

$$\frac{d[A^*]}{dt} = -k_2[A^*] = -\frac{d[B]}{dt} \qquad \text{(Eq. 1.7)}$$

Apply the steady state approximation to the formation of A* and this gives Eq. 1.8 for the overall process.

$$\frac{d[B]}{dt} = \frac{k_1 k_2 [A][M]}{k_{-1}[M] + k_2} \qquad \text{(Eq. 1.8)}$$

At low pressures, Eq. 1.2 is the rate determining step and the reaction follows 2nd order kinetics. At high pressures, the collisional activation and deactivation come into a rapid equilibrium. In this case, Eq. 1.5 is the rate limiting step and the observed kinetics are 1st order.

The example given above shows that collisional deactivation competes with reactivity in highly excited molecules. There are a number of important questions about collisions of molecules that remain unanswered. What are the dominate energy transfer pathways in molecular collisions? How is the energy partitioned in the two molecules after the collision? How does the complexity of the excited molecules affect collisional deactivation and chemical reactions? How much vibrational energy is available for chemistry in reactive collisions?

The goal of this thesis is to investigate how activated molecules lose energy through collisions and use energy in bimolecular chemical reactions. In these studies, high resolution transient IR absorption spectroscopy is used to characterize the collision products. The partitioning of energy between vibrational, rotational and translational degrees of freedom reveals information about the mechanism of energy transfer and absolute rates show which pathways are most effective at energy transfer.

These data provide a detailed picture of energy flow during collisions of highly excited molecules.

1.2 Methods to Study Collisional Quenching

A number of experimental approaches have been used to investigate collisional quenching of highly excited molecules. Some experimental methods directly monitor energy loss of a donor molecule. These techniques include time-resolved infrared fluorescence (IRF),[5-7] ultraviolet absorbance (UVA),[8,9] Fourier transform infrared (FTIR) emission,[10] molecular beam imaging,[11-13] and kinetically controlled selective ionization (KCSI).[14-17] An alternate approach is to measure energy gain of bath molecules following collisions. This latter category includes the state-resolved transient IR probing technique that is used in this thesis.

Currently, determination of the energy transfer distribution function is of great interest. The energy transfer distribution function describes the probability that a highly excited donor molecule loses energy ΔE after collisions with bath molecules. There are several techniques to get this information, including KCSI, molecular beam imaging and state-resolved transient IR probing. Using two-color two-photon ionization, the KCSI approach directly monitors highly vibrationally excited donor molecules as they are relaxed by collisions. Distributions of highly vibrationally excited molecules with initial energy E are monitored as they pass through experimentally determined energy windows at an energy E'.[14,18-20] The molecular beam imaging technique measures the velocity mapping of scattered molecules, which corresponds to the energy mapping of scattered molecules, to measure the energy transfer distribution function.[11-13] State-resolved transient IR spectroscopy

provides information on energy partitioning for the scattered bath molecules after collisions with highly vibrationally excited donor molecules. By measuring the nascent Doppler-broadened linewidths of single ro-vibrational transitions, the translational energy distributions of scattered molecules in individual ro-vibrational states is measured. The energy transfer distribution function is obtained by combining state-resolved energy distribution data with absolute energy transfer rate measurements for individual ro-vibrational states. Previous studies using high resolution transient IR spectroscopy have focused on the strong collisions of a number of highly vibrationally excited molecules which impart large amounts of rotational and translational energy to bath molecules.[21-24] These earlier studies provided information on the high energy tail of the energy transfer distribution function. In this thesis, a novel method is described and utilized to measure the weak collisions with small amount of energy transferred. This enables us to directly measure the full energy transfer distribution function in addition to gaining insight into the energy transfer dynamics from a state-resolved perspective.

There are a number of theoretical studies that have investigated the collisional quenching of highly excited molecules. Hinshelwood assumed that every collision deactivated an excited reactant so that the collision rate was used for k_{-1} in Eq. 1.4. In reality, the strong collision assumption overestimates the quenching efficiency of deactivation collisions. Weak collisional relaxation has been described by Rabinovitch[25-28] and Troe[29] with semi-empirical master equation theories using microcanonical transition state theory. The ergodic collision theory (ECT) given by Nordholm is based on the idea that a collision leads to a complete redistribution of the

initial excitation into all of the degrees of freedom available to a collision complex.[30-32] This approach was able to reproduce qualitative trends seen in experiments but did not lead to quantitative agreement. Recently, a semiempirical extension of ECT, called the partially ergodic collision theory (PECT), has obtained improved agreement with experiments by allowing only a subset of donor and bath degrees of freedom to be involved in the energy redistribution.[33-35] Gilbert and coworkers used a biased random-walk model to describe energy transfer from large molecules. Classical trajectory calculations have also been used for studying collisional energy transfer,[36-40] for both excited polyatomic molecules with inert atomic gases[41-54] and excited polyatomic molecules with diatomic and polyatomic bath molecules.[17,44,55-60]

This thesis includes two types of experimental investigations: studies of collisional quenching dynamics to understand how a molecule's complexity and electron distribution impacts collisional relaxation and studies of reaction dynamics to explore the role of vibrational energy in reactions of highly excited molecules.

1.3 Molecules Chosen in this Study

The highly excited molecules studied in this thesis are prepared with pulsed UV laser absorption. To study the collisional relaxation and reactivity of highly vibrationally excited azabenzene molecules, it is essential that the photo-physics of these molecules is well characterized. Highly vibrationally excited donor molecules are prepared using nanosecond laser excitation. This procedure generally occurs as follows. Room temperature donor molecules in the gas phase absorb 266 nm UV photons and are excited to an electronically excited state. Following radiationless decay under collision free conditions, donor molecules relax to the electronic ground

state, leaving the molecule in a highly vibrationally excited state. For the molecules under investigation, the radiationless decay process typically has a lifetime of τ=5 ps to 100 ns.

Here the photo-physics of pyridine is used as an example to demonstrate how highly vibrationally excited azabenzene molecules are produced. Pyridine molecules are electronically excited to the first excited singlet state (S_1) by single photon absorption of 266 nm light. Over 99% of the excited pyridine molecules internally convert to the electronic ground state (S_0) with a lifetime of 60 ps, resulting in pyridine molecules with a vibrational energy of E_{vib}=37,920 cm^{-1}. Fewer than 1% of the pyridine molecules go through the triplet state (T_1) with an intersystem crossing process in 50 ps and then to electronic ground state (S_0) in less than 100 ns.[61-63] Samples with typical pressure of ~20 mTorr have an average collision time of τ_{col}~4 μs. State-resolved transient IR probing of collisional energy transfer is then recorded at 1 μs after UV excitation. Relative to the μs time scale, the highly vibrationally excited donor molecules are prepared at t=0. The donor molecules have very small fluorescence quantum yields, less than 1%, and in cases where photodissociation can occur, the outcome of collisions is probed well before any decomposition occurs. The azabenzene molecules studied in this thesis included 2-ethyl-pyridine (2EP), 2-propyl-pyridine (2PP), pyridine-h_5, pyridine-d_5, pentafluoro-pyridine (pyridine-f_5), pyrazine, 2-methyl-pyridine (2MP or 2-picoline), 2,6-dimethyl-pyridine (2,6-lutidine) and 2-methyl-d_3-pyridine (2-picoline-d_3). Structures of these molecules are shown in Figure 1.1. The photo-physics of each will be discussed individually in the relevant chapters.

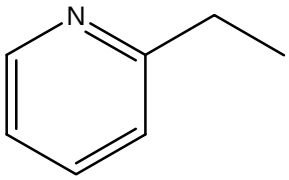

2-ethyl-pyridine

(2EP)

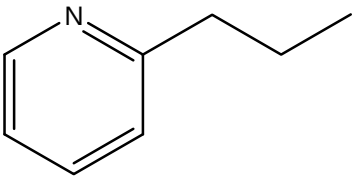

2-propyl-pyridine

(2PP)

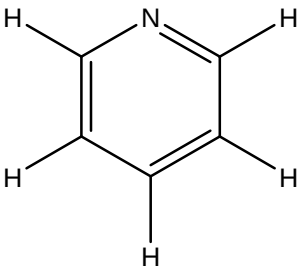

pyridine-h_5

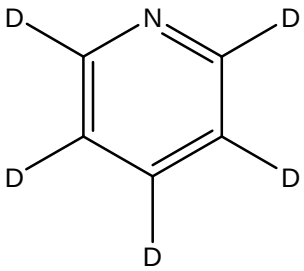

pyridine-d_5

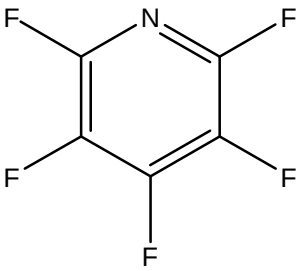

pentafluoropyridine

(pyridine-f_5)

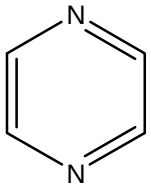

pyrazine

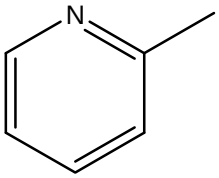

2-methyl-pyridine

(2MP or 2-picoline)

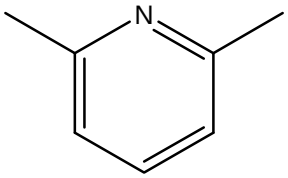

2,6-dimethyl-pyridine

(2,6-lutidine)

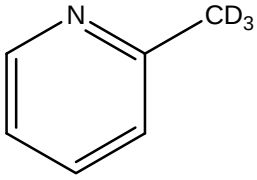

2-methyl-d_3-pyridine

(2-picoline-d_3)

Figure 1.1. Azabenzene molecules studied in this work.

1.4 Overview of the Work in this Dissertation

This thesis addresses a number of questions regarding the nature of collisions involving highly excited molecules. How does the structure of highly excited molecules influence the collisional quenching dynamics? How do donor vibrational mode frequencies and state density play the role during collisional quenching? Is there evidence that intermolecular forces affect collisional energy transfer? How do the quenching dynamics depend on the identity of the gas? Is the Lennard-Jones collision model a good description of intermolecular potentials for polyatomic molecules? How does the reactant vibrational energy contribute to chemical reactions? With these questions in mind, the dynamics of collisional quenching and reactivity of highly vibrationally excited molecules have been investigated using high resolution state-resolved transient IR spectroscopy. A number of collision systems were chosen to investigate the effects of molecular structure, molecular state density and intermolecular potentials during collisional energy transfer. The effect of vibrational energy on chemical reactions was also studied.

The remaining chapters of this thesis are organized as follows:

● Chapter 2 describes the experimental setup of the high resolution transient IR absorption spectrometers.

● In Chapter 3, the effect of flexibility in collision of alkylated pyridine molecules with CO_2 is explored. The collisional energy transfer dynamics of highly vibrationally excited pyridine (E_{vib}=37,920 cm^{-1}), 2-methyl-pyridine (E_{vib}=38,313 cm^{-1}), 2-ethyl-pyridine (E_{vib}=38,568 cm^{-1}) and 2-propl-pyridine (E_{vib}=38,867 cm^{-1}) with CO_2 are investigated. It is found that for the strong collisions, the alkylated donors

impart less rotational and translational energy to CO_2 than pyridine does. Two competing processes are discussed: strong collisions are reduced for donors with longer alkyl chains by lowering the average energy per mode but longer alkyl chain have increased flexibility and higher state densities that enhance energy loss via strong collisions.

● Chapter 4 explores the role of preferential hydrogen bonding interactions in strong collisional energy transfer dynamics. The collisional energy transfer dynamics of highly vibrationally excited pyridine-h_5 (E_{vib}=37,920 cm^{-1}), pyridine-d_5 (E_{vib}=38,068 cm^{-1}) and pentafluoro-pyridine (pyridine-f_5) (E_{vib}=38,836 cm^{-1}) with H_2O are studied. These collision pairs have different structures for local minima in their intermolecular potentials due to different electron distributions. Nearly identical energy partitioning is observed for H_2O molecules scattered from pyridine-h_5 and pyridine-d_5, while substantially less rotational energy is found in H_2O scattered from pyridine-f_5. A torque-inducing catapult mechanism is proposed that involves directed movement of water between σ and π-hydrogen bonding interactions with the pyridine donors. The experimental results are consistent with this mechanism, and with effects due to the state-density energy dependence of the highly excited donor molecules.

● Chapter 5 describes the first IR absorption measurements of the full energy transfer distribution functions for the collisional quenching of hot donor molecules. The outcome of strong and weak collisional energy transfer of highly vibrationally excited pyrazine (E_{vib}=37,900 cm^{-1}), 2-methyl-pyridine (2-picoline, E_{vib}=38,313 cm^{-1}) and 2,6-dimethyl-pyridine (2,6-lutidine, E_{vib}=38,702 cm^{-1}) with HOD is presented and compared. Lower limits to the overall collision rates are directly determined from

experimental measurements and compared to Lennard-Jones models. It is found that the Lennard-Jones model underestimates the collision rate for highly vibrationally excited azabenzenes with HOD.

● In Chapter 6, the role of vibrational energy in chemical reactions of highly vibrationally excited molecules is explored. The reaction dynamics of highly vibrationally excited pyridine-d_5 (E_{vib}=38,068 cm^{-1}) and 2-methyl-d_3-pyridine (2-picoline-d_3, E_{vib}=38,328 cm^{-1}) with chlorine radical is reported. A rate enhancement of ~90 has been observed for the reaction of highly vibrationally excited pyridine-d_5 and chlorine radical relative to room temperature pyridine-d_5 reactions. The results show that energy equal to a single quantum of C-D stretch is used for the D-atom abstraction reaction. For reactions of 2-picoline-d_3 with chlorine radical, vibrational energy in the reactant inhibits the D-abstraction reactions that lead to DCl (v=0) products. The results indicate that free-rotor motion in the highly vibrationally excited molecule reduces the likelihood of a direct reaction via a linear transition state.

Chapter 2: Experimental Methods

2.1 Introduction

High resolution transient IR absorption spectroscopy has been used to study the inelastic and reactive collisions of highly vibrationally excited azabenzene molecules. In these experiments, highly vibrationally excited azabenzene molecules are prepared using optical excitation by UV light from a pulsed Nd:YAG laser. The high resolution probing of scattered bath molecules or reaction product involves different lasers, depending on the IR absorption spectra of the collision partner or reaction product. Diode lasers operating at λ~4.3-4.5 μm are used to measure scattered CO_2 and DCl molecules. A high resolution F-center laser with output at λ~2.7 μm is used to probe H_2O and HOD molecules. A general description of the diode laser, F-center laser and Nd:YAG laser is given in Sections 2.2, 2.3 and 2.4, respectively. The techniques used in high resolution transient absorption spectroscopy are explained in detail in Sections 2.5 and 2.6.

2.2 Diode Laser

Commercial mid-IR diode lasers were used to measure dynamics of CO_2 collisions and reactions that form DCl. Mid-IR diode laser are formed by doping a very thin layer of semiconductor materials on the surface of a crystal wafer. The crystal is doped to produce an n-type region and a p-type region, one above the other, resulting in a p-n junction, or diode. When current is applied to the diode, electrons transfer from the n-type region to the p-type region while electron holes transfer in

the opposite direction. The relaxation of electrons and holes occurs by stimulated emission. The frequency of the emitted photon is determined by the electron and hole state. By applying a ramp current on the diode laser, a tunable output spectrum is obtained. Single frequency output was realized in these studies by reducing the amplitude of the ramp current to a narrow spectral region of a desired probe transition. Active feedback stabilization was used to control the output frequency of the laser. Trace amounts of second mode output were minimized by saturating a reference gas transition, measuring the amount of the light transmitted to the detector and adjusting the temperature and current settings of the diode laser.

The output of the diode laser was typically less than 1 mW, with a frequency resolution of 0.0003 cm^{-1}. Several diode lasers were used for the studies described in this thesis. CO_2 ($00^01 \leftarrow 00^00$) transitions at 2300 cm^{-1} were probed at $\lambda \sim 4.3$ μm in Chapter 3. DCl (v=1←v=0) and DCl (v=2←v=1) transitions at 2100 cm^{-1} were probed at $\lambda \sim 4.5$ μm in Chapter 6.

2.3 F-center Laser

An F-center laser was used to probe H_2O and HOD. The F-center laser is a solid state laser which uses an alkali halide crystal containing F_2^+ lattice defects (such as, Li-doped KCl) as the gain medium. This type of defect occurs where two adjacent anion vacancies share one electron. An excited state of the F_2^+ center is reached by a $\lambda \sim 650$ nm pump source, such as a Kr-ion laser. Emission at $\lambda = 2.7\text{-}3.3$ μm takes place after lattice relaxation for typical F-center crystals. The emission of the F-center crystal is broad because there are numerous lattice vibrations that couple to the transition. One advantage of the F-center laser over the diode laser for transient

absorption studies is its broad tuning range. Addition of a scanning etalon and rotating CaF_2 plates allow single mode tuning over a range of 0.07 cm^{-1}.[64]

The single-mode tunable F-center laser was used to probe individual rotational states corresponding to H_2O and HOD (001←000) and (011←010) transitions as described in Chapter 4 and Chapter 5. The resolution of a single mode F-center laser is was 0.0003 cm^{-1}. A guide to operating the F-center laser is provided in Appendix A.

2.4 Nd:YAG laser

The pump laser in these studies is a Nd:YAG laser that uses a neodymium-doped yttrium aluminium garnet crystal to obtain lasing at λ=1064 nm. Population inversion is achieved using a flash lamp to excite the energy levels of the crystal, which is a 4-level system. The fundamental output frequency is determined by the energy levels of the neodymium-doped yttrium aluminium garnet crystal. A Q-switch is used to generate pulsed output with pulse duration of 5 ns. This optical switch allows lasing to occur when a maximum population inversion has been reached. The Nd:YAG laser is operated at a repetition of 10 Hz. The output power of the fundamental is ~1200 mJ/pulse. A doubling crystal is used to obtain the 2nd harmonic output at λ=532 nm with a peak power of ~500 mJ/pulse. A 4th harmonic crystal is used to generate light at λ=266 nm with a peak power ~120 mJ/pulse.

Pulsed output at λ=266 nm was used to optically excite azabenzene molecules. In D-atom abstraction reaction experiment, the 532 nm output was split into two components. One half was sent to the 4th harmonic crystal to generate 266 nm light, while the other half was mixed with 1064 nm IR in a 3rd harmonic mixing

crystal to generate λ=355 nm light. Both the 266 nm and 355 nm UV are linearly polarized. Chlorine radicals generated by photodissociation of Cl_2 do not have an isotropic velocity distribution. This issue is addressed in Chapter 6. To minimize the effects of this anisotropy, the 355 nm light was sent through a quarter wave plate to make it circularly polarized prior to Cl_2 photo-dissociation.

2.5 Diode Laser Spectrometer

A high-resolution diode laser spectrometer was used to study the collision dynamics of CO_2 with highly vibrationally excited azabenzene molecules. A schematic is shown in Figure 2.1. 90% of the IR beam passed through a 3 meter sample cell, containing a 1:1 mixture of azabenzene:gas bath. The remaining 10% was directed through a 2 meter reference cell containing vapor of the probe molecule. Typical cell pressures were 20 mTorr with an average collision time of τ_{col}~4 μs.

The diode laser output was locked to the center of a transition of bath gas in the reference cell. Transient fractional absorption signals were measured following the UV excitation pulse and the 1 μs value was used for data analysis. The relative populations of individual rotational states of the scattered bath molecules provide a measurement of the partitioning of energy in the bath gas after collisional quenching. To measure these distributions, a relative measurement technique was used to minimize the long-term change of experimental conditions such as fluctuations of the laser power and gas pressure. The method involves measuring individual product states relative to a chosen reference state to get relative populations of the two states. Translational energy partitioning was obtained by measuring the Doppler-broadened line profiles of individual ro-vibrational states for the scattered bath molecules or

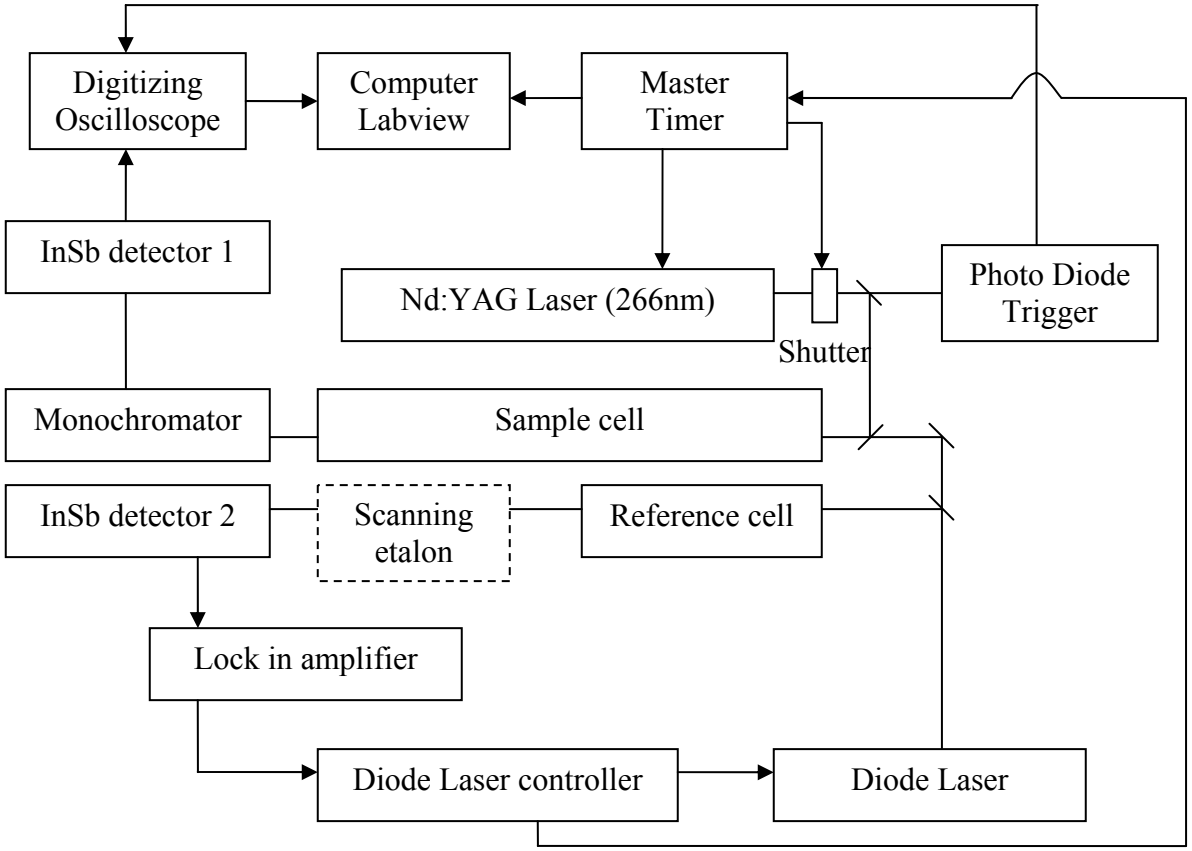

Figure 2.1. Diode Laser Spectrometer

reaction products. This measurement was performed by scanning the single frequency laser across a spectral transition. The diode laser was locked to an etalon fringe and the etalon was tuned by applying a voltage to it. In each frequency step, the time-dependent fractional IR absorption signal was recorded, thereby mapping out the nascent Doppler-broadened line profile. A master timer based on the diode laser modulation was used to synchronize the timing of the Nd:YAG laser and the diode laser. A shutter was used to reduce the 10 Hz UV output to 1 Hz in order to give the flowing gas collision cell enough time to refresh thereby preventing multiple excitation pulses on the sample.

Transient IR absorption data were collected on a digital oscilloscope controlled by a Labview program. The fractional absorption was collected as a function of time after a trigger from the pulsed UV light. The real-time fractional absorption for individual ro-vibrational states was obtained by collecting transient signals on two oscilloscope channels: one coupled with AC and the other coupled with DC. The ratio of these signals was used to determine the fractional absorption following each UV pulse. The fractional signal AC/DC(t) is related to fractional absorption $\Delta I/I_0(t)$ by Eq. 2.1.

$$\frac{\Delta I}{I_0}(t) = \frac{AC/DC(t)}{1 + AC/DC(t)} \qquad \text{(Eq. 2.1)}$$

The change in fractional absorption corresponds to the population change in product molecules.

2.6 F-center Laser Spectrometer

The F-center laser spectrometer is similar to the diode laser spectrometer, but operates at wavelength of ~2.45 to ~3.25 μm. This instrument was used to probe the following states, H_2O (001←000) and HOD (001←000). Several H_2O hot bands such as (011←010) were also probed in this region.

As shown in Figure 2.2, several diagnostics were added into the F-center spectrometer to help study the collisional quenching dynamics. 10% of the output IR beam from the F-center laser was sent to a photodiode to lock to a single cavity mode of the laser. Another 10% of the beam was sent to a scanning Fabry-Perot etalon to monitor the mode quality. The remaining IR beam could be directed to a wavemeter to read the actual frequency output from the F-center laser as needed. The wavemeter was removed during the transient IR absorption measurements. A fixed length confocal etalon (a pair of curved high reflectors separated by 51 cm with a free spectral range of 0.0049 cm^{-1}) was used to calibrate the laser tuning. 10% of the IR beam was sent to an InSb detector in order to compensate for power fluctuations in the IR laser output. The fractional absorption signal was corrected for the IR power fluctuations with the Labview program. 10% of the beam was sent to a reference cell in order to lock to a transition when measuring rotational distributions and energy transfer rates. The remainder of the IR beam was sent to the sample cell, where the time dependent fractional absorption was measured to investigate the collision dynamics.

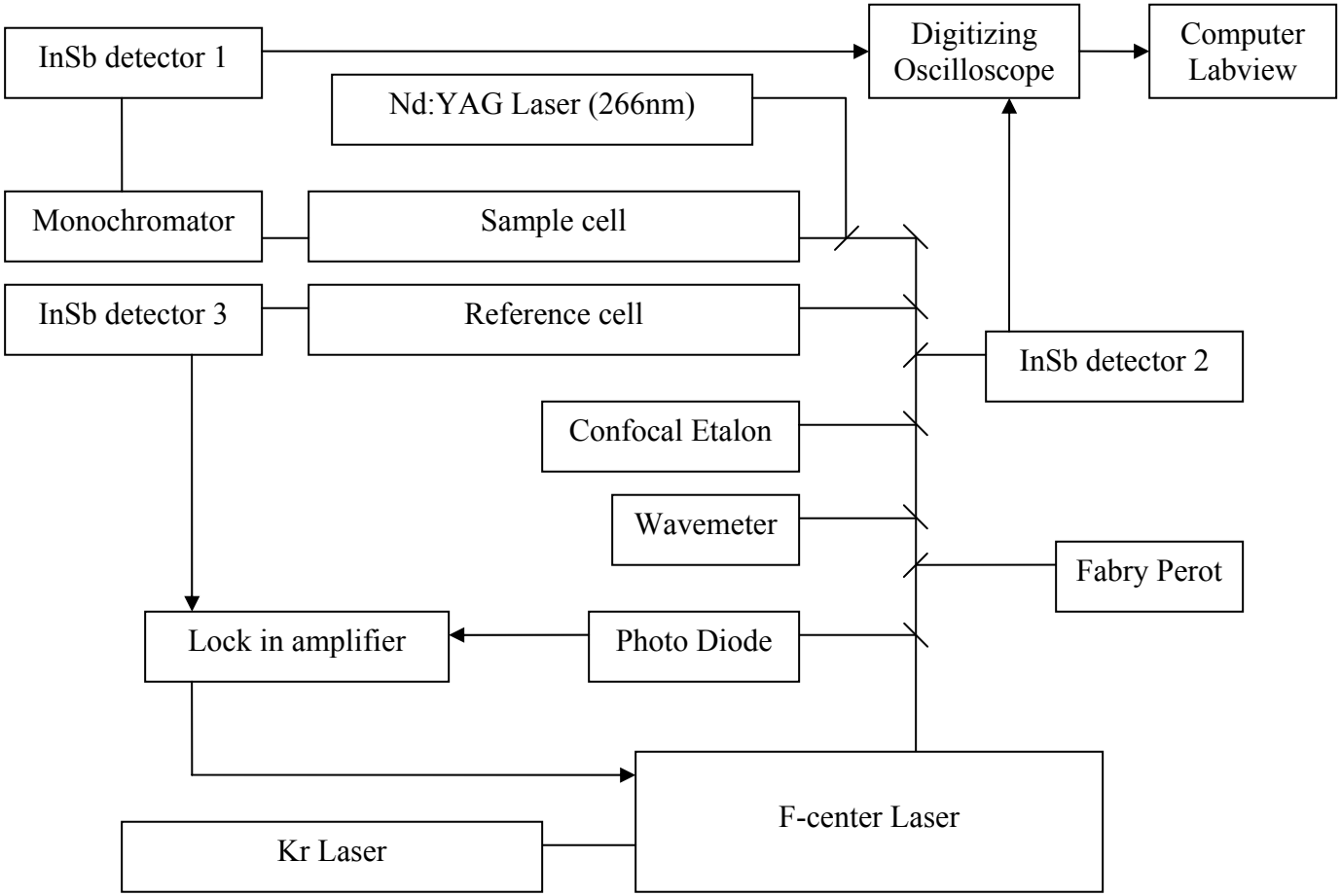

Figure 2.2. F-center Laser Spectrometer

Chapter 3: Alkylation Effects on Strong Collisions of Highly Vibrationally Excited Alkylated Pyridines (E_{vib}~38,800 cm^{-1}) with CO_2

3.1 Introduction

Alkane-containing hydrocarbons are primary constituents of combustion fuels and their chemistry under high temperature conditions is determined in part by reactivity and in part by their collisional behavior.[65] In gas phase chemical kinetics studies using master equation models over multiple interconnected potential wells, Fernandez-Ramos *et al.* showed that rate coefficients for thermal dissociation and recombination reactions are not particularly sensitive to the shape of the energy transfer distribution function and that average energy transfer values suffice to describe such processes. However, they suggest that a more detailed knowledge of the energy transfer distribution may be required in modeling reactions that occur above deep potential wells.[66] High-resolution transient IR absorption experiments provide this type of detail. In this chapter, the dynamics of strong collisional energy transfer is studied for a series of highly vibrationally excited alkylated pyridine molecules with CO_2 using high resolution transient IR spectroscopy. This study is designed to test the impact of molecular structure on collisional energy transfer.

Other studies have found that energy transfer and reactivity are influenced by the length of the alkane chain in molecules involved in collisions. In the reaction of alkyl radicals + O_2, Desain *et al.* found that propane oxidation produces more OH than ethane at each temperature between 296 and 700 K.[67,68] Walker and Morley

found that the branching ratio of alkene + HO_2 products from the reaction of alkyl radicals + O_2 at T=753 K decreases from 99% for ethyl reactants to 80% for propyl and 50% for n-pentyl.[69] Tardy and Song used time resolved optoacoustic spectroscopy to study energy transfer from a series of vibrationally excited fluorinated alkanes in collisions with argon. They reported a decrease of 30% in energy transfer rates as the number of modes in the donor is increased by 2.7, from fluorinated propane to octane with E_{vib}=15,000-40,000 cm^{-1}.[70] This observation was attributed to the presence of low frequency vibrational modes that serve as gateways that are in statistical equilibrium with the remaining oscillators. These modes remain well populated through rapid intramolecular vibrational redistribution (IVR). Molecules with longer chain lengths have more vibrational modes and with similar internal energy, the average energy per mode decreases with increasing alkane chain length.

The flexibility of alkane chains has also been recognized as enhancing collisional energy transfer. Time resolved IR fluorescence studies by Toselli and Barker showed that toluene initially excited with 248 nm light has larger average energy transfer values than benzene for a number of atomic and molecular collision partners.[71] Quasiclassical trajectory calculations by Linhananta and Lim showed that methyl rotors act as gateway modes that introduce additional energy flow pathways that enhance collisional relaxation in collisions between vibrationally hot ethane and propane with rare gases.[72,73] To explain this, the vibrational modes with the lowest frequencies known as the alkane rotation were considered. At low energy, the hindered rotor acts like a normal harmonic vibration. At high energies, the hindered

rotor acts like a near free rotor and promotes energy transfer in highly excited molecules. Free rotors induce internal torsion that acts like internal rotation and converts vibrational energy to external rotation in vibrationally hot molecules. It is thought that both phenomena serve as gateways for vibration-to-rotation, torsion (V→R, torsion) energy transfer. They found that collisional relaxation of vibrationally hot propane is more effective than ethane because propane has more torsional degrees of freedom and a higher vibrational state density.

Bernshtein and Oref compared the collisional relaxation of vibrationally excited benzene, toluene, p-xylene and azulene with argon and with cold benzene using classical trajectory calculations.[74,75] In collisions with argon, with the same donor initial vibrational energy (E_{vib}~41,000 cm^{-1}), they found that average energy transfer values for the methylated donors toluene and p-xylene are larger than for benzene. This result supports the idea that methyl rotors serve as a gateway for collisional energy transfer. However, collisions of toluene and p-xylene with cold benzene have smaller average vibrational energy transfer values than collisions of benzene and azulene with cold benzene, implying that the presence of methyl rotors inhibits collisional energy transfer. The fact that azulene has more efficient energy transfer than p-xylene (even though they have the same number of modes) suggests that the low frequency methyl rotors of toluene and p-xylene actually inhibit energy transfer in molecular collisions by pulling energy away from the rest of the molecule.

High resolution transient IR absorption spectroscopy has been used to investigate how methylation affects collisional energy transfer.[23,24] These studies measured the energy partitioning that results from strong collisions for a series of

highly vibrationally excited methylated pyridines (E_{vib}=38,300 cm^{-1}) with CO_2. These studies provide information about the high energy tail of the energy transfer distribution function (ΔE>3000 cm^{-1}). Results show that the rotational and translational energy of the scattered CO_2 (00^00) molecules is reduced as the number of methyl groups in the vibrationally hot donor molecule is increased. The probability of strong collisions with ΔE>4000 cm^{-1} is reduced by ~50% for 2-methyl-pyridine relative to pyridine. The probability of collisions with ΔE values between 3000 and 4000 cm^{-1}, however, is increased by a factor of 17% for 2-methyl-pyridine relative to those for pyridine.[23] An interesting linear correlation between the curvature of the exponential decay in energy transfer probability and the vibrational state density was observed for seven different aromatic donors.[24,76] This group of energy donors ranges from pyrazine with 24 vibrational modes to azulene with 48 modes.

In this chapter, experiments are described that investigate how alkyl chain length impacts collisional energy transfer. The nascent energy partitioning of scattered CO_2 (00^00) molecules following strong collisions with highly vibrationally excited 2-ethyl-pyridine (E_{vib}=38,570 cm^{-1}) and 2-propyl-pyridine (E_{vib}=38,870 cm^{-1}) was measured. Results show that the probability for strong collisional energy transfer is reduced for 2-ethyl-pyridine relative to 2-methyl-pyridine. However, the propylated donor has a higher probability of strong collisions than 2-ethyl-pyridine. This chapter also explores the relationship of the curvature of the energy transfer distribution function and the vibrational state density for both alkylated and non-alkylated donors. Deactivations for the ethyl and propyl species from the linear

correlation with state density are discussed. Results are discussed in terms of the competing roles of internal energy content, vibrational mode frequencies and larger amplitude motion coming from the increased flexibility of longer alkyl chains. This project has been published in the Journal of Physical Chemistry A.[77]

3.2 Experimental Methods

State-resolved energy transfer measurements were performed using the high resolution transient IR diode laser absorption spectrometer that was described in Chapter 2. To summarize, a 1:1 mixture of donor and CO_2 gases was introduced into a 3 meter flowing gas collision cell with total pressure 20 mTorr at room temperature. 2-ethyl-pyridine (C_7H_9N, ACROS 98+% purity) and 2-propyl-pyridine ($C_8H_{11}N$, Alfa Aesar 98% purity) were purified by several freeze-pump-thaw cycles prior to use. CO_2 (Matheson, 99.995% purity) was used without purification. Highly vibrationally excited donor molecules with E_{vib}~38,800 cm^{-1} were prepared by 266 nm photo excitation from the fourth harmonic output of a pulsed Nd:YAG laser τ_{pulse}=5 ns, followed by rapid radiationless decay to highly vibrationally excited levels of the ground electronic state[61,78]. The pulsed 266 nm UV light interacted with molecules in the gas cell at a repetition of rate of 1Hz and the power was kept below 1 MW/cm^2 to minimize multiphoton absorption. Under these conditions, less than 15% of the donor molecules were excited. Nascent translational and rotational energy gain profiles of individual CO_2 ro-vibrational states were monitored by a single mode tunable diode laser operating near λ=4.3 μm with a spectral resolution of $\Delta\nu_{IR}$=0.0003 cm^{-1}. Time dependent fractional IR absorption was used to monitor the population growth of individual CO_2 high-J states after UV photon excitation. The

high-J states of CO_2 (J>60) have negligible population at room temperature and transient absorption signals correspond to the appearance of the scattered CO_2 molecules. The diode laser output frequency was locked to the center of the transition using a CO_2 reference cell and active feedback control. The nascent translational energy distributions were determined by scanning the laser across a CO_2 rotational line and measuring the Doppler-broadened line profiles for the scattered CO_2 (00^00) molecules. The nascent populations were measured at 1 μs after the UV pulse excitation, well before the average collision time of τ_{col}~4 μs.

3.3 Results and Discussion

The strong collisions of CO_2 with highly vibrationally excited 2-ethyl-pyridine (2EP, E_{vib}=38,570cm^{-1}) and 2-propyl-pyridine (2PP, E_{vib}=38,870cm^{-1}) were characterized by measuring the nascent rotational and translational energy gain of scattered CO_2 (00^00) molecules in high rotational states with J=62-78. Combining the nascent rotational and translational energy distributions with the absolute energy transfer rate gives the energy transfer distribution functions for strong collisions with ΔE>3000 cm^{-1}.[79] This section reports the translational and rotational energy partitioning for scattered CO_2 (00^00), the state-specific bimolecular energy transfer rates and the energy transfer probability distribution functions for ΔE>3000 cm^{-1}. These results are compared throughout with those from earlier studies on collisions of pyridine (Pyr) and 2-methyl-pyridine (2MP) with CO_2.[23]

3.3.1 Transient Absorption of CO_2 (00^00)

Collisions between highly vibrationally excited 2EP (E_{vib}=38,570cm^{-1}) and 2PP (E_{vib}=38,870cm^{-1}) with CO_2 molecules (298 K) lead to energy changes in both collision partners (Eq. 3.1)

$$\text{Donor } (E_{vib}) + CO_2\ (298K) \xrightarrow{k_2^J} \text{Donor } (E_{vib}-\Delta E) + CO_2\ (00^00, J, V) \qquad \text{(Eq. 3.1)}$$

High-resolution IR probing was used to monitor the quantum-state-resolved population changes in CO_2 (J>60) resulting from Eq. 3.1. The probe transitions involve excitation of the ν_3 antisymmetric stretching mode of CO_2 at λ~4.3 μm.

$$CO_2\ (00^00, J, V) + h\nu\ (\lambda\sim 4.3\ \mu m) \rightarrow CO_2\ (00^01, J-1, V) \qquad \text{(Eq. 3.2)}$$

In Eq. 3.2, (00^01) represents one quantum in the CO_2 antisymmetric stretch, J is the angular momentum quantum number, and V is the component of the velocity vector parallel to the IR propagation axis. States with J=62 to 78 were probed using P-branch transitions of the ν_3 band.

Transient absorption signals for appearance of the CO_2 (00^00, J=62) state are shown in Figure 3.1 following collisions with highly vibrationally excited 2EP and 2PP. The signals are linear for the first few μs where single collision conditions predominate. The fractional absorption is converted to the number density of scattered CO_2 molecules using IR transition line strengths.[80,81]

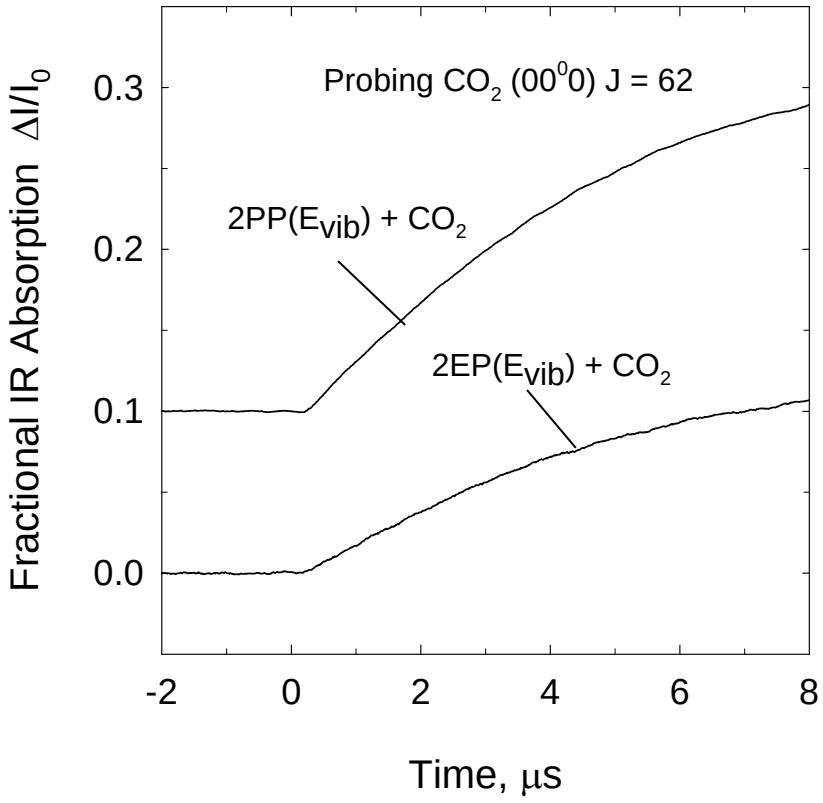

Figure 3.1. Transient IR absorption signals for appearance of $CO_2(00^00)$ J=62 from collisions of CO_2 at 298 K with highly vibrationally excited 2EP (E_{vib}=38,570 cm^{-1}) and 2PP (E_{vib}=38,870 cm^{-1}) (offset for clarity). Nascent CO_2 populations are determined from the IR signal at t=1 μs. The average time between collisions is τ_{col}~4 μs.

3.3.2 Translational Energy Gain of CO_2 (00^00)

The translational energy distributions resulting from strong collisions between highly vibrationally excited 2EP and 2PP with CO_2 were determined by measuring Doppler-broadened lineprofiles for multiple high-J states of CO_2 collected at t=1 μs following optical excitation of the donor molecules. Transient lineshapes for the CO_2 J=74 state following collisions with 2EP and 2PP are shown in Figure 3.2. In Figure 3.2, the fractional IR absorption signals (symbols) are fit to a Gaussian function (solid line). The line profiles are broadened relative to the initial line widths at 298 K (dashed line). The two parameter Gaussian fitting function $G(\Delta\nu) = A\times\exp(-(\nu_0/\Delta\nu)^2/2)$ contains the full width of half max (FWHM) parameter $\Delta\nu$, and line intensity parameter A. The FWHM linewidth of a Gaussian profile is related to the translational temperature of the scattered CO_2 molecules by Eq. 3.3.

$$T_{trans}(lab) = \frac{mc^2}{8R\ln 2}\left(\frac{\Delta\nu}{\nu_0}\right)^2 \qquad \text{(Eq. 3.3)}$$

Here $T_{trans}(lab)$ is the lab frame translational temperature, m is the mass of CO_2, c is the speed of light, R is the gas constant and ν_0 is the transition frequency. The linewidths for individual CO_2 (00^00) states are reported in Table 3.1 along with $T_{trans}(lab)$ and T_{rel}, where T_{rel} is the translational temperatures in the center of mass frame. Values for T_{rel} are determined using Eq. 3.4 based on an isotropic velocity distribution.

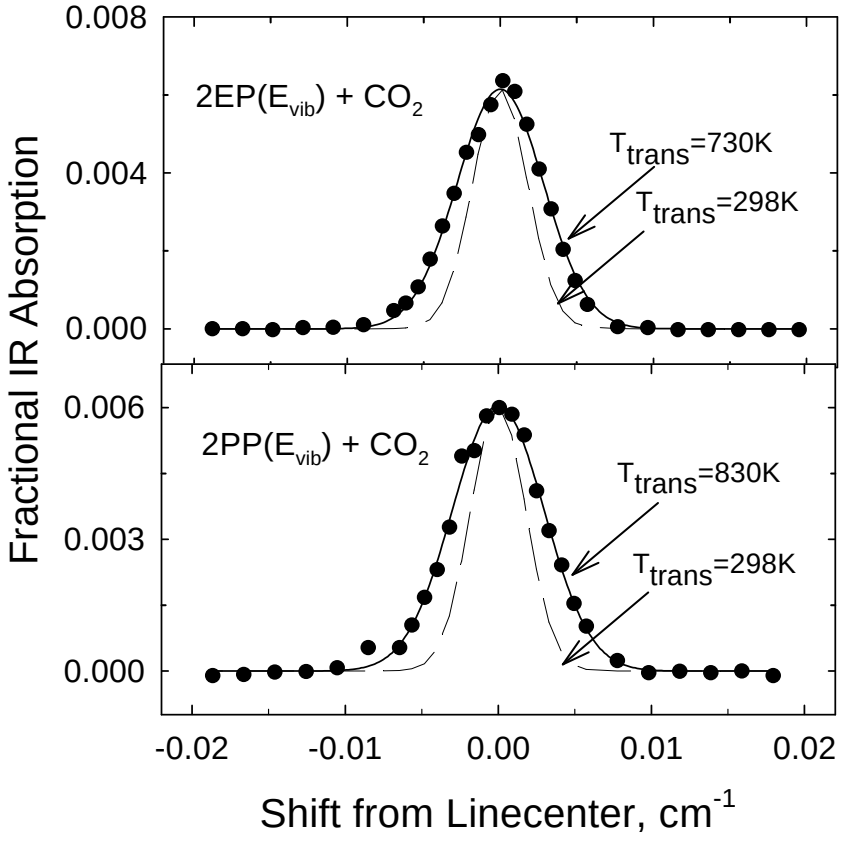

Figure 3.2. Nascent Doppler-broadened line profiles for $CO_2(00^00)$ J=74 following collisions with vibrationally excited 2EP and 2PP. Black circles are IR absorption at t=1 μs. Each line profile is fit to a Gaussian function shown as a solid line. The translational temperature T_{trans}(lab) for the scattered CO_2 molecules is determined from the full width at half maximum linewidth. Transient line widths are all broadened relative to the initial 298 K profiles, shown as dashed lines. Collisions with 2PP consistently have broader line widths than 2EP indicating that the propylated donor has more vibration-to-translation energy transfer than 2EP.

Table 3.1. Doppler-broadened linewidth for scattered CO_2 (00^00) for strong collisions with vibrationally excited 2-ethyl-pyridine (2EP) and 2-propyl-pyridine (2PP)

	CO_2 (00^00)				
	J	E_{rot}, cm^{-1}	$\Delta\nu_{obs}$, cm^{-1} [a]	T_{trans}(lab)[b],K	T_{rel}[c], K
	62	1522.1611	0.0058[e]	560±168	669±201
	66	1722.9413	0.0062	640±192	781±234
2EP	68	1827.9724	0.0063	650±195	796±239
38,570 cm^{-1}	70	1936.0953	0.0067	730±219	908±273
	72	2047.3081	0.0066	720±216	894±268
	74	2162.6090	0.0066	730±219	908±273
	78	2399.4677	0.0066	730±219	908±273
	62	1522.1611	0.0063	645±194	772±232
	66	1722.9413	0.0068	760±228	928±279
2PP	68	1827.9724	0.0071	833±250	1028±308
38,870 cm^{-1}	70	1936.0953	0.0071	830±249	1024±307
	72	2047.3081	0.0071	830±249	1024±307
	74	2162.6090	0.0071	843±253	1042±313
	76	2278.9962	0.0074	910±273	1133±340

[a] The full width half maximum linewidth from fitting the t=1 μs transient line profile to a Gaussian function. The uncertainty in linewidths is ±0.001 cm^{-1}.

b) The lab frame translational temperature is found using $T_{trans}(lab) = \left(\frac{mc^2}{8k_B \ln 2}\right)\left(\frac{\Delta\nu_{obs}}{\nu_0}\right)^2$ where m is the mass of CO_2, c is the speed of light, k_B is Boltzmann's constant, ν_0 is the IR transition frequency and $\Delta\nu_{obs}$ is the nascent Doppler-broadened line width.

c) The center of mass translational temperature for an isotropic distribution of scattered molecules is found using $T_{rel} = (T_{trans}(lab) - T_0) \times \left(m_{CO_2}/m_{donor}\right)$ where T_0=298 K is the pre-collision temperature.

$$T_{rel} = (T_{trans}(lab) - T_0) \times \left(\frac{m_{CO_2}}{m_{donor}} \right) \quad \text{(Eq. 3.4)}$$

Here T_0=298 K is the pre-collision temperature and m_{CO2} and m_{donor} are the masses of CO_2 and the donor molecules, respectively. T_{rel} is a measure of the translational energy of the scattered molecules following collisional energy transfer.

A comparison of the center of mass translational energy for collisions of CO_2 with four different pyridine donors Pyr, 2MP, 2EP and 2PP is shown in Figure 3.3. Each donor has been excited initially with λ=266 nm. There is a notable effect of donor alkylation on the collisional energy transfer. Relaxation of pyridine imparts more translational energy than the alkylated donors. For the alkylated donors, 2MP, 2EP and 2PP, the product translational energy values are similar. However, when data for the three alkylated donors are compared in the lower plot of Figure 3.3, it is seen that 2MP consistently imparts more product translational energy than 2EP or 2PP. This observation is explained as follows. The number of vibrational modes increases from 36 modes for 2MP to 45 modes for 2EP and 54 modes for 2PP. The three donor molecules have similar amounts of internal energy, but that internal energy is spread among more degrees of freedom in larger molecules. The observation that less vibrational energy is imparted through collisions with 2EP and 2PP than with 2MP is consistent with that fact that on average the larger donor molecules have less energy per mode. The addition of alkyl groups in particular

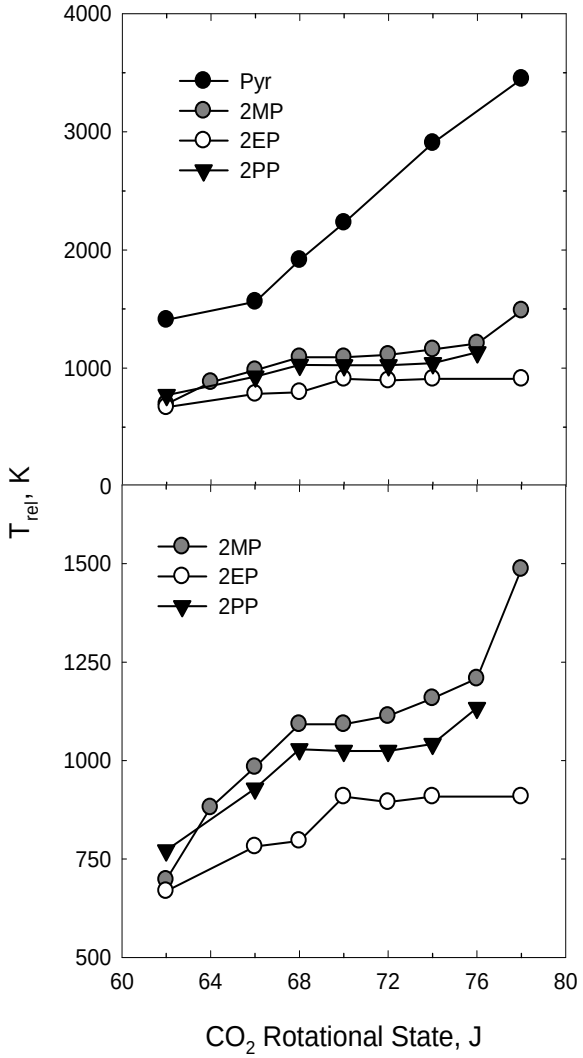

Figure 3.3. Relative translational temperatures, T_{rel}, between donors and CO_2 (00^00) J=62-78. The lower graph shows data for 2EP and 2PP along with earlier results for 2-methyl-pyridine (2MP). The increase in T_{rel} with CO_2 J state is consistent with an impulsive energy transfer mechanism. For a given J state, T_{rel} generally follows the ordering of 2MP>2PP>2EP. The top graph compares T_{rel} of the alkylated donors with those for pyridine (Pyr) and shows that alkylation substantially reduces the translational energy of the scattered molecules.

introduces low frequency torsions and hindered or nearly free rotors that are preferentially populated by IVR. This is the case for methyl pyridine.

However, Figure 3.3 also shows that strong collisions with 2PP lead to more translational energy than those of 2EP for all CO_2 (00^00) states that were probed, even though highly vibrationally excited 2PP has less energy per mode on average than 2EP. This observation indicates that dynamical effects are at work, namely that longer alkyl chains increase the amount of translational energy in scattered molecules due to strong collisions. We note that this is not a substantial effect on the translational energy and that the translational energy distributions from 2EP and 2PP are within experimental error as listed in Table 3.1. However, as shown in Figure 3.3, 2PP consistently exhibits larger energy releases than 2EP and the relative uncertainty is less than the absolute uncertainty.

3.3.3 Rotational Energy Gain of CO_2 (00^00)

Nascent rotational energy distributions were obtained by measuring populations of CO_2(00^00) with J=62-78 that scatter from highly vibrationally excited 2EP and 2PP. Figure 3.4 shows semi-log plots of the degeneracy-weighted populations of scattered CO_2 molecules measured at t=1 μs as a function of CO_2 rotational energy for both donors. The scattered CO_2 populations are each well described by a Boltzmann distribution with a rotational temperature T_{rot}, given by Eq. 3.5.

$$\frac{N_J}{g_J} = \exp\left(-\frac{E_J}{k_B T_{rot}}\right) \qquad \text{(Eq. 3.5)}$$

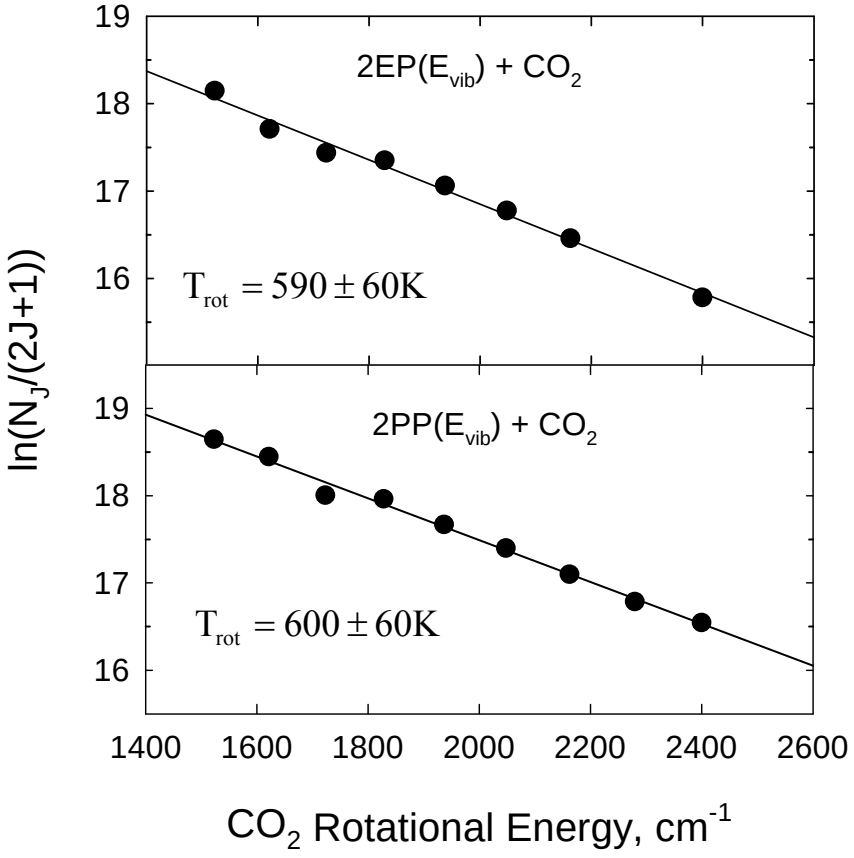

Figure 3.4. Nascent t=1 μs rotational distributions of scattered CO_2 (00^00) with J=62-78 following collisions with vibrationally hot 2EP and 2PP. The distribution for 2MP is similar with T_{rot}=610 K. Increasing the alkyl chain on the pyridine donor from methyl through propyl has little effect on the rotational energy of the scattered CO_2.

Here N_J is the CO_2 population in the J quantum state, the rotational degeneracy is $g_J=2J+1$, E_J is the rotational state energy, and k_B is the Boltzmann constant. A relative population measurement was used to reduce error from long time fluctuations in the experiment.

The nascent rotational distributions from collisions with the two donors are nearly the same: T_{rot}=590±60 K for 2EP collisions and T_{rot}=600±60 K for 2PP. These values are nearly identical to that for quenching of 2MP where T_{rot}=616±60 K for the scattered CO_2. For this piece of the energy transfer distribution, the average change in CO_2 rotational energy for the alkylated donors is $\langle \Delta E_{rot} \rangle = \frac{3}{2} k_B (T_{rot} - T_0)$=315 cm^{-1}, in which T_0=298 K. In contrast, when pyridine (E_{vib}=37,920 cm^{-1}) is the donor molecule, the scattered high-J CO_2 molecules have a rotational temperature of T_{rot}=835 K and an average change in rotational energy of $\langle \Delta E_{rot} \rangle$=560±90 cm^{-1}. Thus we find that donor alkylation reduces the amount of energy that goes into CO_2 rotation and that this effect is similar for methyl, ethyl and propyl substituents.

3.3.4 Energy Transfer Rate Constants for Donor/CO_2

State-resolved energy transfer rate constants k_2^J for strong collisions of CO_2 with highly vibrationally excited 2EP and 2PP were determined by measuring the early time appearance of rotational states of CO_2, as shown in Eq. 3.1. CO_2 populations were measured at t=1 μs after donor excitation where the donor and CO_2 bath concentrations are essentially the same as their respective values at t=0. Under these early time conditions, rate constants were determined for known initial donor and CO_2 bath concentrations using Eq. 3.6.

$$k_2^J = \frac{\Delta[CO_2(00^00,J)]}{[Donor^E]_0[CO_2]_0\Delta t} \quad \text{(Eq. 3.6)}$$

Here $[CO_2(00^00,J)]$ is the CO_2 population at a rotationally excited J state after a time interval Δt. $[Donor^E]_0$ is the initial concentration of highly vibrationally excited 2EP or 2PP determined from the observed UV absorption. $[CO_2]_0$ is the bulk CO_2 concentration at 298 K. The scattered CO_2 populations include contributions from the Doppler-broadened line widths. The rate constants for the strong collisions that quench 2EP and 2PP are listed in Table 3.2.

The comparison of energy transfer rate constants for strong collisions of pyridine, 2MP, 2EP and 2PP with CO_2 is shown in Figure 3.5. Overall, the ordering of rates goes as 2PP>2MP>2EP>Pyr. To account for differences in the collision rates for the different donors, it is convenient to compare the energy transfer on a per-collision basis by normalizing the energy transfer rate to the collision rate. The collision rate depends on the collisional cross section, reduced mass and translational temperature. The Lennard-Jones collision rates for the donor:CO_2 pairs are $k_{LJ}=5.58\times10^{-10}$ cm^3 $molecule^{-1}$ s^{-1} for pyridine:CO_2, $k_{LJ}=5.86\times10^{-10}$ for 2MP:CO_2, $k_{LJ}=6.39\times10^{-10}$ for 2EP:CO_2 and $k_{LJ}=6.76\times10^{-10}$ for 2PP:CO_2. Details of the collision rate calculation are given in Appendix B. For these donors, the cross section has the largest effect on the collision rate. The collisional cross section for 2PP-CO_2 is 30% larger than for Pyr-CO_2 and the collision rate for 2PP-CO_2 is 21% larger than

Table 3.2. Rate constants for energy gain in CO_2 (00^00, J) following collisions with highly vibrationally excited 2-ethyl-pyridine (2EP) and 2-propyl-pyridine (2PP)

CO_2 (00^00)		k_2^J, 10^{-13} cm^3 molecule^{-1} s^{-1}	
J state	E_{rot}, cm^{-1}	2EP, E_{vib}=38,570 cm^{-1}	2PP, E_{vib}=38,870 cm^{-1}
62	1522.1611	15.7±4.7	20.0±6.0
64	1621.0037	11.3±4.4	17.0±5.1
66	1722.9413	8.7±2.6	11.1±3.3
68	1827.9724	7.6±2.3	11.1±3.3
70	1936.0953	6.2±1.9	8.5±2.6
72	2047.3081	4.5±1.4	6.7±2.0
74	2162.6090	3.5±1.1	5.1±1.5
76	2278.9962	2.6±0.8	3.8±2.3
78	2399.4677	2.0±0.6	3.1±0.9
k_2^{int}, 10^{-12} cm^3 molecule^{-1} s^{-1} for CO_2 J>60		6.2±1.9	8.6±2.6
k_{LJ}, 10^{-10} cm^3 molecule^{-1} s^{-1} [a)]		6.39	6.76

[a)]The collision rate constants were determined using a Lennard-Jones (LJ) potential as the intermolecular potential during the donor/CO_2 collisions. The method of getting the collision rate constants is described in Appendix B.

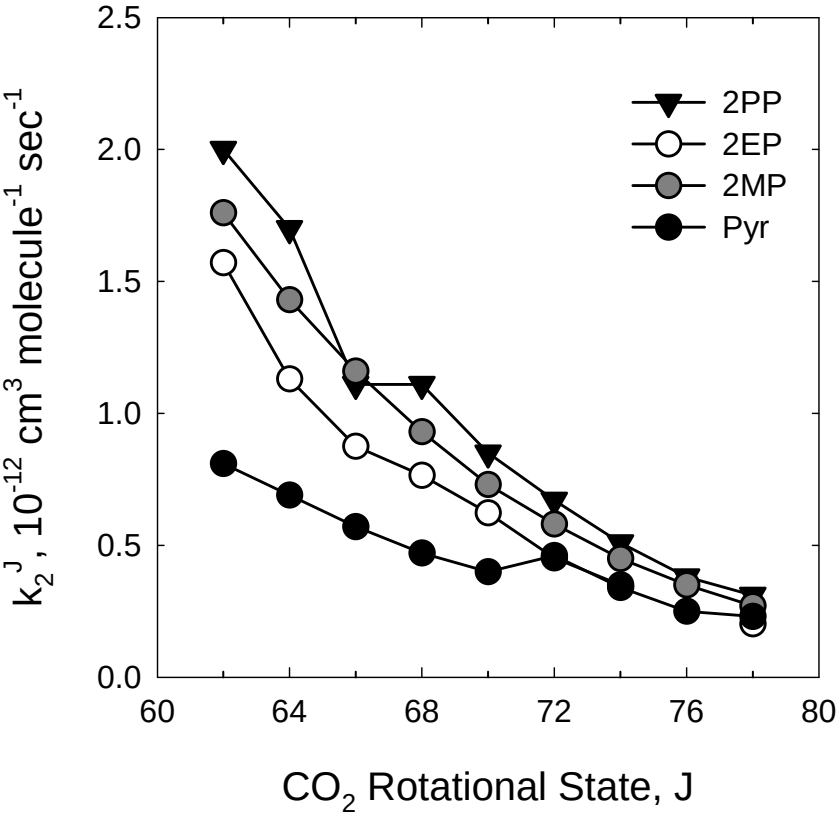

Figure 3.5. Absolute rate constants k_2^J for appearance of scattered CO_2 (00^00) J=62-78 following collisions with vibrationally excited donors. The ordering of energy transfer rates for appearance of a given CO_2 J state is 2PP>2MP>2EP. The rates for energy transfer from the alkylated donors are larger than those from pyridine (Pyr).

for Pyr-CO_2. The reduced mass has a smaller effect. The reduced mass of 2PP-CO_2 is 14% larger than that for Pyr-CO_2, making the collision velocity for 2PP-CO_2 only ~6% smaller than that for Pyr-CO_2. Energy transfer probabilities P_J were determined by $P_J = k_2^J/k_{LJ}$. The ordering of energy transfer probabilities for individual J states of CO_2 is similar to the ordering of rate constant in Figure 3.5. The J-specific probabilities for 2PP relaxation are about twice those of pyridine.

3.3.5 P(ΔE) Curves for Strong Collisions with CO_2

Energy transfer probability distribution functions P(ΔE) describe the probability of energy transfer ΔE from a highly excited molecule due to collisions. The state-resolved energy transfer data here were used to determine P(ΔE) curves for the collisions systems under investigation. The magnitude of the exchanged energy ΔE is determined from the measured rotational and translational energy gain profiles and the observed energy transfer rates. The methodology of this transformation has been described by Michaels and Flynn.[82] The key idea is to convert from state- and velocity-indexed data to a ΔE-indexed probability. For each scattered J state, CO_2 has a speed distribution whose spread is specified by the spectral Doppler-broadening. The probability for energy transfer to each state is determined by the ratio of the energy transfer rate constant to the collision rate. The change in energy ΔE is defined as the difference between final energy (including the translational and rotational component) and the average initial rotational and translational energies. The overall energy transfer probability distribution function P(ΔE) is obtained by summing over the distribution functions of individual J states of the scattered CO_2 molecules.

A complete picture of the energy transfer probability distribution functions requires information on both low- and high-J states of the scattered bath molecules. However, scattered CO_2 molecules in low-J states have not been characterized in these studies so the P(ΔE) curves presented here are complete only for ΔE>3000 cm^{-1}. In addition, the contributions to ΔE from changes in donor rotation are not accounted for our measurements. Simulations have shown that donor molecules can gain rotational energy through quenching collisions.[83] The extent of rotational energy gain in the donors is expected to be less than for CO_2 based on the conservation of angular momentum and the relatively small rotational constants for the donor molecules.

Figure 3.6 shows the energy transfer distribution functions for the strong collisions of 2EP and 2PP with CO_2. The P(ΔE) curves for Pyr and 2MP are also included in Figure 3.6 for comparison. The data show that pyridine has the largest probability for strong collisions with ΔE> 4000 cm^{-1}. For the alkylated donors, 2MP and 2PP have similar P(ΔE) curves while 2EP has the lowest probability for strong collisions. The four donor molecules have similar internal energy of E_{vib}~37,900-38,800 cm^{-1}. However, pyridine has the fewest vibrational modes and thus more energy per mode on average. This situation leads to a relatively large fraction of strong collisions. The alkylated pyridines have less energy per mode on average than non-alkylated pyridines and in general the likelihood of strong collisions for these donors is reduced. The probability of relaxation via strong collisions with ΔE>4000 cm^{-1} has the order Pyr>2MP>2EP. However, this trend does not continue for 2PP.

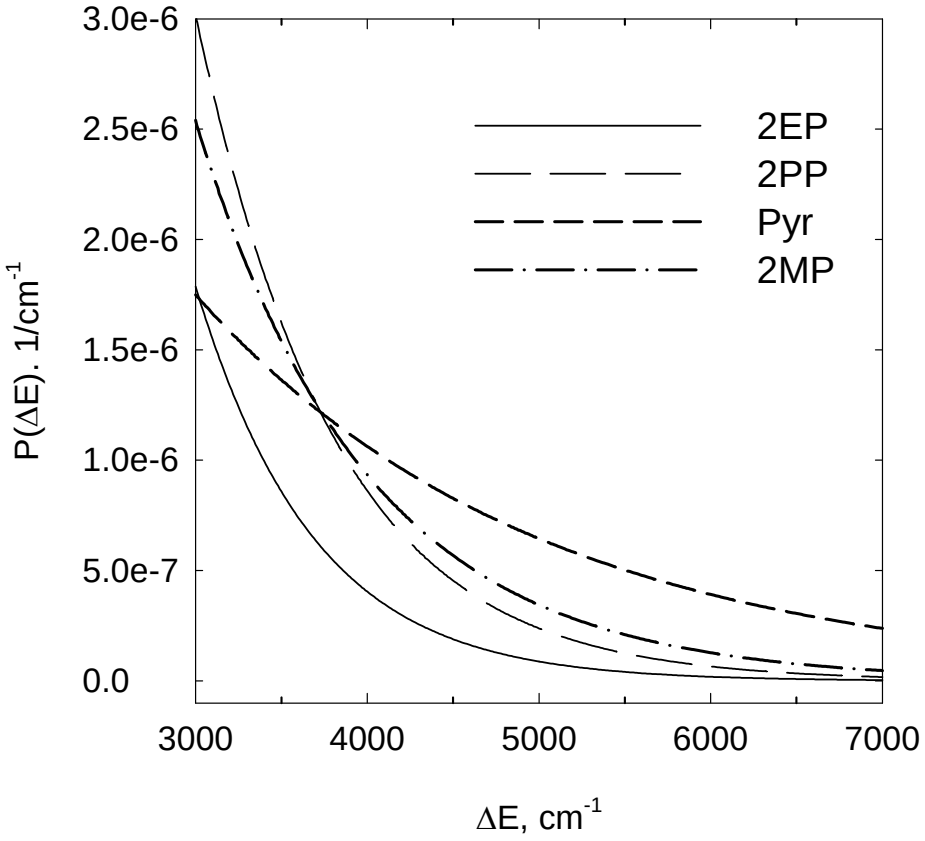

Figure 3.6. Energy transfer probability distribution functions for energy gain into $CO_2(00^00)$ J=62–78 following collisions with highly vibrationally excited donor molecules. Comparison of P(ΔE) curves for strong collisions with ΔE>3000 cm^{-1} of CO_2 with vibrationally hot 2EP and 2PP. 2PP has a larger probability for strong collisions than 2EP.

For the alkylated donors, the probability of strong collisions is ordered as 2MP~2PP>2EP.

One interesting result is that 2PP imparts substantially more energy to the translational degrees of freedom of CO_2 in single collision events with $\Delta E > 3000$ cm^{-1} than 2EP does. This result is not consistent with the lower average energy per mode of 2PP. The source of this effect may be dynamical in nature. One possible reason may be that differences in the potentials for the torsional and methyl rotor vibrations of the various donors contribute to the observed differences in their $P(\Delta E)$ curves. Linhananta and Lim performed simulations on ethane and propane and found that methyl and ethyl torsional motion can enhance vibrational relaxation.[72,73] It is also possible that the longer alkyl chain in 2PP introduces new dynamical processes that are not present in aromatic and methylated aromatic species. Longer chain alkyl groups can undergo larger amplitude motion and whip-like motions of the propyl chain may account for the enhanced strong collisions in 2PP. Another possible reason is that the longer chain length of 2PP introduces new possibilities for constrained configurations that increase the mode frequencies of the propyl group. Models based on simple geometric considerations indicate that the propyl group in 2PP is long enough to form a secondary ring-like structure adjacent to the pyridine ring. Constraining the propyl group configuration actually increases the energy content of the aromatic ring, which in turn is likely to enhance the strong collisions. This is in agreement with the simulation results of Bernshtein and Oref showing that collisional energy transfer from azulene (E_{vib}) to benzene is enhanced relative to that for p-xylene (E_{vib}).[74] Even though the two donors have the same number of modes,

the stiffer ring system has higher frequency modes a higher probability of vibrational energy transfer. It is not clear why the simulations do not show a similar effect when argon is the quencher. Simulations on collisional quenching of alkyl chains attached to aromatic molecules should provide additional insight into this effect.

3.3.6 State Density and Strong Collisions for 2PP and 2EP

Earlier studies from the Mullin group have shown that the extent of strong collisional energy transfer of highly excited azabenzenes and methylated azabenzenes correlates with the energy dependence of the vibrational state density. This correlation is seen for collisions with CO_2 and with H_2O.[21,23,24,76] This observation is consistent with a description of the collisional quenching of highly vibrationally excited molecules based on Fermi's Golden Rule known as GRETCHEN (Golden Rule Excitation Transfer in Collisions of High Energy Molecules).[21-24,76]

Fermi's golden rule describes the transition rate (probability of transition per unit time) from one energy eigenstate $|i\rangle$ of a quantum system (initial state) into a continuum of energy eigenstates $|f\rangle$ (final state) due to a perturbation $\hat{H}$ in Eq. 3.7.

$$\text{Rate} = \frac{dP}{dt} = \frac{4\pi^2}{h}\left|H_{if}\right|^2 \rho\left(E_f\right) \qquad \text{(Eq. 3.7)}$$

Here the ρ is the state density of the final states, H_{if} is the matrix element that couples initial and final states and h is the Planck's constant. The GRETCHEN model treats collisions as perturbations that induce ΔE transitions in the hot donor molecules from

E to E-ΔE. The probability of energy transfer via impulsive collisions is proportional to the rate of energy transfer and given by Eq. 3.8.

$$P(\Delta E) \propto \frac{4\pi^2}{h}\left|H_{if}\right|^2 \rho(E - \Delta E) \qquad \text{(Eq. 3.8)}$$

CO_2 molecules are activated during collisional energy transfer, but the contribution to the density of states from the CO_2 is negligible relative to that of the hot donor. The state density of the final states ρ is essentially the state density of donor molecules at E-ΔE. The collisions are impulsive which means only the momenta change during the collisions. Eq. 3.8 assumes that the perturbation is short in time and the matrix element H_{if} can be considered as a constant.

Eq. 3.8 predicts that the energy transfer probability distribution is proportional to energy dependence of the donor state density. Here, the relationship between state density ρ(E-ΔE) and energy transfer probability P(ΔE) for the alkyated pyridines is explored. The P(ΔE) curves such as those shown in Figure 3.6 characterize the probability that a vibrationally hot molecule will lose an amount of energy ΔE through collisions with CO_2. The curve for each donor is fit to a single exponential decay using Eq. 3.9,

$$P(\Delta E) = \alpha_{obs} \exp(-\beta_{obs} \Delta E) \qquad \text{(Eq. 3.9)}$$

where α_{obs} and β_{obs} are fitting parameters. β_{obs} describes the relative collision 'strength' for a given donor, as shown in Figure 3.7. $\beta_{obs}=15.3\times10^{-4}$ /cm^{-1} for 2EP and $\beta_{obs}=12.9\times10^{-4}$ /cm^{-1} for 2PP.

The vibrational state density of the vibrationally excited donors also changes as a function of ΔE as shown in Figure 3.8. The state densities were calculated by a direct sum of vibrational states as described later in this section. The state densities of 2EP and 2PP are well described by Eq. 3.8 for $\Delta E=0$ to 10,000 cm^{-1}.

$$\rho(E-\Delta E) = \alpha_\rho \exp(-\beta_\rho \Delta E) \qquad \text{(Eq. 3.10)}$$

The parameter β_ρ characterizes how the vibrational state density changes with internal energy. The state densities for 2EP and 2PP are $\beta_\rho=8.07\times10^{-4}$/cm^{-1} for 2EP and $\beta_\rho=9.13\times10^{-4}$/cm^{-1} for 2PP. Both P(ΔE) and $\rho(E-\Delta E)$ are exponential functions of ΔE over the range of interest, for $\Delta E=0$ up to 10,000cm^{-1}.

Figure 3.9 shows the correlation between β_{obs} from experimental distribution functions and β_ρ from calculated state densities for the molecules studied here along with values from a number of other donor molecules reported elsewhere: pyrazine,[23] pyridine,[23] methyl-pyridine isomers (2MP, 3MP and 4MP),[23,24] 2,6-dimethyl-pyridine (2,6MP)[23] and azulene[76]. The β_{obs} and β_ρ values are also listed in Table 3.3.

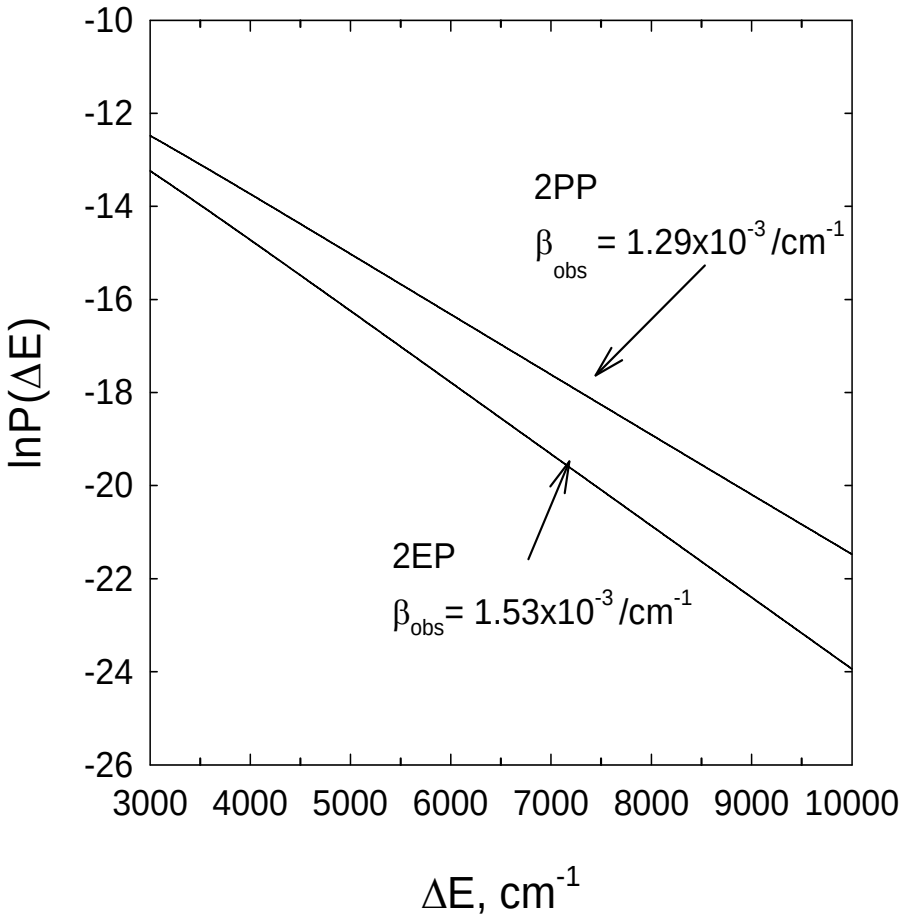

Figure 3.7. Semi-log plot of P(ΔE) with ΔE>3000 cm^{-1} for strong collisions of vibrationally hot 2EP and 2PP with CO_2. The slope equals $-\beta_{obs}$.

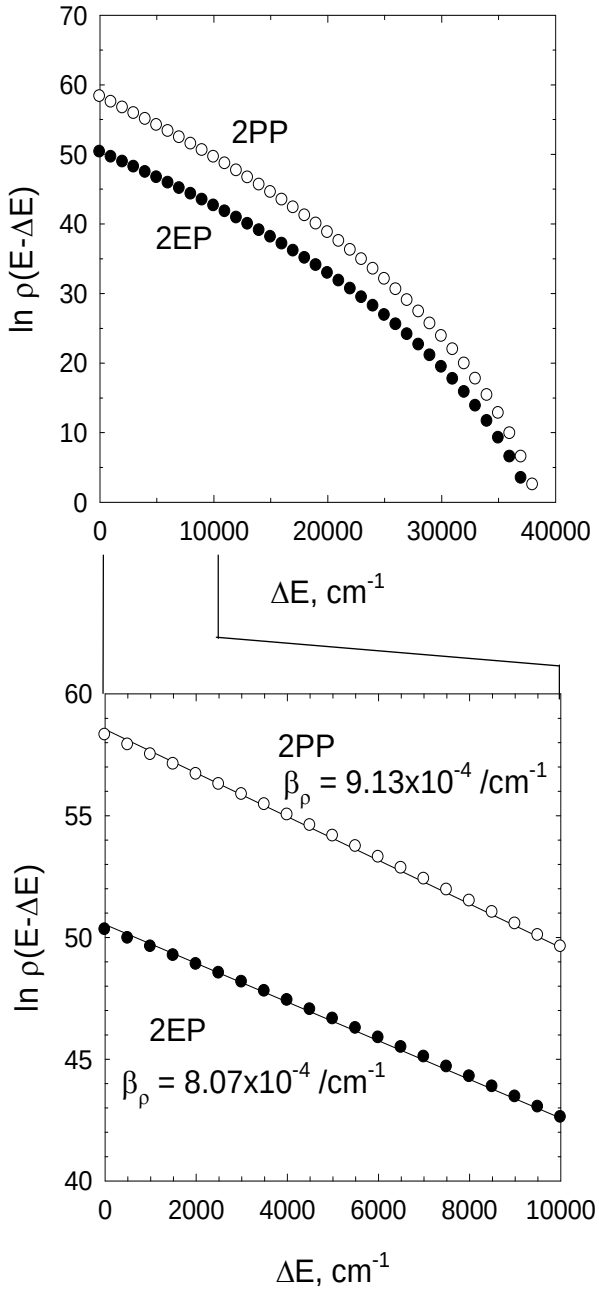

Figure 3.8. Semi-log plots of the donor vibrational state density as a function of internal energy, ΔE. The state density for each donor was fit to an exponential decay in energy with a fitting parameter β_ρ.

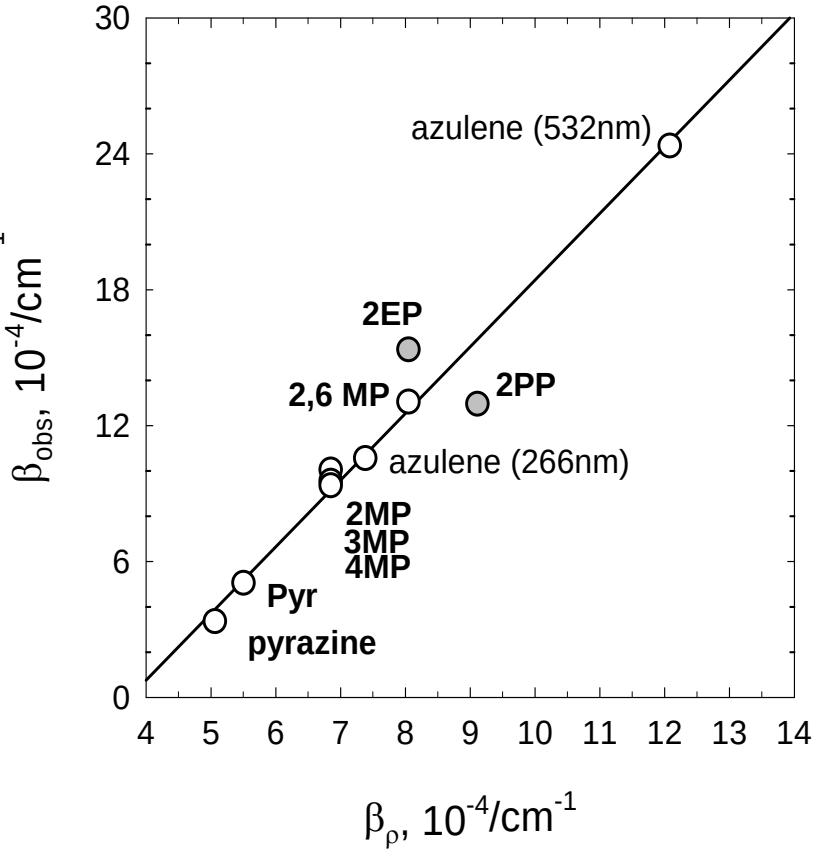

Figure 3.9. Comparison of β_{obs} for strong collisions and the vibrational state density energy dependence parameter β_{ρ} for collisions of CO_2 with highly vibrationally excited donors: pyrazine, pyridine (Pyr), methyl-pyridine isomers (2MP, 3MP, 4MP), 2,6-dimethyl-pyridine (2,6MP), azulene, 2EP and 2PP. A linear correlation is seen for the unsubstituted donors and for donors containing methyl or ethyl groups. For donor with larger alkyl groups, β_{obs} no longer correlates with changes in state density associated with ΔE. In the limiting case of no rotational or translational energy gain in CO_2, β_{obs} has a value near 4×10^{-3}/cm^{-1}.

Table 3.3. The energy transfer probability parameter β_{obs} of the P(ΔE) at high energy tail (ΔE=3000-10,000 cm^{-1}) and highly vibrationally excited donor molecules state density parameter β_ρ for different donor/CO_2 pairs.

Donor molecules	E_{vib}, cm^{-1}	β_{obs}, $10^{-4}/cm^{-1}$	β_ρ, $10^{-4}/cm^{-1}$
pyrazine[a)]	37900	3.3	5.08
pyridine(Pyr)[a)]	37920	5.0	5.52
2-methyl-pyridine (2MP)[a)]	38313	10.0	6.87
3-methyl-pyridine (3MP)[b)]	38313	9.5	6.87
2-methyl-pyridine (4MP)[b)]	38313	9.3	6.87
2,6-dimethyl-pyridine (2,6MP)[a)]	38702	13.0	8.07
azulene (266 nm)[c)]	38580	10.5	7.40
2-ethyl-pyridine (2EP)[d)]	38568	15.3	8.07
2-propyl-pyridine (2PP)[d)]	38867	12.9	9.13
azulene (532 nm)[c)]	20390	24.5	12.1

[a)]Data taken from the work by Park *et al.*[23]

[b)]Data taken from the work by Miller *et al.*[24]

[c)]Data taken from the work by Yuan *et al.*[76]

[d)]Data taken from this work[77]

In general the data in Figure 3.9 show that larger donor molecules have larger values of β_ρ and β_{obs}. This result is in agreement with predictions from the GRETCHEN model. We find that strong collisions that correspond to smaller changes in state density (smaller β_ρ values) generally occur with higher probabilities (relative to the weak collisions for that donor:bath pair). In this way, donors with fewer vibrational modes (and state densities that vary more slowly with ΔE) have a larger percentage of strong collisions than larger donors where the state density changes more rapidly as a function of ΔE.

A very good linear correlation is seen in Figure 3.9 for all donors shown except for the two donors reported here: 2EP and 2PP. Strong collisions of 2EP with $\Delta E > 3000$ cm^{-1} are not as strong as predicted by the state density energy dependence while those for 2PP are stronger than predicted. It is possible that 2EP and 2PP deviate from the linear state density correlation due to the dynamical effects discussed in Section 3.3.5, namely that large amplitude motion of the propyl chain and possible ring closing mechanisms of the ethyl group may contribute to the energy transfer differences. The impact of these processes is not accounted for by statistical models but may be relevant to details of collisional energy transfer. If this is the case, a direct correlation of energy transfer with state density will be valid only when these effects are not present, that is, for quenching collisions of simple aromatic and methylated aromatic donor molecules.

It is also possible that the state density calculations for 2EP and 2PP are affecting the comparison in Figure 3.9. The presence of low-frequency torsional modes can have a dramatic effect on state density calculations. Here we consider the

sensitivity of the β_ρ values on details of the state density calculations for 2EP and 2PP.

The state densities for 2EP and 2PP were determined as a function of E-ΔE using donor vibrational frequencies and performing a direct count of states with the Beyer-Swinehart algorithm.[84] The vibrational modes of 2EP with frequencies above 200 cm^{-1} were measured by Green and Barnard.[85] However, the low frequency modes that correspond to torsional motions of the ethyl group were not reported. The normal modes of 2EP and 2PP were estimated using Hartree-Fock calculations at the 6-311g** level.[86] At this level of theory, the calculated frequencies for normal modes do not exactly reproduce the experimental results. We found however that the state density parameter β_ρ was not particularly sensitive to the exact mode frequencies and that the estimated frequencies yielded reliable β_ρ values. To verify this, β_ρ values were determined for pyridine, 2MP and 2,6MP using calculated frequencies and using experimental frequencies. The resulting β_ρ values were the same within 0.7%. The state density is very sensitive to the choice of the low frequency modes, but the β_ρ value was much less sensitive. For example, the state density of 2EP (E_{vib}=38,570 cm^{-1}) is 10 times larger if one low frequency mode is increased from 20 to 200 cm^{-1}, but β_ρ was insensitive to this change, varying only by less than 0.2%.

We also considered how the alkyl rotors impacted the state density calculations. Vibrational modes that correspond to internal rotations were treated differently depending on whether they are hindered or free rotors. A one-dimensional hindered rotor potential energy U(φ) is given in Eq. 3.11.

$$U(\varphi) = \frac{V}{2}(1 - \cos(n\varphi)) \qquad \text{(Eq. 3.11)}$$

where φ is the rotation angle, n is the number of minima, and V is the barrier height. For a hindered rotor, the mode energy is less than the barrier height, $E_{mode}<V$. A free rotor model is more appropriate at higher energies when $E_{mode}>V$. The hindered rotor model was used by Draeger[87] for the methyl group in toluene at 298 K with a barrier height of V=720 cm^{-1}, zero-point energy E_0=86 cm^{-1} and first excited state E_1=258 cm^{-1}. Highly vibrationally excited 2EP (E_{vib}=38,570 cm^{-1}) on average has $\langle E \rangle$~1300 cm^{-1} in the lowest frequency mode. This energy is far greater than the barrier height of 720 cm^{-1} for a methyl hindered rotor in toluene, and it is reasonable that the methyl rotor in vibrationally excited 2EP is a free rotor. We treated the internal rotors in 2EP and 2PP as harmonic oscillators in one extreme and as free rotors the other extreme to establish limiting values of β_ρ. The state density in the free rotor limit was determined using a modified Beyer-Swinehart method.[88] The choice of the hindered or free rotor model made almost no difference on β_ρ and values for the two limiting cases have differences that are less than 0.1%.

3.4 Conclusion

The effect of alkylation on the strong collisional energy transfer between CO_2 and a series of highly vibrationally excited alkyl-pyridines (E_{vib}~38,400 cm^{-1}) where alkyl = methyl, ethyl and propyl has been investigated. The nascent rotational and translational energy distributions for scattered CO_2 molecules were measured under single collision conditions using high resolution transient IR absorption. The largest

influence on the amounts of rotational and translational energy gain in the scattered molecules is whether the donor is alkylated. Strong collisions between highly vibrationally excited pyridine and CO_2 lead to significantly more rotational and translational energy in the scattered molecules than for the alkylated donors. Differences are also seen in the distribution functions for the strong collisions of the alkylated donors. The ordering of strong collision probabilities with CO_2 is pyridine>2-methyl-pyridine~2-propyl-pyridine>2-ethyl-pyridine. The probability for strong collisions with CO_2 is twice as large for 2-propyl-pyridine as for 2-ethyl-pyridine. This observation cannot be explained solely by a statistical description of the vibrationally hot donor molecule. These results show that longer chain alkyl groups actually can enhance strong collisional energy transfer, possibly due to enhanced flexibility of the donor molecules.

Chapter 4: Energy Transfer Dynamics in the Presence of Preferential Hydrogen Bonding: Collisions of Pyridine-h_5, -d_5 and -f_5 (E_{vib}~38,300 cm^{-1}) with H_2O

4.1 Introduction

Hydrogen bonding interactions are important in a wide array of disciplines ranging from biochemistry[89-91] to atmospheric chemistry.[92-94] Preferential hydrogen bonding of H_2O and its isotopes has been observed in interactions with aromatic molecules. Stable binary complexes of nitrogen-containing aromatics with water have local energy minima for both σ– and π-type hydrogen bonding. The interaction of a hydrogen atom on water and the nitrogen lone pair leads to σ-type hydrogen bonding. In π-type hydrogen bonding, both hydrogen atoms of water interact with the aromatic π cloud. These structures are illustrated in Figure 4.1. This chapter focuses on what effect this type of preferential hydrogen bonding has on collisional energy transfer.

A number of studies have characterized σ– and π-type interactions of water and aromatic molecules. Using microwave spectroscopy in a molecular beam, Caminati and coworkers observed an interesting isotope effect in σ-type complexes of pyrazine ($C_4H_4N_2$) and water. They saw evidence for the $C_4H_4N_2$-HOH and $C_4H_4N_2$-DOH configurations but found no evidence for the $C_4H_4N_2$-HOD conformer.[95] They attributed the selective formation of the $C_4H_4N_2$-DOH complex to

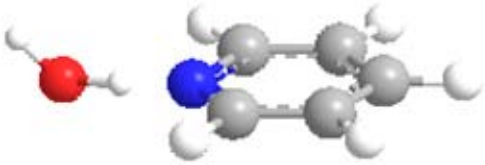

pyridine-h_5

pyridine-d_5

σ-bonding

pyridine-h_5

pyridine-d_5

π-bonding

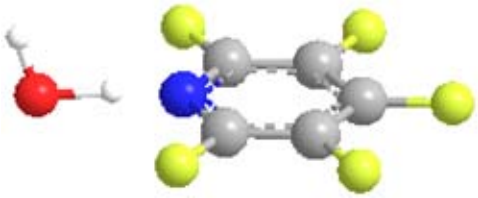

pyridine-f_5

σ-bonding

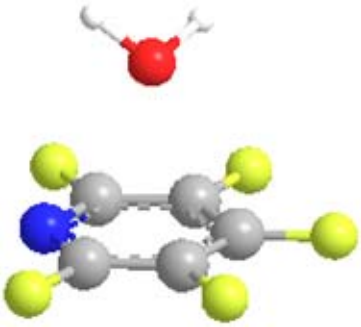

pyridine-f_5

π-bonding

Figure 4.1. Structures of σ- and π-type hydrogen bonding of pyridine-h_5, pyridine-d_5 and pyridine-f_5 with H_2O.

a difference in zero point energy relative to $C_4H_4N_2$-HOD. A related isotope effect has been observed in collisional energy transfer from highly vibrationally excited pyrazine (E=37,920 cm^{-1}) with H_2O and HOD.[96,97] High-resolution transient IR absorption studies show that both H_2O and HOD are scattered with relatively small amounts of translational energy but that H_2O is scattered with twice the rotational energy of HOD. The reduced rotational energy of HOD is attributed to a stronger interaction with the nitrogen lone pair.[96,97]

Hydrogen bonding interactions of H_2O with aromatic π-systems have also been observed and characterized.[98-103] Rotationally-resolved molecular beam experiments by Suzuki *et al.*[103] established that benzene-water clusters have the hydrogen atoms of water positioned toward the π-electron cloud.[103] Matrix isolation studies by Engdahl and Nelander[104] as well as resonance ionization studies by Gotch and Zweir[105] showed that the two hydrogen atoms, when vibrationally averaged, are equivalent. When benzene is fluorinated, however, the large electronegativity of the fluorine atoms distorts the π-electron distribution and leaves the carbon atoms electron deficient. Alkorta, Rozas, and Elguero characterized the electrostatics and interaction energies of a series of small molecules hydrogen bonded to C_6H_6 and to C_6F_6.[99,100] They found that stable complexes form between electron-donating atoms and the π-cloud of C_6F_6 while C_6H_6 attracts electron-deficient atoms.[99,103] Danten, Tassaing, and Besnard performed *ab initio* calculations at the Hartree-Fock and Møller-Plesset-2 levels on complexes of H_2O-C_6F_6 and H_2O-C_6H_6.[98] They found that both complexes have similar binding energies of ~2 kcal/mol, but that the orientation of H_2O with respect to the aromatic ring is opposite in the two complexes.[98,103] For

C_6H_6, H_2O is oriented with its hydrogen atoms toward the π-electron cloud of the aromatic ring. When complexed with C_6F_6, H_2O is in its most stable configuration with the oxygen lone pairs directed towards the ring. Experimental calorimetry studies by Wormald and Wurzberger support the calculations of Danten, Tassaing and Besnard with orientationally averaged binding energies of ~1.3±0.1 kcal/mol for both the hydrogenated and fluorinated benzene-H_2O complexes.[106] Structures of this type are illustrated in Figure 4.1 for the collision systems investigated in this chapter.

In this chapter, the role of preferential hydrogen bonding interactions in collisional energy transfer between highly vibrationally excited donor molecules and H_2O is explored. This chapter focuses on the large-ΔE collisions that scatter H_2O into high energy rotational states (with E_{rot}>1000 cm^{-1}). These collisions correspond to the high energy tail of the vibration-to-rotation/translation (V–RT) energy transfer pathway. The V-RT pathway is the primary means by which highly vibrationally excited molecules relax through collisions at least with small molecular collision partners. The nascent rotational and translational energy distributions of scattered H_2O molecules were measured in order to characterize the nascent rotational and translational energy partitioning in H_2O molecules that scatter from a series of high energy donors that have different π-electron distributions. The donor molecules, pyridine-h_5 (C_5H_5N), pyridine-d_5 (C_5D_5N), and pyridine-f_5 (C_5F_5N), were initially prepared with E~38,300 cm^{-1} by pulsed UV excitation prior to collisions with H_2O at 300 K. The appearance of individual quantum states of scattered H_2O was monitored using high-resolution transient IR absorption at λ=2.7 μm.

Previously, the large-ΔE collisions of highly vibrationally excited pyridine-h_5 with H_2O that lead to rotational and translational excitation of H_2O (000) have been reported.[107] A sensitive test of large-ΔE collisions between vibrationally hot molecules and a 300 K bath is the nascent rotational temperature T_{rot} of scattered bath molecules. Earlier studies on a series of pyridine-based donors have shown that T_{rot} for scattered H_2O (000) molecules (with E_{rot}>1000 cm^{-1}) decreases systematically for donors that have larger size, more vibrational modes, and increased vibrational state density.[21] In this chapter, the three pyridine donors listed above have the same number of vibrational modes (n=27), are of similar size, and can interact with H_2O through both σ– and π–type hydrogen bonding interactions. However, the intermolecular potential energy surface for the fluorinated donor has a minimum with H_2O in the opposite orientation. This is shown in Figure 4.1. Under the experimental conditions used in this study, the presence of stable complexes is unlikely but differences in specific local electrostatic interactions may well influence the energy transfer dynamics. Other differences among these donors are mode frequencies and state densities. We will consider how each of these affects the outcome of large-ΔE collisions.

In this chapter, the nascent energy gain profiles are reported for a number of rotational states of H_2O (000) with E_{rot}>1000 cm^{-1} and H_2O (010) that result from collisions with highly vibrationally excited pyridine-h_5, pyridine-d_5 and pyridine-f_5, each with E~38,300 cm^{-1}. The dynamics of large-ΔE collisions between pyridine-h_5 (E_{vib}= 37,920 cm^{-1}) and H_2O have been investigated previously.[107] In the current study, measurements on pyridine-h_5/H_2O have been repeated and new measurements

on collisions of H_2O with pyridine-d_5 and pyridine-f_5 have been performed using a recently constructed high-resolution transient IR absorption spectrometer. The new measurements show that the high energy tail of the scattered H_2O (000) distribution is affected by the donor identity. The three donors impart roughly the same amounts of translational energy through large-ΔE collisions but there are differences in the rotational distributions of the scattered H_2O molecules. H_2O molecules with E_{rot}>1000 cm^{-1} that scattered from pyridine-h_5 and pyridine-d_5 have essentially the same rotational distribution. When pyridine-f_5 is the donor, however, the nascent rotational temperature of the scattered H_2O decreases by nearly 40%. The implications of these results are discussed in terms of differences in donor/H_2O interactions, donor state density, and donor mode frequencies. This project has been published in the Journal of Physical Chemistry A.[108]

4.2 Experimental Setup

The experimental setup for the high-resolution transient IR F-center laser spectrometer has been described in detail in Chapter 2. Here a brief description of the experimental setup is given. After absorption of a 266 nm photon from the 4th harmonic of a pulsed Nd:YAG laser (2 Hz, 5 ns pulse duration), pyridine-h_5, pyridine-d_5 and pyridine-f_5 undergo rapid radiationless decay to vibrationally excited states with E_{vib}=37,920 cm^{-1}, 38,068 cm^{-1} and 38,836 cm^{-1}, respectively.[62,63,109,110] The radiationless decay of pyridine-h_5 has near unity quantum yield with a lifetime of ~60 ps.[62] Pyridine-d_5 and pyridine-f_5 are expected to have similar quantum yields and radiationless decay lifetimes.[63,110] The 266 nm pump beam was propagated collinearly along a 3 meter Pyrex collision cell with a continuous and tunable single-

mode F-center laser operating at λ~2.7 μm with a resolution of 0.0003 cm^{-1}. The F-center laser was used to probe H_2O rotational transitions within the (001←000) asymmetric stretch vibrational transition. A number of H_2O(000) rotational states with energy between E_{rot}=1000 and 1800 cm^{-1} were investigated. Vibrationally excited H_2O with one quantum in the ν_2 bending mode was probed with the (011←010) transitions.

Pyridine-h_5, pyridine-d_5, or pyridine-f_5 (Acros, 99+ %) and the vapor from HPLC grade H_2O were introduced in a 1:1 mixture, with a total pressure ~25 mTorr, into the flowing gas collision cell. The total average cell pressure was determined using a spectroscopically calibrated manometer thereby accounting for the pressure gradient that exists in a flowing gas system.[108] The total number density at ~25 mTorr is ~8×10^{14} molecules/cm^3. The UV intensity was kept less than 5 MW/cm^2 to minimize multi-photon absorption by the donor molecules. Under these conditions, the fraction of donor molecules that were photo-excited was 15% or less and the average time between collisions was τ_{col}~2.5 μs.

4.3 Results and Discussion

4.3.1 Nascent Transient Absorption of H_2O (000)

H_2O (000) molecules gain rotational and translational energy after single collisions with highly vibrationally excited donor molecules, as shown in Eq. 4.1.

$$\text{Donor}(E_{vib}) + H_2O(298\ K) \rightarrow \text{Donor}(E_{vib} - \Delta E) + H_2O(000, J_{KaKc}, V) \quad \text{(Eq. 4.1)}$$

The scattered H_2O (000) molecules are described by the following: J is the total angular momentum; K_a and K_c are the components of the angular momentum along the A and C molecular axes, respectively; and V is the component of the velocity vector along the IR probe axis. k_2^J is the rate constant for the appearance of a single $J_{Ka,Kc}$ state of H_2O. IR probing of scattered H_2O (000) molecules is described by Eq. 2.

$$H_2O(000, J_{KaKc}, V) + h\nu(\lambda \sim 2.7\ \mu m) \rightarrow H_2O(001, J'_{Ka'Kc'}, V) \qquad \text{(Eq. 4.2)}$$

The collisional relaxation dynamics of the hot donor molecules are characterized by measuring the nascent energy partitioning in scattered H_2O (000) molecules and the absolute rates for energy transfer.

Transient IR absorption signals for appearance of the $J_{Ka,Kc}=8_{4,5}$ rotational state of H_2O (000) following collisions with the hot donors are shown in Figure 4.2. Fractional IR absorption measured at t=1 μs following the UV pulse corresponds to populations of individual H_2O states that result primarily from single collisions with the hot donors. Probing at t=1 μs relative to the τ_{col}~2.5 μs collision time minimizes the effect of secondary collisions that relax the rotational and translational energies of the scattered H_2O (000) molecules. The linearity of the transient signals in Figure 4.2 at early times following UV excitation of donor molecules is indicative of products resulting from single collisions between donor and H_2O. Transient spectra were collected at t=1 μs as a function of probe laser wavelength to obtain Doppler broadened line profiles for scattered H_2O(000), as shown in Figure 4.3 for the

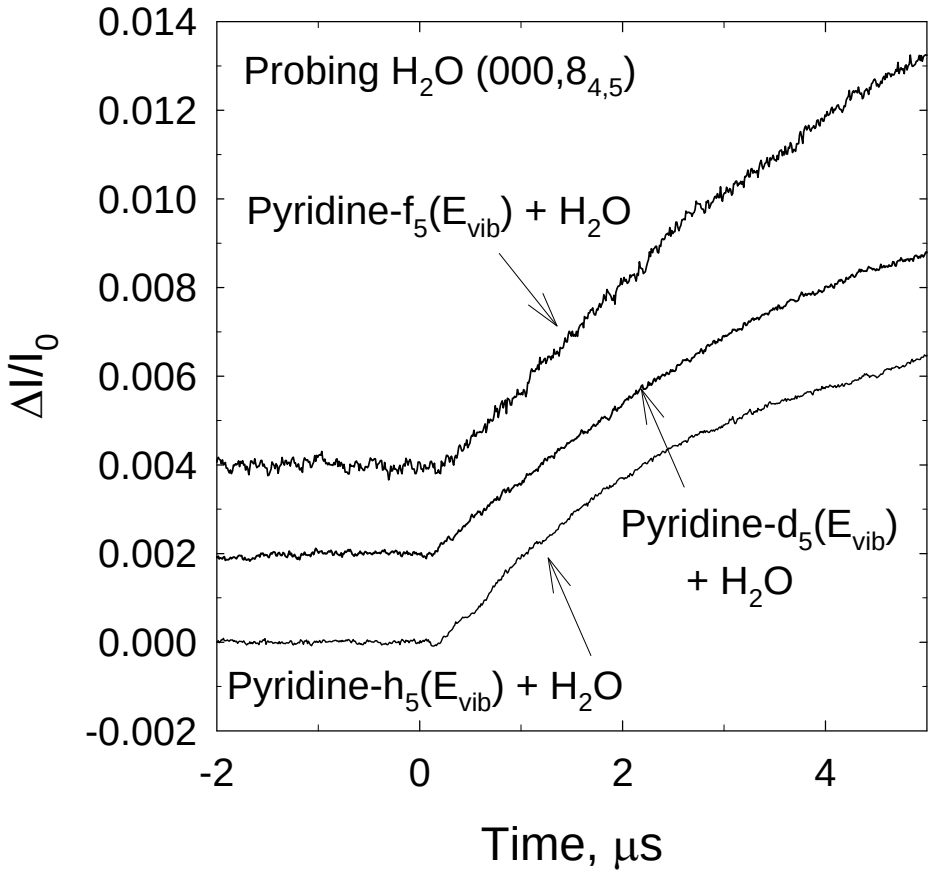

Figure 4.2. Fractional IR absorption of H_2O $(000,8_{4,5})$ following collisions of highly vibrationally excited pyridine-h_5 (E_{vib}=37,920 cm^{-1}), pyridine-d_5 (E_{vib}=38,068 cm^{-1}) and pyridine-f_5 (E_{vib}=38,836 cm^{-1}) with H_2O measured at ν_0 as a function of time following UV excitation. The transient absorption signal for collisions with pyridine-d_5 and pyridine-f_5 are each offset by 0.002 for clarity.

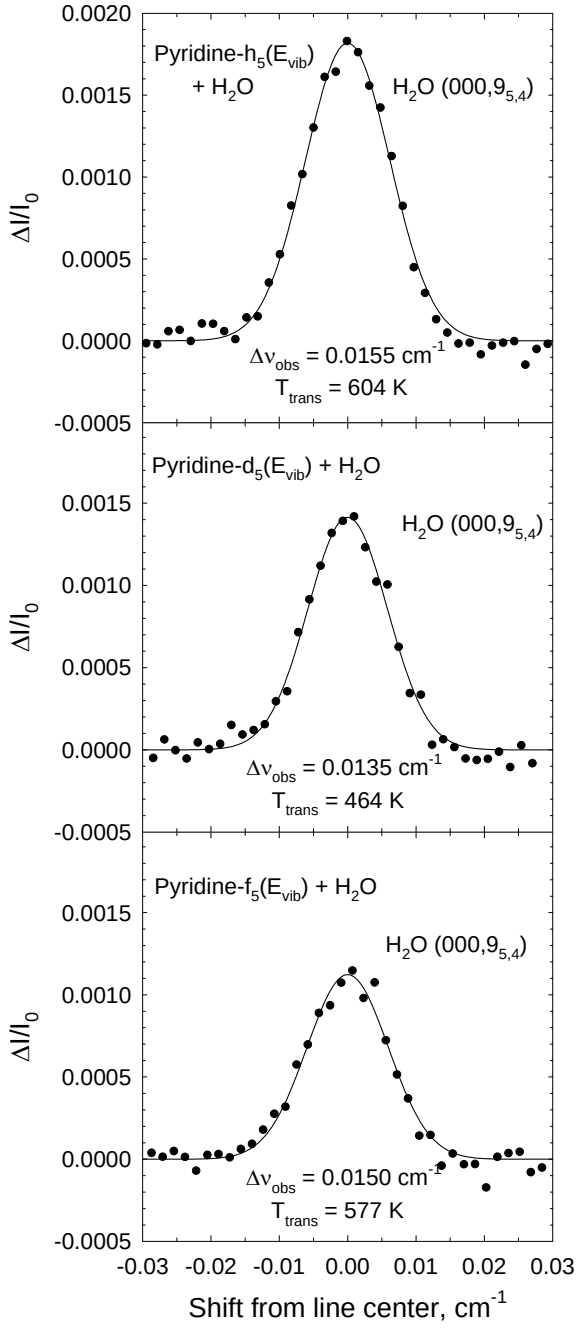

Figure 4.3. Transient absorption lineshapes for H_2O ($000,9_{5,4}$) collected at 1 μs following UV excitation of pyridine-h_5, pyridine-d_5 and pyridine-f_5. The data are fit to a Gaussian function, shown as a solid line.

$J_{Ka,Kc}=9_{5,4}$ state. Nascent velocity distributions of the scattered molecules are obtained from transient line widths. Nascent populations are determined by the area under the transient line profile.

A number of improvements have been made in the new spectrometer to increase the quality of the transient absorption data. Improvements in IR power, beam alignment and detector sensitivity have resulted in a 5-fold increase in signal to noise levels of transient IR absorption measurements and a 3-fold decrease in the detector response time. A new spectroscopic method for measuring total cell pressure gives a more accurate measure of the time between collisions. Together these improvements have lead to transient absorption signals (Figure 4.2) that are of higher quality and are more linear with respect to time than those in the original pyridine-h_5/H_2O study.[107]

In the next section new results for pyridine-h_5/H_2O collisions are presented and compared with the original data. The energy transfer data from the two studies are consistent (with overlapping error bars) but the new energy gain profiles for rotation and translation of H_2O are slightly larger than the original data. The difference in the pyridine-h_5/H_2O results are attributed to the influence of secondary collisions in the original experiments that relaxed the scattered H_2O molecules. Based on the new method of measuring pressure, it is estimated that the original data were collected at a pressure that was ~50% higher than reported, which leads to a 67% drop in the collision time from $\tau_{col}=2.5$ μs to $\tau_{col}=1.6$ μs. Previous transient measurements made at t=1 μs are therefore likely to be affected by secondary collisions. In the current study, data are compared for the three donors that were

collected on the new instrument under similar conditions of pressure and laser power where the influence of secondary collisions is reduced.

4.3.2 Translational Energy Gain of H_2O

The nascent translational energy distributions that result from the large-ΔE collisions of water with pyridine-h_5, pyridine-d_5, and pyridine-f_5 are similar. Translational energy distributions were obtained from Doppler-broadened line widths of H_2O transitions after single collisions with highly vibrationally excited donors. Doppler-broadened line profiles (such as those shown in Figure 4.3) for individual water states measured at t=1 μs after donor excitation were fit using a two-parameter Gaussian function to extract the full-width-half-maximum line width $\Delta\nu_{obs}$ and the intensity at line center. The nascent line widths and translational temperatures (in both the lab frame and the center-of-mass frame) are listed in Table 4.1 for a number of scattered water states with E_{rot}>1000 cm^{-1}. The center-of-mass translational temperatures T_{rel} are a measure of the recoil velocity distribution in the scattered molecules and have values that range from T_{rel}=467±70 K to 738±111 K. Values of T_{rel} are plotted as a function of H_2O rotational energy in Figure 4.4. The new results for pyridine-h_5 are slightly higher than, but within error of, our previous results which are shown as open circles in Figure 4.4 for comparison. The translational energy distributions from the three donors are similar and there is no clear dependence on the water rotational state. The lack of rotational dependence for T_{rel} appears to be a common feature in collisions of water with highly excited molecules and has been observed for both H_2O and HOD.[96,97,107]

Table 4.1. Doppler-broadened linewidths and translational temperatures for strong collisions of $H_2O(000)$ with vibrationally excited pyridine-h_5, pyridine-d_5 and pyridine-f_5.

H_2O (000)		Pyridine-h_5 + H_2O		
$J_{Ka,Kc}$ [a]	E_{rot}, cm^{-1}	$\Delta\nu_{obs}$, cm^{-1} [b]	T_{trans}(lab),K [c]	T_{rel}, K [d]
$8_{3,6}$	1006.1160	0.0163	652±98	733±110
$7_{5,3}$	1059.6470	0.0161	656±98	738±111
$8_{5,4}$	1255.1670	0.0144	532±80	585±88
$8_{6,2}$	1411.6418	0.0150	574±86	636±95
$9_{5,4}$	1477.2970	0.0155	604±91	673±101

H_2O (000)		Pyridine-d_5 + H_2O		
$J_{Ka,Kc}$ [a]	E_{rot}, cm^{-1}	$\Delta\nu_{obs}$, cm^{-1} [b]	T_{trans}(lab),K [c]	T_{rel}, K [d]
$8_{3,6}$	1006.1160	0.0134	437± ± 65	467±70
$7_{5,3}$	1059.6470	0.0140	499±71	542±77
$8_{5,4}$	1255.1670	0.0142	511±72	557±79
$8_{6,2}$	1411.6418	0.0136	472±69	509±75
$9_{5,4}$	1477.2970	0.0135	464±69	500±74
$10_{5,6}$	1718.7188	0.0149	567±76	625±84
$9_{7,2}$	1810.5879	0.0135	470±70	507±75

H_2O (000)		Pyridine-f_5 + H_2O		
$J_{Ka,Kc}$ [a]	E_{rot}, cm^{-1}	$\Delta\nu_{obs}$, cm^{-1} [b]	T_{trans}(lab),K [c]	T_{rel}, K [d]
$8_{3,6}$	1006.1160	0.0166	672±101	711±107
$7_{5,3}$	1059.6470	0.0144	534±80	559±84
$8_{5,4}$	1255.1670	0.0151	578±87	607±91
$9_{5,4}$	1477.2970	0.0150	577±87	607±91
$9_{6,3}$	1631.3831	0.0147	552±83	579±87

[a] J is the total angular momentum, K_a and K_c are the components of the angular momentum along the A and C molecular axes, respectively.

[b] The full width at half maximum linewidth from fitting the t=1 μs transient line profile to a Gaussian function (Figure 4.3). The uncertainty in linewidth measurements is ±0.001 cm^{-1}.

[c] The lab frame translational temperature is found using $T_{trans}(lab) = \left(\frac{mc^2}{8k_B \ln 2}\right)\left(\frac{\Delta\nu_{obs}}{\nu_0}\right)^2$ where m is the mass of H_2O, c is the speed of light, k_B is Boltzmann's constant, ν_0 is the IR transition frequency and $\Delta\nu_{obs}$ is the nascent Doppler-broadened line width.

[d] The center of mass translational temperature for an isotropic distribution of scattered molecules is found using $T_{rel} = T_{trans}(lab) + (T_{trans}(lab) - T_0) \times \left(m_{H_2O}/m_{donor}\right)$ where T_0=298 K is the pre-collision temperature and donor = pyridine-h_5, pyridine-d_5 or pyridine-f_5.

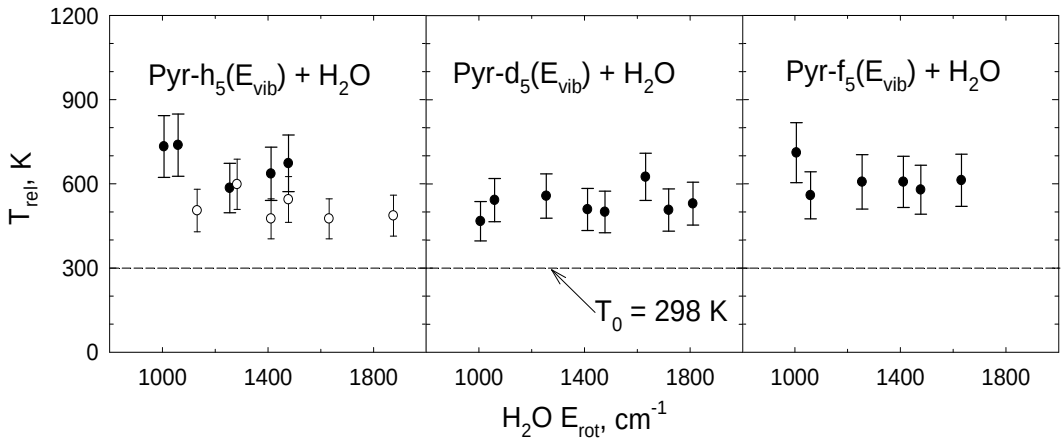

Figure 4.4. Center of mass translational temperatures for pyridine-h_5/H_2O, pyridine-d_5/H_2O, and pyridine-f_5/H_2O shown as a function of H_2O rotational energy following collisional energy transfer.

4.3.3 Rotational Energy Gain of H_2O

The nascent rotational distribution of H_2O (000) molecules scattered from the pyridine donors was determined by measuring the early-time population changes of H_2O rotational states with E_{rot}=1000-1800 cm^{-1}. The rotational distribution for each donor/water pair was measured at t=1 μs following donor excitation and is shown in Figure 4.5. Each data point is the average of at least 3 measurements of an individual water state. Each data set was fit to a Boltzmann distribution with a rotational temperature. The distribution of scattered H_2O from pyridine-h_5 was measured to be T_{rot}=890±150 K. This result is slightly larger than, but within error of, our previous result of T_{rot}=770±80 K.[107] For collisions of H_2O with pyridine-d_5, the scattered H_2O(000) has a rotational temperature of T_{rot}=890±90 K, which is similar to the result for pyridine-h_5/H_2O. Less rotational energy is imparted to the high-J states of water in collisions with pyridine-f_5 where the rotational temperature of scattered water is T_{rot}=530±55 K.

For collisions that result in H_2O(000) scattered into states with E_{rot}=1000-1800 cm^{-1}, the average amount of donor vibrational energy that is converted into water rotation is estimated using $\langle \Delta E_{rot} \rangle = \frac{3}{2} k_B (T_{rot} - T_0)$ and T_0=298 K. In collisions of pyridine-h_5 and pyridine-d_5, the average change in water's rotational energy is $\langle \Delta E_{rot} \rangle$~610 cm^{-1}. Much less energy goes into water rotation through strong collisions with pyridine-f_5 where $\langle \Delta E_{rot} \rangle$~240 cm^{-1}.

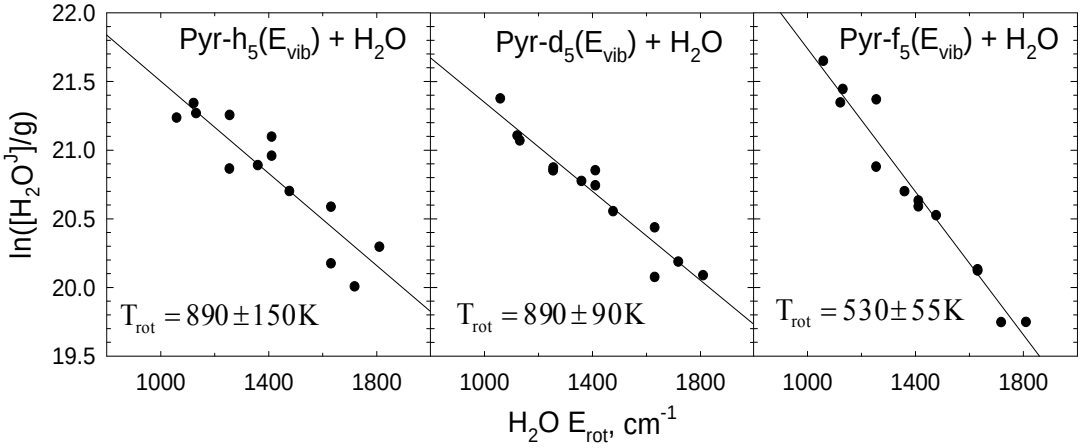

Figure 4.5. The nascent distribution of H_2O (000) rotational states after single collisions with pyridine-h_5, pyridine-d_5, and pyridine-f_5. Data are collected at 1 μs following donor excitation. Each point represents an average of three independent measurements.

4.3.4 Energy Transfer Rates of Donor/H_2O

Absolute rate constants (k_2^J in Eq. 4.1) for energy gain in individual H_2O states were determined for each donor molecule to establish the importance of vibration-to-rotation/translation (V→RT) energy transfer. Table 4.2 lists the energy transfer rate constants measured in this study. Detailed information on determining the energy transfer rate for H_2O individual J states is shown in Appendix C. Here a brief summary is given. The energy transfer rate constant k_2^J for energy gain in H_2O after single collisions with highly vibrationally excited pyridine donors is given by Eq. 4.3

$$k_2^J = \frac{\Delta[H_2O^J]}{[H_2O]_0[Donor^E]_0\,\Delta t} \qquad \text{(Eq. 4.3)}$$

In Eq. 4.3, $[H_2O]_0$ is the bulk H_2O concentration at 298 K while $[H_2O^J]$ is the population of scattered H_2O molecules in a rotationally excited J state after a time interval Δt. $[Donor^E]_0$ is the concentration of highly vibrationally excited pyridine-h_5, pyridine-d_5, or pyridine-f_5 determined from the 266 nm UV absorption. $[Donor^E]$ at 1 μs is essentially the same as the initial value $[Donor^E]_0$, based on the method of initial rates and an average collision time of τ_{col}~2.5 μs. The absolute rate was measured for a single state and the nascent rotational temperatures were used to get rates for the distribution for pyridine-h_5/H_2O, pyridine-d_5/H_2O and pyridine-f_5/H_2O collisions, as discussed in Section 4.3.3.

Table 4.2. Appearance rates for H_2O (000, $J_{Ka,Kc}$) following collisions with pyridine-h_5 (E_{vib}=37,920 cm^{-1}), pyridine-d_5 (E_{vib}=38,068 cm^{-1}) and pyridine-f_5 (E_{vib}=38,836 cm^{-1}).

$$\text{Donor } (E_{vib}) + H_2O \xrightarrow{k_2^J} \text{Donor } (E_{vib}-\Delta E) + H_2O\ (000, J_{Ka,Kc})$$

Donor = pyridine-h_5, pyridine-d_5 or pyridine-f_5

J_{KaKc}	ν_0, cm^{-1}	[a] E_{rot}, cm^{-1}	[b] k_2^J, 10^{-12} cm^3 $molecule^{-1}$ s^{-1}		
			Pyridine-h_5	Pyridine-d_5	Pyridine-f_5
$7_{5,3}$	3723.273	1059.6467	2.0±0.6	2.2±0.6	2.2±0.7
$8_{4,5}$	3739.095	1122.7085	6.3±1.9	6.6±2.0	6.2±1.9
$8_{4,4}$	3719.762	1131.7756	2.1±0.6	2.2±0.7	2.2±0.7
$8_{5,4}$	3721.878	1255.1667	5.1±1.5	5.3±1.6	4.3±1.3
$8_{5,3}$	3720.131	1255.9115	1.7±0.5	1.8±0.5	1.4±0.4
$9_{4,5}$	3706.841	1360.2354	4.7±1.4	5.0±1.5	3.6±1.1
$8_{6,3}$	3710.781	1411.6115	3.9±1.2	4.1±1.2	2.8±0.8
$8_{6,2}$	3710.706	1411.6418	1.3±0.4	1.4±0.4	0.9±0.3
$9_{5,4}$	3716.160	1477.2974	3.9±1.2	4.1±1.2	2.7±0.8
$9_{6,4}$	3708.597	1631.2455	1.0±0.3	1.1±0.3	0.6±0.2
$9_{6,3}$	3708.258	1631.3831	3.1±0.9	3.2±1.0	1.8±0.5
$10_{5,6}$	3712.379	1718.7188	2.9±0.9	3.1±0.9	1.5±0.5
$9_{7,2}$	3696.887	1810.5879	2.3±0.7	2.4±0.7	1.1±0.3
[b] k_2^{int}, 10^{-10} cm^3 $molecule^{-1}$ s^{-1} for E_{rot}=1000-1800 cm^{-1}			1.7±0.4	1.8±0.4	1.4±0.3

[a)]The energy in cm^{-1} of the $J_{Ka,Kc}$ rotational states of H_2O (000) from the HITRAN spectral database[81].

[b)]The integrated energy transfer rate constant k_2^{int} for energy gain in H_2O (000) is determined by summing over the H_2O (000) states with E_{rot}=1000-1800 cm^{-1}.

Energy gain rate constants for individual H_2O states between E_{rot}=1000 and 1800 cm^{-1} in Table 4.2 were summed to yield integrated rate constants k_2^{int} that are listed in Table 4.3 for each donor/H_2O pair. These rates correspond to the subset of V→RT collisions that have large ΔE values. The similarity of the integrated rates for strong collisions shows that all these donors have comparable probabilities of strong collisions. Pyridine-h_5/H_2O and pyridine-d_5/H_2O have k_2^{int} values of k_2^{int}~$(1.8\pm0.4)\times10^{-10}$ cm^3 $molecule^{-1}$ s^{-1}. Pyridine-f_5/H_2O has a lower k_2^{int} value, with k_2^{int}=$(1.4\pm0.3)\times10^{-10}$ cm^3 $molecule^{-1}$ s^{-1}. These values are similar within the experimental uncertainty.

Determining the total V→RT energy transfer rate constant k_{TOT} requires information about the low energy water states with E_{rot}<1000 cm^{-1}, which have not been measured. Extrapolating the T_{rot} values for large-ΔE collisions to low-energy water states leads to an estimate of total V→RT energy transfer rates that are just slightly larger than the Lennard-Jones collision rates. This suggests that most quenching collisions involve the V→RT pathway and that V→RT energy transfer occurs on essentially every collision. These values are listed in Table 4.3. As a cross check, the rate of vibration-to-vibration (V→V) energy transfer for pyridine-f_5/H_2O collisions was measured. Excitation of the (010) bending mode of water occurs at a rate that is only ~2% of the Lennard-Jones collision rate. This result will be presented in section 4.3.8. Energy transfer to the higher frequency (001) and (100) stretching modes of water was not observed.

Table 4.3 lists the total rate constants for each donor/H_2O pair. Both pyridine-h_5/H_2O and pyridine-d_5/H_2O have k_{TOT} values of $k_{TOT}=7\times10^{-10}$ cm^3 $molecule^{-1}$ s^{-1} and

Table 4.3. Comparison of integrated energy transfer rates (k_2^{int}), total collision rates, and Lennard-Jones collision rates.

Donor molecules	k_2^{int} 10^{-10} cm^3 molecule^{-1} sec^{-1}	$k_{TOT} = \sum_{all\ J} k_2^J$ 10^{-10} cm^3 molecule^{-1} sec^{-1}	[a)]k_{LJ} 10^{-10} cm^3 molecule^{-1} sec^{-1}
H_2O E_{rot} range	1000 – 1800 cm^{-1}	0 – 3000 cm^{-1}	
pyridine-h_5	1.7±0.4	6.9±1.7	6.15
pyridine-d_5	1.8±0.4	7.3±1.8	6.12
pyridine-f_5	1.4±0.3	10.7±3.2	6.44

[a)]The collision rate constants were determined using a Lennard-Jones (LJ) potential as the intermolecular potential during the donor/H_2O collisions. The method of getting the collision rate constants is described in Appendix B.

agree within experimental uncertainty. Specifically, pyridine-h_5/H_2O k_{TOT} is $k_{TOT}=(6.9\pm1.7)\times10^{-10}$ cm^3 $molecule^{-1}$ s^{-1} while k_{TOT} for pyridine-d_5/H_2O was found to be $k_{TOT}=(7.3\pm1.8)\times10^{-10}$ cm^3 $molecule^{-1}$ s^{-1}. The energy transfer rate for pyridine-f_5/H_2O is $k_{TOT}=(10.7\pm3.2)\times10^{-10}$ cm^3 $molecule^{-1}$ s^{-1}, which is ~50% larger than the pyridine-h_5/H_2O and pyridine-d_5/H_2O energy transfer rates.

The energy transfer probability distribution function P(ΔE) shows the dependence of the energy transfer probability on the ΔE, amount of energy loss caused by collisions with H_2O. Here, the energy transfer probability for strong collisions of each donor/H_2O pair is investigated. The key idea is to convert from state- and velocity-indexed data to a ΔE-indexed probability. The method of calculating P(ΔE) has been described in detail[82] and the specific treatment for H_2O has been described in a previous paper.[96] The P(ΔE) curve is the summation of all the state-specific $P_J(\Delta E)$ curves. The state-specific energy transfer probability $P_J(\Delta E)$ was determined by the ratio of the energy transfer rate constant k_2^J to the total collision rate and the Doppler-broadened velocity distributions of the scattered molecules. Here we use the Lennard-Jones collision rates for collision rate. Detailed information of calculating Lennard-Jones collision rates for donor/H_2O pair is described in Appendix B. The amplitude of P(ΔE) describes the propensity of an energy transfer event assuming that the Lennard-Jones model properly describes the total collision rate. The P(ΔE) curves are shown in Figure 4.6 for different pyridine donors. From Figure 4.6, strong collision probabilities with H_2O have the following order, pyridine-h_5 > pyridine-d_5 > pyridine-f_5.

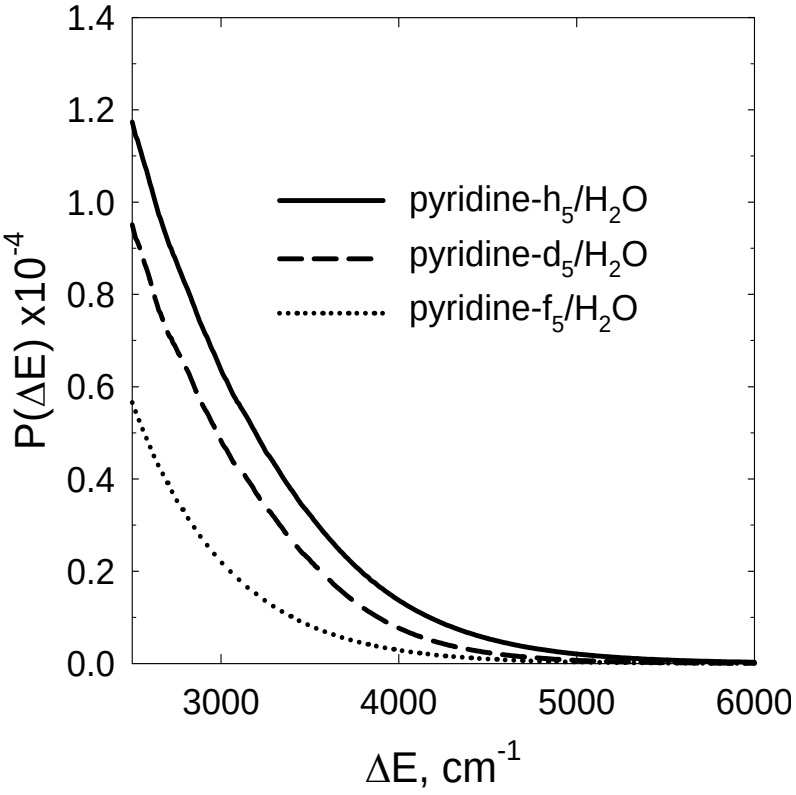

Figure 4.6. P(ΔE) curves for strong collisions based on transient data of H_2O and vibrationally excited pyridine-h_5 (solid line), pyridine-d_5 (dashed line), and pyridine-f_5 (dotted line). Appearance of scattered H_2O molecules is characterized by a nascent rotational distribution and each rotational state has a velocity distribution based on the Doppler-broadened linewidths. Probabilities for strong collisions are pyridine-h_5 > pyridine-d_5 > pyridine-f_5.

4.3.5 Role of Donor Vibrational Mode Frequencies

The state-resolved scattering measurements provide insight into the dynamics of large-ΔE collisions in molecules that have preferential hydrogen bonding interactions with water. The measured energy gain of H_2O shows that the scattering dynamics for H_2O with pyridine-h_5 and pyridine-d_5 are essentially the same. In collisions with pyridine-f_5, however, H_2O is scattered with substantially less rotational energy. A number of factors may explain why H_2O gains more rotational energy in collisions with pyridine-h_5 and pyridine-d_5 than with pyridine-f_5. One possibility is that differences in the vibrational frequencies of the donor molecules are responsible. Vibrational frequencies depend on the reduced mass and the force constant of the vibrational mode. For these donors the effective reduced mass of the C–X bond increases from μ=1 amu when X is H, to μ= 2 amu when X is D and to μ~17 amu when X is F, leading to a reduction in vibrational frequencies as the atom X becomes more massive. Figure 4.7 shows how vibrational energy is distributed among the donor vibrational modes, assuming a statistical distribution. Figure 4.7 shows that the C–X stretch frequencies are ~3050 cm^{-1} for pyridine-h_5, ~2270 cm^{-1} for pyridine-d_5 and ~1550 cm^{-1} for pyridine-f_5.[111,112] The out-of-plane-bending modes and other low frequency modes are also affected by the mass of X and the oscillator force constants. The low frequency modes of pyridine-h_5, pyridine-d_5 and pyridine-f_5 are in the range of ν~390-990 cm^{-1}, ~340-820 cm^{-1} and ~170-650 cm^{-1}, respectively.[111,112] The average energy per vibrational mode is calculated based on statistical distribution of internal energy using a direct sum of states.[113] Frequencies

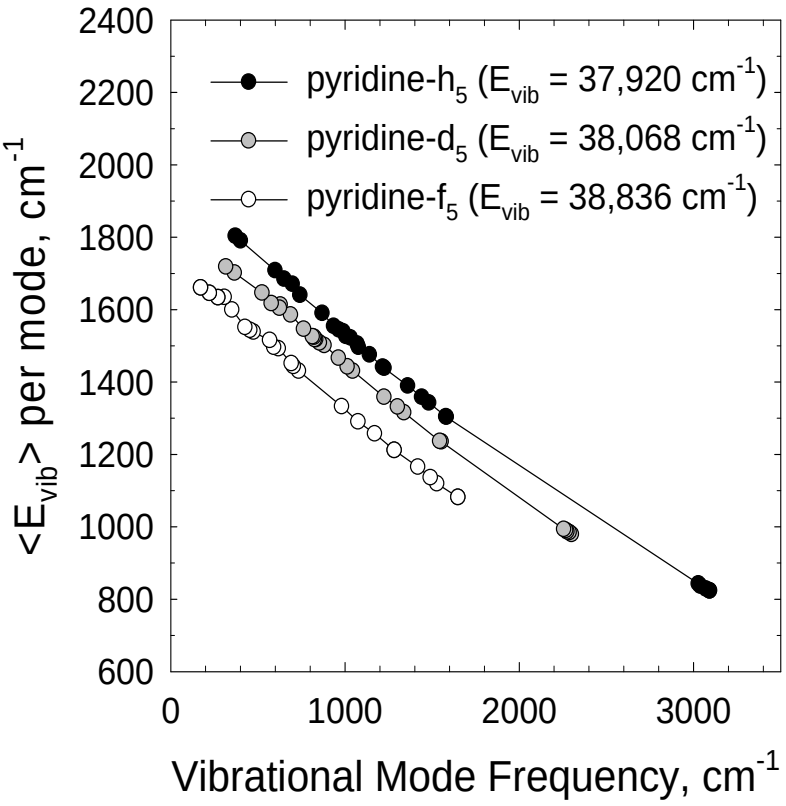

Figure 4.7. Average energy per vibrational mode in pyridine-h_5 (black dots), pyridine-d_5 (grey dots) and pyridine-f_5 (circles) following excitation with 266 nm UV light.

of pyridine-h_5 and pyridine-d_5 are given by Wong and Colson[111] and assigned by Maris *et al*.[114] Frequencies of pyridine-f_5 by Long and Steele[112] are used.

A number of experimental and theoretical studies indicate that the low frequency modes of highly excited molecules are the most relevant modes for collisional energy transfer.[43,71,115] Based on this, we might expect that collisions with pyridine-f_5 would impart larger amounts of energy to the scattered water molecules, which is not observed in our measurements. In addition, if donor vibrational frequencies influence the large-ΔE collisions, we would expect to see differences between the pyridine-h_5 and pyridine-d_5 donors, which are not observed. Our results are consistent with those from other studies showing that deuteration of highly vibrationally excited donor molecules has little effect on average energy transfer behavior.[71,116] Of course, the measurements in the current study are focused on the dynamics of the high energy tail of the V-RT pathway and do not include information about small-ΔE collisions. It may be that the small-ΔE collisions are sensitive to differences in donor vibrational frequencies.

4.3.6 Role of Donor State Density

Here the influence of donor state density is discussed. Collisional energy transfer of highly vibrationally excited molecules is known to be affected by changes in the vibrational state density of the donor. Increasing donor state density tends to enhance energy transfer probabilities. Beyond general trends, high resolution IR studies have shown that the curvature of the high energy tail of the energy transfer distribution function correlates with the energy dependence of the donor state density for collisions in a CO_2 bath.[23] A related dependence on state-density has been seen in

the rotational distributions of scattered water molecules in collisions with highly excited donors.[21] The GRETCHEN model (described in Section 3.3.6) for large-ΔE collisions is based on Fermi's Golden Rule and outlines this state density dependence.[21,23] Statistical theories inherently include state density in collisional energy transfer, and recent developments in the Partially Ergodic Collision Theory of Nordholm and coworkers consider subspaces of state density that are in agreement with the KCSI experiments of Luther and coworkers.[33-35]

The donor molecules studied here have state densities at E~38,300 cm^{-1} of $\rho=6.24\times10^{13}$ states/cm^{-1} for pyridine-h_5, $\rho=1.90\times10^{15}$ for pyridine-d_5 and 1.48×10^{20} for pyridine-f_5. The state density of the fluorinated donor has the strongest energy dependence of these donors, and we observe that pyridine-f_5 imparts the smallest amount of rotational energy to H_2O. The rotational energy gain profiles for water following collisions with pyridine-h_5, pyridine-d_5, and pyridine-f_5 agree reasonably well with predictions from the GRETCHEN model, but there is some discrepancy for pyridine-h_5 and pyridine-d_5. The GRETCHEN model predicts that T_{rot} for pyridine-d_5 collisions should be slightly less than for pyridine-h_5, but this is not observed. However the state density difference in these donors is not very large and the difference in their energy dependence is even smaller, so differences in the scattering results may be within our experimental uncertainty. The energy transfer probability parameter β_{obs} and state density parameter β_ρ is show in Table 4.4. β_{obs} values for 2-methyl-pyridine (2-picoline) and 2,6-dimethyl-pyridine (2,6-lutidine) with H_2O are also calculated based on previous results.[21,22]

Table 4.4. The energy transfer probability parameter β_{obs} of the P(ΔE) at high energy tail (ΔE>3000 cm^{-1}) and highly vibrationally excited donor molecules state density parameter β_ρ for different donor/H_2O pairs.

Donor molecules	E_{vib}, cm^{-1}	β_{obs}, $10^{-4}/cm^{-1}$	β_ρ, $10^{-4}/cm^{-1}$
pyridine-h_5[a)]	37920	20.0	5.48
pyridine-d_5[a)]	38068	25.7	5.77
pyridine-f_5[a)]	38836	22.3	6.23
2-picoline[b)]	38313	20.5	6.87
2,6-lutidine[b)]	38702	21.5	8.07

[a)]Data taken from this work

[b)]Data taken from the work by Elioff et al[21]

It is interesting that if both the rotational energy and translational energy exchanges are considered, the correlation of the energy transfer P(ΔE) curvature and the energy dependence of the donor state density washes out for these donor/H_2O pairs, as shown in Figure 4.8. The Doppler-broadened line widths for water do not increase as a function of rotational state, giving similar translational energy distributions to each rotational state of H_2O. This tends to flatten out the overall energy transfer distribution function for large-ΔE collisions. This situation is quite different from CO_2 collisions, where extensive line broadening is observed for scattering to high rotational states.[117,118] It may be that for strongly interacting collision partners, such as aromatic donors with water, the attractive interactions outweigh the impulsive nature of the collisions leading to different state density effects. The fact that we do not observe differences in the scattering dynamics of H_2O from pyridine-h_5 and pyridine-d_5, but do see differences for collisions with pyridine-f_5, suggests that electrostatic interactions and not state density difference, are important in the large-ΔE collisions of water.

4.3.7 Preferential Hydrogen Bonding Effects

In this section we consider how differences in the intermolecular potential energy surfaces of water with pyridine-h_5, pyridine-d_5 and pyridine-f_5 might affect the types of motions that water undergoes in collisions with these highly excited donors. The interaction of water with each of these donors has energy minima in the σ– and π–hydrogen bonding orientations, as shown in Figure 4.1. It is possible that water moves from one energy minimum to the other during collisions and that this type of

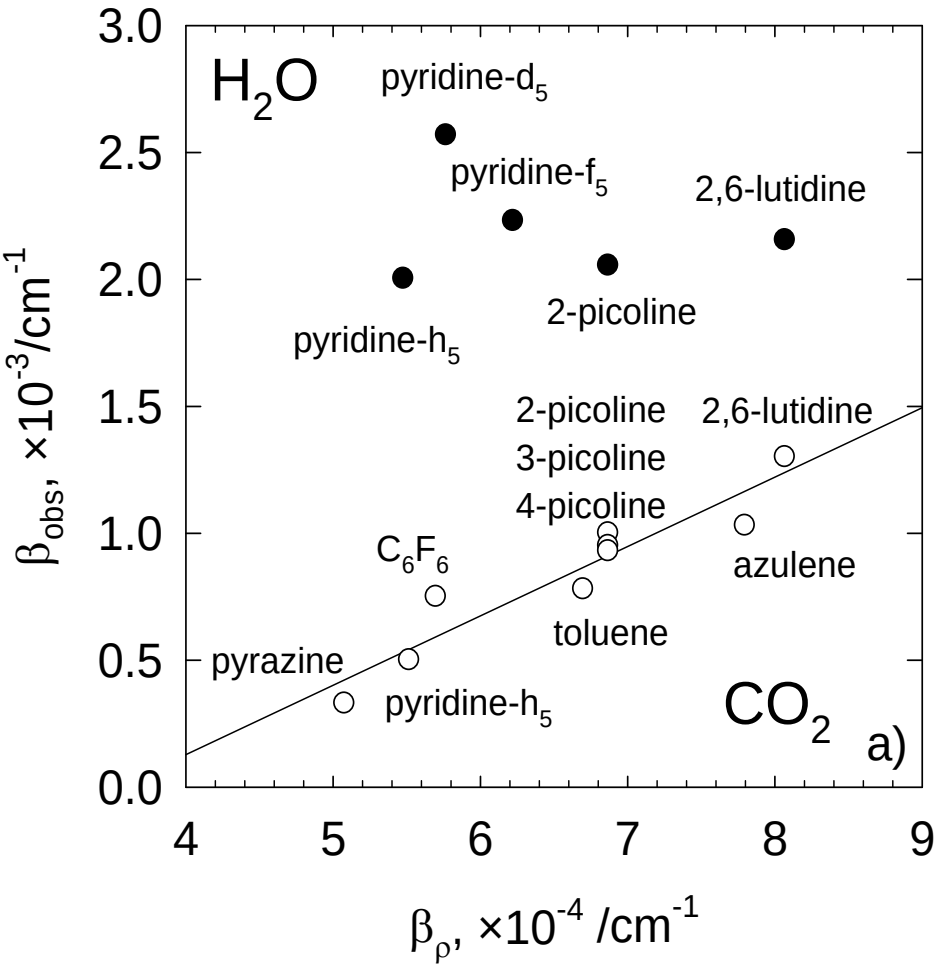

Figure 4.8. Correlation diagram of the energy transfer probability parameter β_{obs} with the state density parameter β_ρ for collisional quenching of highly vibrationally excited azabenzenes with H_2O (top/symbols). The literature correlation for CO_2 as a bath is shown for comparison.

motion influences the partitioning of energy in the scattered water molecules. The photo-induced shuttling of water between different hydrogen bonding sites has been observed for stable complexes of trans-formaniline in experiments by Zwier and coworkers.[119] Motion of water from a π-configuration to a σ-configuration (and vice versa) is likely to promote rotational energy in the scattered bath molecules. If this type of directed motion of water occurs in collisions with highly excited pyridine donors, then donors for which water can more easily move between σ– and π-sites are expected to impart more rotational energy to water.

As discussed in Section 4.1, the π-complexes of water with pyridine-h_5 and pyridine-d_5 are likely to have minimum energy configurations that are roughly that of benzene-H_2O, with the hydrogen atoms of water directed toward the electron-rich π-cloud.[98,103] The π-complexes of pyridine-f_5 are likely to be similar in structure to those of C_6F_6-H_2O, with the hydrogen atoms of water directed away from the π-cloud.[98] For the C_6H_6 complex, water is ~3 Å from the π -cloud as compared to a distance of ~4 Å in H_2O-C_6F_6. The interaction energies of these complexes are similar, both ~2 kcal/mol. In collisions of the type we have studied, it is unlikely that multiple shuttling events occur between the σ– and π– sites, just as it is unlikely that stable complexes are formed. It is possible however that the ease with which water moves between σ– and π– sites on the donors affects the amount of rotational energy it gains during collisions. Directed movement of water between σ– and π–sites on pyridine-h_5 and pyridine-d_5 is likely to be easier than for pyridine-f_5 given the proximity of the hydrogen atoms to the aromatic ring and the simpler motion required to move between σ– and π–orientations. On the other hand, the reversed orientation

of water in the fluorinated complex is likely to hinder its ability to move between the σ– and π– orientations. Taken together, this situation would impart less rotational energy to water and may be one reason that water is scattered from pyridine-f_5 with less rotational energy. Of course, collisions occur over a wide range of initial impact parameters and orientations and the σ–π hydrogen bonding swapping mechanism discussed here describes just one type of collisional encounter. Nevertheless, the σ– and π-hydrogen bonded orientations are the global minima in the intermolecular potential energy surface of water with pyridine. The ease with which water can move between these sites, and the extent to which these forces direct its motion, are likely to influence molecular collisions. The scattering data reported here are consistent with the type of torque-inducing interactions described above.

Computer simulations of collisions between highly vibrationally excited pyridine-h_5, pyridine-d_5, and pyridine-f_5 with water are expected to provide insight into the importance of this phenomenon in the collisional quenching of highly excited molecules with water.

4.3.8 V→V Energy Transfer of Pyridine-f_5 and H_2O

The vibration to vibration (V→V) energy transfer channel for collisional quenching of highly vibrationally excited pyridine-f_5 and H_2O was measured. The results show that the V→V energy transfer channel is not the primary collisional quenching channel, accounting for only 2% of the total energy transfer rate. In this section, detailed information about the translational and rotational energy partitioning and the energy transfer rate is presented for the H_2O (010) state. The appearance of vibrationally excited water (010) from collisions with highly vibrationally excited

pyridine-h_5 and pyridine-d_5 was also checked, but the transient IR signals for this state were below our detection limit.

Vibration to vibration energy transfer between highly vibrationally excited pyridine-f_5 and room temperature H_2O molecules is shown in Eq. 4.4.

$$\text{Pyridine-f}_5(E_{vib}) + H_2O(298\ K) \rightarrow \text{Pyridine-f}_5(E_{vib}-\Delta E) + H_2O(010, J_{KaKc}, V) \quad \text{(Eq. 4.4)}$$

IR probing of H_2O (010, J_{KaKc},V) molecules is given by Eq. 4.5.

$$H_2O\ (010, J_{KaKc}, V) + IR \rightarrow H_2O\ (011, J'_{Ka'Kc'}, V) \quad \text{(Eq. 4.5)}$$

Here (011) refers to a combination state with one quantum in the H_2O asymmetric stretch and one quantum in the H_2O bend.

Figure 4.9 shows the fractional transient absorption $\Delta I/I_0$ of H_2O (010, 1_{01}) transition. Translational energy gain of H_2O (010) was measured by the Doppler-broadened line widths of scattered H_2O (010) molecules. A Doppler-broadened line shape for H_2O (010, 1_{01}) is shown in Figure 4.10. A summary of a series of linewidth measurements is listed in Table 4.5 along with the corresponding translational temperatures for several rotational states of H_2O (010). Center of mass translational temperatures, T_{rel}, of scattered H_2O (010) are plotted in Figure 4.11. It is shown in Figure 4.11 that all T_{rel} values are ~540 K and are independent of the rotational energy E_{rot}.

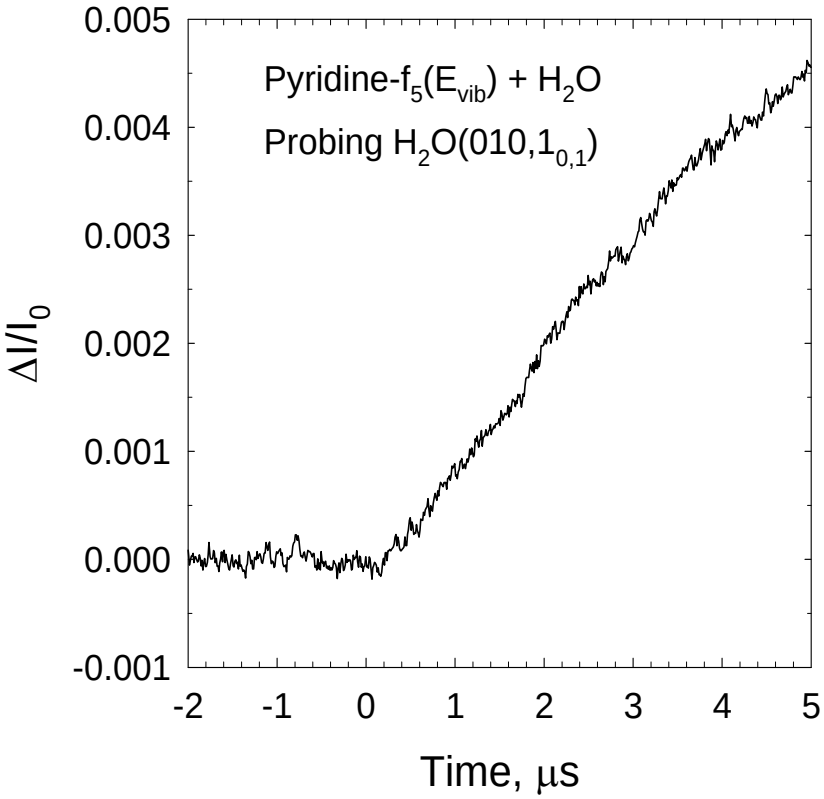

Figure 4.9. Fractional IR absorption of H_2O $(010,1_{0,1})$ following collisions of highly excited pyridine-f_5 (E_{vib}=38,836 cm^{-1}) with H_2O measured at ν_0 as a function of time following UV excitation of pyridine-f_5.

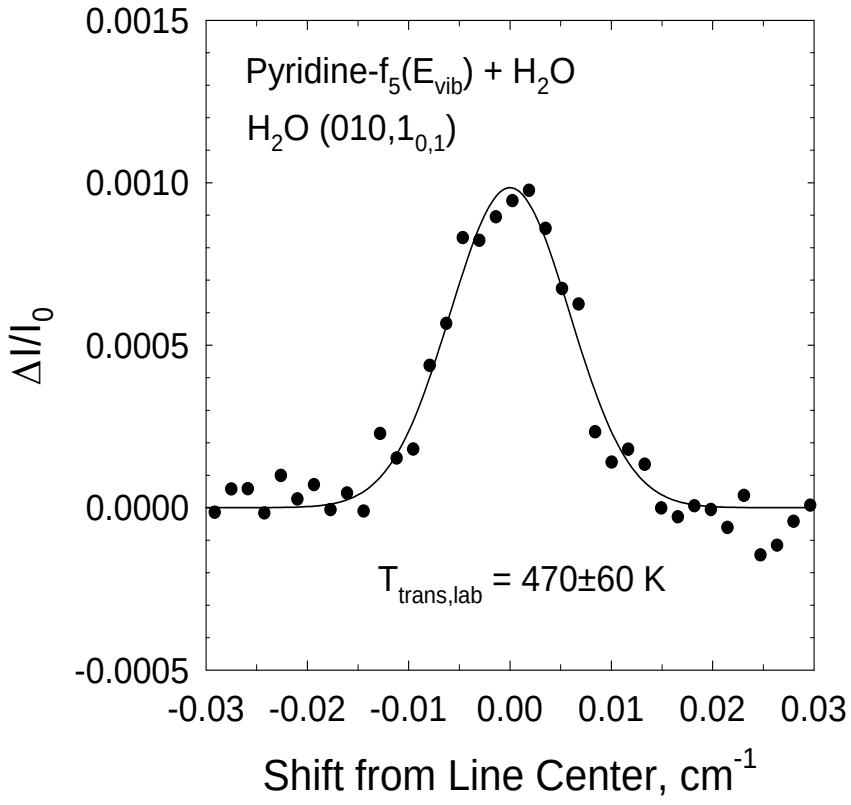

Figure 4.10. Transient absorption lineshapes for H_2O $(010,1_{0,1})$ collected at 1 μs following UV excitation of pyridine-f_5. The data (symbols) are fit to a Gaussian function shown as a solid line.

Table 4.5. Doppler-broadened linewidths and translational temperatures of H_2O (010) after collisions with vibrationally excited pyridine-f_5.

$J_{Ka,Kc}$	E_{rot}, cm^{-1} [a]	$\Delta\nu_{obs}$, cm^{-1}	T_{trans}(lab), K [b]	T_{rel}, K [c]
$1_{0,1}$	23.8110	0.0138	466±62	483±70
$3_{0,3}$	137.1504	0.0148	528±70	552±79
$3_{2,1}$	224.5888	0.0148	525±70	549±79
$5_{0,5}$	326.0202	0.0151	539±72	564±81

[a] The full width at half maximum linewidth from fitting the t=1 μs transient line profile to a Gaussian function (Figure 4.8). The uncertainty in linewidth measurements is ±0.001 cm^{-1}.

[b] The lab frame translational temperature is found using $T_{trans}(lab) = \left(\frac{mc^2}{8k_B \ln 2}\right)\left(\frac{\Delta\nu_{obs}}{\nu_0}\right)^2$ where m is the mass of H_2O, c is the speed of light, k_B is Boltzmann's constant, ν_0 is the IR transition frequency and $\Delta\nu_{obs}$ is the nascent Doppler-broadened line width.

[c] The center of mass translational temperature for an isotropic distribution of scattered molecules is found using $T_{rel} = T_{trans}(lab) + (T_{trans}(lab) - T_0) \times \left(m_{H_2O}/m_{donor}\right)$ where T_0=298 K is the pre-collision temperature and donor=pyridine-f_5.

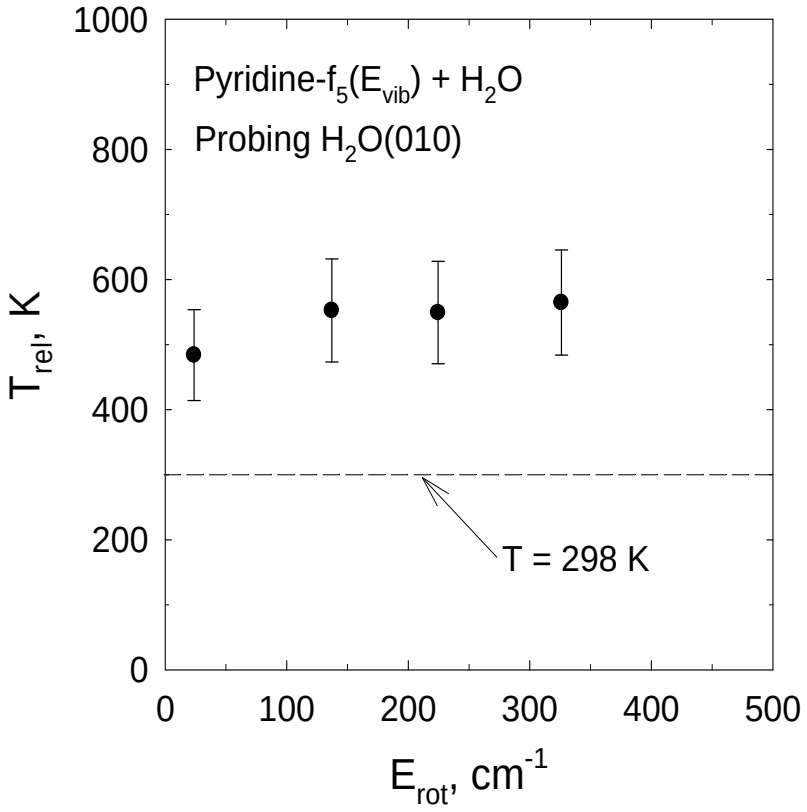

Figure 4.11. Center of mass translational temperatures for H_2O (010) shown as a function of H_2O rotational energy following collisions with highly vibrationally excited pyridine-f_5.

The rotational distribution of scattered H_2O (010) state was obtained by measuring the absolute populations of different states for scattered H_2O molecules. The nascent rotational distribution of scattered H_2O (010) is shown in Figure 4.12. The rotational temperature of scattered H_2O (010) from the V→V channel is T_{rot}=430±90 K. This indicates that very little rotational energy gain accompanies vibrational excitation of water in collision with pyridine-f_5.

Collisional energy transfers can happen either through short-range repulsive intermolecular forces or through long-range attractive interactions.[120-122] Energy transfer mediated by repulsive interactions is generally accompanied by rotational and translational energy gain in the products. Near-resonance couplings leading to V→V energy transfer do not rely on impulsive interactions. They can proceed through long-range attractive interactions and this process usually results in small amounts of translational and rotational energy in the collision products.[122] Theoretical investigations have shown that long range coupling between transition moments induces vibrational energy transfer between two IR active modes.[123,124] During this process, the rotational energy gain is determined by the optical selection rules. For instance, $\Delta J=\pm 1$ in a pure dipole-dipole interaction. Impulsive collisions can also lead to V→V energy transfer but this process is orientationally constrained and generally occurs with small probability. The products of impulsive V→V energy transfer will have relatively large translational and rotational energies.

Long range interaction is enhanced when the energy gap between donor and bath vibration is small. As mentioned in Section 4.3.4, in pyridine-f_5, the C-F stretches are ~1650 cm^{-1},[112] in near resonance with the H_2O bend at ~1595 cm^{-1}. The

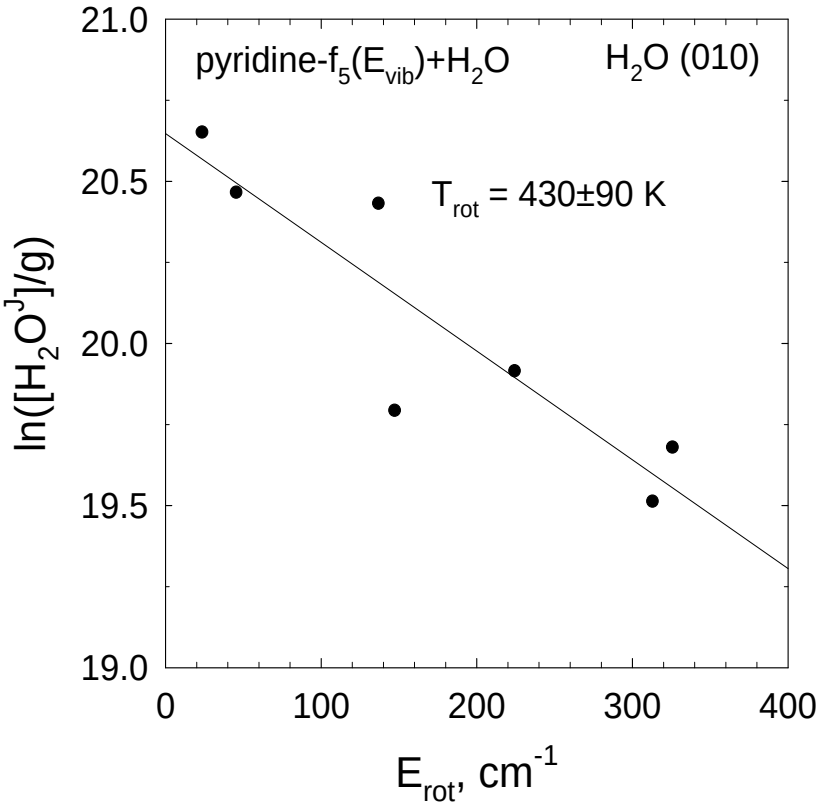

Figure 4.12. The nascent rotational distribution of H_2O (010) states after single collisions with highly vibrationally excited pyridine-f_5. Data are collected at 1 μs following donor excitation. Each point for pyridine-f_5 represents an average of three independent measurements. Since the line widths for H_2O $(010,1_{1,0})$, $(010,2_{2,1})$ and $(010,4_{2,3})$ were not measured, a linear fitting was used to estimated the linewidth values from Figure 4.9.

probability of near resonant energy transfer from highly vibrationally excited pyridine-f_5 and H_2O is likely to be enhanced relative to other non-resonant energy transfer events. Vibrational excitation at H_2O symmetric stretch (3657 cm^{-1}) and antisymmetric stretch (3756 cm^{-1}) is not likely to happen since both of them are of larger frequency than any single vibration in pyridine-f_5.

4.3.9 Comparison of Energy Transfer of Pyridine-d_5 and Pyrazine with H_2O

Here we compare the V→V energy transfer of pyridine-f_5/H_2O to previous results for pyrazine/H_2O collisions.[125] As shown in Table 4.6, the rotational temperature of scattered H_2O (010) from the V→V channel is T_{rot}=430±90 K. The V→RT channel scatters H_2O (000) has a higher rotational distribution of T_{rot}=530±30 K. This corresponds to an average change in rotational energy of $\langle\Delta E_{rot}\rangle$~140 and $\langle\Delta E_{rot}\rangle$~240 cm^{-1}, respectively, where the change in rotational energy is determined by $\langle\Delta E_{rot}\rangle = \frac{3}{2}k_B(T_{rot} - T_0)$, in which T_0=298 K. Near resonant energy transfer was also observed due to the resonance of H_2O bend with C-C stretches on pyrazine ring, which are ~1563 cm^{-1} as shown in Figure 4.13.[126] In collisions with pyrazine (E_{vib}=37,900 cm^{-1}) the scattered H_2O (010) has a rotational temperature of T_{rot}=630±90 K from the V→V channel. The V→RT pathway for pyrazine/H_2O collisions leaves H_2O (000) with rotational temperature of T_{rot}=920±120 K. The average changes in rotational energy for these pathways are $\langle\Delta E_{rot}\rangle$~350 and $\langle\Delta E_{rot}\rangle$~650 cm^{-1}. It shows that V→RT pathway has more rotational energy gain in than V→V channel for both donors.

Table 4.6. Comparison of nascent rotational partitioning and energy transfer rates (k_2^{int}) and Lennard-Jones collision rates for H_2O (010) (V→V channel) and H_2O (000) (V→RT channel).

Donor Molecule	Pyridine-f_5		Pyrazine-h_4	
Pathway	V→V	V→RT	V→V	V→RT
T_{rot}, K	430±90	530±30	630±90	920±120
ΔE_{rot}, cm^{-1}	140	240	340	640
k_2^{int}, 10^{-10} cm^3 $molecule^{-1}$ s^{-1}	0.23±0.07	10.5±3.2	0.44±0.13	10.8±3.2
Z[a)]	~47	~1	~26	~1

a) The collision number Z is defined as a ratio of the total collision rate constant k_{TOT} to the energy transfer rate constant, k_2^{int}.

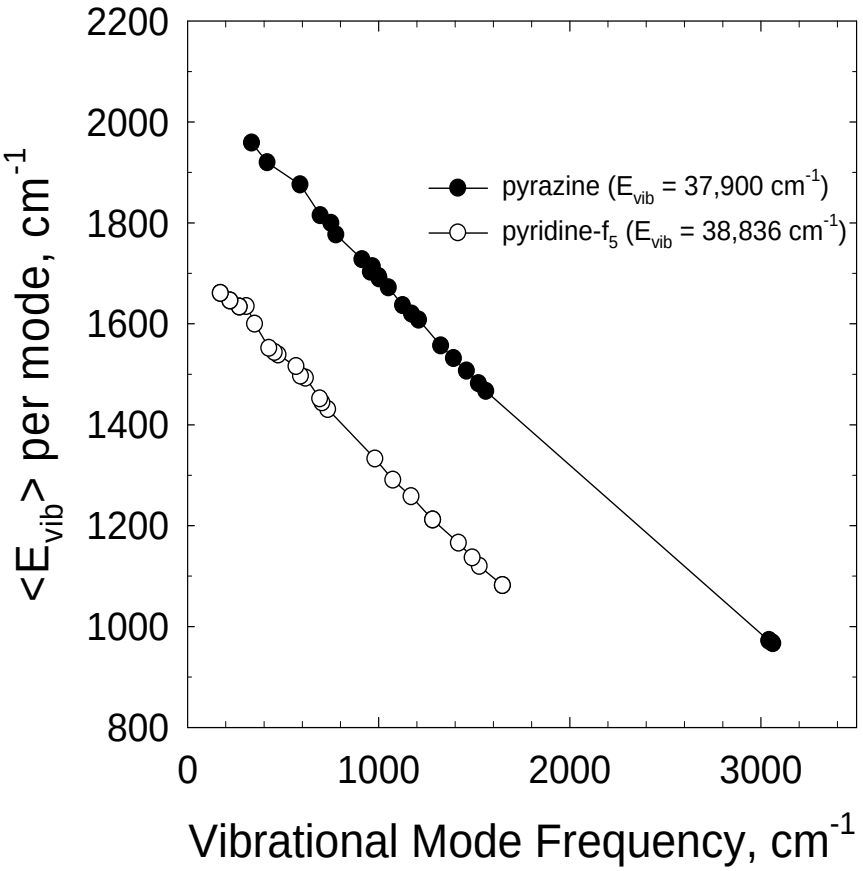

Figure 4.13. Average energy per vibrational mode in pyridine-f_5 (symbols) and pyrazine (open circle) after photo excitation using 266 nm UV light. Method of calculating the average energy per mode has been described in Section 3.3.6.

The energy transfer rate constant for appearance of the H_2O (010) state was determined from transient IR absorption measurements, as described in section 4.3.3. k_2^{int} for the H_2O (010) state is $k_2^{int}=(0.23\pm0.07)\times10^{-10}$ cm^3 $molecule^{-1}$ sec^{-1} for the V→V energy transfer channel. This is only 2% of the value for the V→RT channel. The collision rate of the V→V energy transfer channel for pyrazine/H_2O was measured to be ~5% of the total collision rate. The collision number Z is defined as a ratio of the total collision rate constant k_{TOT} to the energy transfer rate constant, k_2^{int}. The collision number Z for pyridine-f_5:H_2O are Z=47 for V→V pathway and Z=1 for V→RT pathway, meaning that essentially the V→V energy transfer takes place every 47 collisions while the V→RT energy transfer happens every collision. In term of pyrazine:H_2O, the V→V energy transfer takes place every 26 collisions. The higher probability of V→V pathway in pyrazine/H_2O also suggests the long range interaction mechanism.

4.4 Conclusion

The state-resolved energy gain profiles of scattered $H_2O(000)$ molecules with $E_{rot}>1000$ cm^{-1} are reported for quenching collisions with highly vibrationally excited pyridine-h_5, pyridine-d_5, and pyridine-f_5 (E~38,300 cm^{-1}). The results show that water molecules scattered from pyridine-h_5 and –d_5 have similar rotational distributions of T_{rot}=890 K. Collisions with pyridine-f_5 scatter water with less rotational energy and a rotational temperature of T_{rot}=530 K. The distributions of recoil velocities are similar for the three donor molecules and have center-of-mass translational temperatures of 400-700 K. The energy transfer rates are similar for the three donors and indicate that the V-RT pathway is the dominant relaxation route for

these donors with water. The results show that energy transfer into the bending vibrational mode of water is another pathway for collisional relaxation but only accounts for ~2% of all collisions.

Differences in the vibrational frequencies of the three donor molecules do not appear to explain the observed reduction in rotational energy of the scattered water molecules when pyridine-f_5 is the donor molecule. The experimental results are consistent with differences in state density of the highly excited donor molecules but the correlation of the energy transfer distribution with state density energy dependence is less than ideal and does not account for similarities in scattering data of the pyridine-h_5 and -d_5 donors. A third explanation is that motion between σ-and π-hydrogen bonding sites on the highly excited donors influences the extent to which water gains large amounts of rotational energy through a torque-inducing mechanism. This motion is likely to be similar for pyridine-h_5 and -d_5 based on the most stable π-configurations of aromatic species with hydrogen atoms. The strong electronegativity of fluorine atoms in pyridine-f_5 reverses water's orientation for the most stable π-configuration. This orientation is likely to hinder motion between the σ– and π–sites of the fluorinated donor and lead to a reduction in the rotational energy of the scattered water molecules. This torque-inducing mechanism is consistent with our experimental observations. The extent to which this type of motion occurs on pyridine-H_2O collisions can be investigated in the future using molecular dynamics simulations.

Chapter 5: Full Energy Transfer Dynamics in Collisions of Highly Vibrationally Excited Molecules and HOD: Probes of Strong and Weak collisions

5.1 Introduction

Water is a primary product of hydrocarbon combustion and is ubiquitous in the earth's atmosphere. In high temperature environments, quenching collisions deactivate highly excited molecules and compete directly with unimolecular decomposition and activated bimolecular reactions.[127-129] Despite the importance of collisional relaxation processes involving water, a number of outstanding questions remain about how water interacts with highly excited molecules. Average energy transfer measurements show that H_2O is a more efficient quencher of highly excited molecules than CO_2.[120-122,130-135] However, data on energy partitioning of strong collisions with large amounts of energy transferred show that H_2O is not particularly effective at removing energy from highly excited donors.[107,125,136] Previous experiments on collisional quenching of highly vibrationally excited molecules by H_2O show that less energy is transferred to H_2O molecules in impulsive collisions relative to CO_2.[23,24,77,82,107,117,118,125,136-140]

How can H_2O be a more efficient quencher than CO_2 given the fact that H_2O takes away less energy than CO_2 during impulsive collisions? The missing piece of information is the nature of the weak collisions. Weak collisions are of great interest

since they are the most common type of collisions but their study poses great challenges to the experimentalist. Despite the small amounts of energy that are transferred in weak collisions, their high probability contributes much to the overall quenching process. In this chapter, a novel method of measuring the weak collision dynamics using state-resolved transient IR probing will be described and the first state-resolved data on weak collisions of highly excited molecules are presented. These data yield the full distribution of energy transfer from a state-resolved prospective.

Several experimental methods have been used to study the energy transfer distribution function of highly excited molecules. Kinetically controlled selective ionization (KCSI) [15-17,141] directly monitors highly vibrationally excited donor molecules as they are relaxed by collisions. Distributions of highly vibrationally excited molecules with initial energy E are monitored as they pass through experimentally determined energy windows at an energy E'.[14,18-20] The molecular beam imaging technique measures the velocity mapping of scattered molecules, which corresponds to the energy mapping of scattered molecules, to measure the energy transfer distribution function.[11-13] Recently state-resolved IR absorption probing focuses on energy gain in the bath molecule and has been used to study dynamics of strong and weak collisional energy transfer. This approach is used to measure the full energy transfer distribution functions for a series of highly vibrationally excited molecules.[96,97] The details of measuring the weak collisions are described in this chapter.

Combining information of both the strong and weak collisions leads to a direct measurement of the molecular collision rate. The collision rate is of great importance in a number of fields including collisional energy transfer,[142-144] unimolecular reactions[29,145,146] and nucleation theory.[147-150] Common models used for molecular collisions include hard-sphere potentials and Lennard-Jones or Sutherland type potentials.[151] An number of experimental and theoretical studies have found that molecular collision rates are substantially larger than rates from these models.[143,152-158] Here high-resolution IR probing is used to directly measure collision rates.

In this chapter, investigations of weak collisions for highly vibrationally excited pyrazine, 2-methylpyridine (2-picoline) and 2.6-dimethylpyridine (2,6-lutidine) molecules with isotopically substituted water HOD are reported. A summary of the physical properties difference for the donors are shown in Table 5.1. When combined with previous strong collision data for these donors, the data provide a complete description of the energy transfer dynamics, the distribution function and the collision rate. Part of this project has been published in the Journal of Physical Chemistry A.[96,97]

5.2 Experimental Setup

A detailed description of the state-resolved transient IR absorption probing has been described in Chapter 2. Highly vibrationally excited pyrazine, 2-picoline and 2,6-lutidine with E_{vib}~38,300 cm^{-1} in their ground electronic state were prepared by photon excitation of the 4th harmonic output from a pulsed Nd:YAG laser with a wavelength of λ=266 nm.[159] The pulsed UV light was directed into the sample cell at a repetition of 2 Hz. The UV power was kept below 4.2 MW/cm^2 to achieve good

Table 5.1. Summary of physical properties for highly vibrationally excited donor molecules relevant in Chapter 5.

Donor molecule	Pyrazine	2-Picoline	2,6-Lutidine
Lennard-Jones diameter (Å)	5.35	5.58	5.89
Number of vibrational modes	24	36	45
Dipole moment (Debye)	0	1.85	1.71
Mass (g/mol)	80.09	93.13	107.16
Lennard-Jones collision rate (10^{-10} $cm^3 molecule^{-1} s^{-1}$)[a)]	6.19	6.44	6.86

[a)]The collision rate constants were determined using a Lennard-Jones potential as the intermolecular potential during the donor/HOD collisions. The method of getting the Lennard-Jones collision rate constants is described in Appendix B.

transient absorption signal relative to noise but still have single-photon absorption of donor molecules.

Time dependent transient IR absorption of HOD was collected using a tunable high resolution F-center laser operating at λ=2.7 μm. The IR light was collinear with the 266 nm beam in a 3 meter collision cell. The cell contained a flowing mixture of pyrazine, 2-picoline or 2,6-lutidine donor molecules and the H_2O/HOD/D_2O bath at a total pressure of ~25 mTorr. With the experimental conditions describe above, about 15% of donor molecules became vibrationally excited in the collision cell and the average collision time is τ_{col}~3 μs. Transient signal values at t=1 μs correspond to the outcome of single collisions between hot donors and HOD.

The HOD sample was prepared by mixing equal volumes of H_2O and D_2O. At equilibrium, the H_2O/HOD/D_2O sample had 49.4% HOD.[160] The pressure of donor and H_2O/HOD/D_2O mixture was 1:2 in the collision cell in order to match a 1:1 ratio for donor and HOD. HPLC grade H_2O and D_2O (Cambridge Isotope Laboratories, 99.9%) was purified by several freeze/pump/thaw cycles to eliminate the presence of atmosphere gases. Pyrazine (Aldrich, 99+ %), 2-picoline (Aldrich, 99+ %) and 2,6-lutidine (Aldrich, 99+ %) were also purified by several freeze/pump/thaw cycles before use.

The tunable F-center laser is a high resolution IR source with resolution $\Delta\nu$=0.0003 cm^{-1}. That enables individual rotational states of HOD to be probed. Scattered HOD (000) molecules were monitored using individual HOD (001←000) transitions. Time-dependent transient absorption signals were collected with the F-center laser locked onto a HOD transition line center. The transient absorption for

each J-state at t=1 μs following donor excitation was used to obtain the HOD rotational distribution having a characteristic rotational temperature, T_{rot}. Doppler-broadened line profiles give information about the translational energy released in the scattered molecules. Transient line profiles were measured by locking on a single F-center laser cavity mode and scanning an internal etalon in synchronized movement with a pair of rotating calcium fluoride plates. The rotating plates change the F-center laser cavity length and resulted in a 0.07 cm^{-1} scan across an individual ro-vibrational transition.

5.3 Results and Discussion

5.3.1 Nascent Transient Absorption of HOD (000)

HOD molecules at room temperature change their translational and rotational energies after collisions with vibrationally hot donor molecules (E_{vib}~38,300 cm^{-1}) as shown in Eq. 5.1.

$$\text{Donor } (E_{vib}) + \text{HOD (298 K)} \rightarrow \text{Donor } (E_{vib} - \Delta E) + \text{HOD } (000, J_{Ka,Kc}, V) \qquad \text{(Eq. 5.1)}$$

Here J is the total angular momentum, and K_a and K_c are the component along the molecular A axis and C axis, respectively. V is the component of the velocity along the IR beam corresponding to a 1-D projection of a 3-D velocity vector spread.

High-resolution IR absorption probes HOD (000, $J_{Ka,Kc}$, V) transitions and monitors the time-dependent population changes for individual J states as shown in Eq. 5.2.

$$\text{HOD}\ (000, J_{Ka,Kc}, V) + \text{IR} \rightarrow \text{HOD}\ (001, J'_{Ka',Kc'}, V) \qquad \text{(Eq. 5.2)}$$

HOD gains one quantum in its O-H stretch by absorption of IR radiation. The time-dependent fractional signal corresponds to the population change of the vibrationless $J_{Ka,Kc}$ state in the ground state of HOD (000, $J_{Ka,Kc}$, V). The transient signal value at t=1 μs is used to determine the population growth after single collisions between highly vibrationally excited donor molecules and HOD. The average collision time is τ_{col}~3 μs under the conditions used in this experiment.

Using high-resolution IR transient absorption to measure strong collisions is relatively straight forward using the approach described in Chapters 3 and 4. Probing the outcome of strong collisions involves monitoring bath molecules that are scattered into high rotational states that initially have no population. In this case, transient absorption signals correspond purely to the appearance of population in the state being probed. Measurements on weak collisions involving low-J states of bath molecules have added complications. Substantial thermal population means that transient signals of low-J states are dominated by depletion which can overwhelm appearance signals. If the line widths for appearance and depletion are equal, there is no way to distinguish the relative transient populations. In addition, competing energy transfer pathways can interfere with pathway-specific measurements since

transient absorption measurements give information about the population difference between states, collisions that put energy into the upper state of the probe transition can obscure measurements of the lower state population. Additional measurements must address this issue.

Consider the transient absorption of the HOD (000, $2_{2,0}$) state as an example. The IR probe transition for this state is HOD (001, $2_{2,1}$) ← HOD (000, $2_{2,0}$). The population change for the (000, $2_{2,0}$) state can result from two processes. HOD can be scattered into the (000, $2_{2,0}$) state as in Eq. 5.3 and HOD can be depleted out of the (000, $2_{2,0}$) state due to Eq. 5.4.

$$\text{Donor } (E_{vib}) + \text{HOD (any state)} \xrightarrow{k^J_{app}} \text{Donor } (E - \Delta E_{vib}) + \text{HOD } (000, 2_{2,0}) \qquad \text{(Eq. 5.3)}$$

$$\text{Donor } (E_{vib}) + \text{HOD } (000, 2_{2,0}) \xrightarrow{k^J_{dep}} \text{Donor } (E_{vib} - \Delta E) + \text{HOD (any state)} \qquad \text{(Eq. 5.4)}$$

It is also possible that collisions can directly populate the upper state of the probe transition, as shown in Eq. 5.5.

$$\text{Donor (E)} + \text{HOD (298 K)} \longrightarrow \text{Donor } (E_{vib} - \Delta E) + \text{HOD } (001, 2_{2,1}) \qquad \text{(Eq. 5.5)}$$

The collision-induced appearance of HOD (001, J_{KaKc}) state was investigated separately using HOD (002←001) probe transitions, but no transient absorption

signals were observed. It is not surprising that collisions leading to energy gain in the (001) state are not observed. It is likely that vibration-to-vibration (V→V) energy transfer is dominated by a one-quantum transfer. The highest frequency vibrational modes of 2-picoline and 2,6-lutidine are near 3000 cm^{-1} while the HOD ν_3 stretch is near 3710 cm^{-1}. Thus Eq. 5.5 does not impact the HOD (001←000) probe transitions in this study. Transient signals for HOD result purely from the collisions such as shown in Eq. 5.3 and Eq. 5.4. For this reason, the HOD (001←000) transition can be used to characterize the energy partitioning in weak collisions of highly vibrationally excited donor molecules with HOD.

Transient signals for HOD in the (000, $7_{0,7}$) state following collisions with highly vibrationally excited 2-picoline and 2,6-lutidine molecules are shown in Figure 5.1 and Figure 5.2. The energy of the HOD (000, $7_{0,7}$) state is E_{rot}=109 cm^{-1} and has appreciable thermal population at 298 K. When the IR probe is tuned to ν_0, the center of the IR transition, the rate of population loss of HOD in the $7_{0,7}$ state is greater than that of appearance following the pulsed UV absorption of donor molecules. Hence, Figure 5.1(a) and Figure 5.2(a) show net depletion of population for this state. When the IR probe is tuned to the wings of the absorption feature, transient absorption traces in Figure 5.1(b) and Figure 5.2(b) show the appearance of HOD population in the (000, $7_{0,7}$) state due to collisions with the hot donors. In Section 5.3.2, the analysis for extrapolating appearance information for the low J states from the relatively large depletion signals is described.

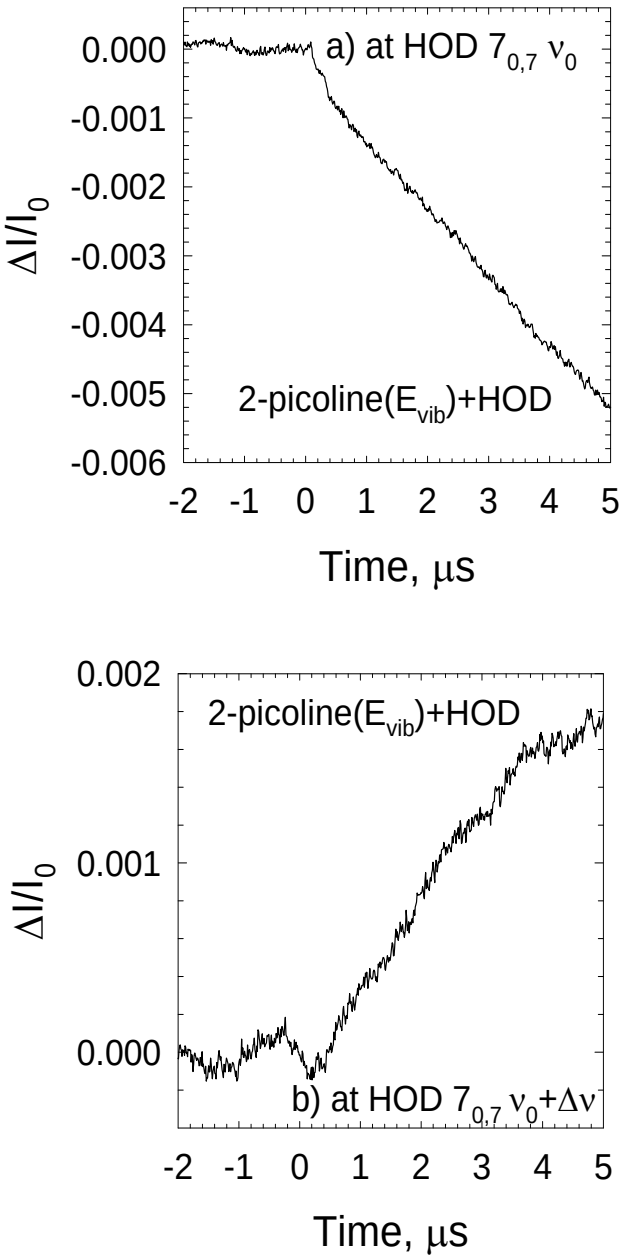

Figure 5.1. Fractional IR absorption of HOD (000) following collisions of highly excited 2-picoline with HOD measured at ν_0 as a function of time following UV excitation. Figure 5.1a shows depletion of HOD (000, $7_{0,7}$) with E_{rot}=403 cm^{-1} and Figure 5.1b shows appearance for the same transition.

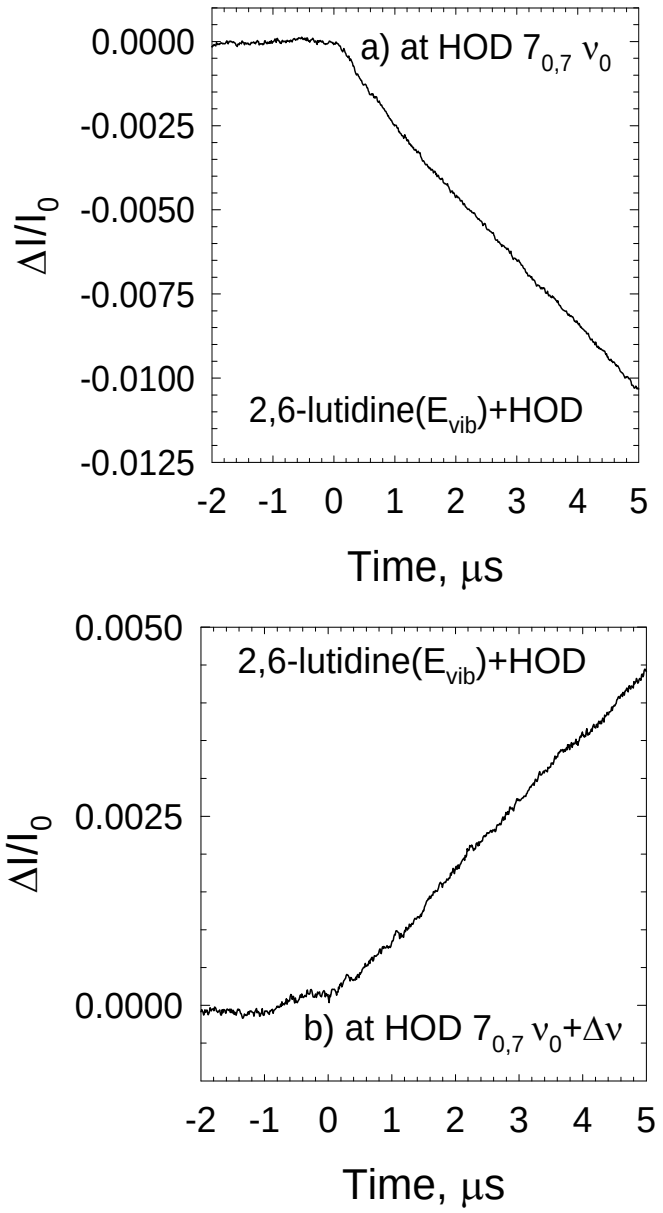

Figure 5.2. Fractional IR absorption of HOD (000) following collisions of highly excited 2,6-lutidine with HOD measured at ν_0 as a function of time following UV excitation. Figure 5.2a shows depletion of HOD (000, $7_{0,7}$) with E_{rot}=403 cm^{-1} and Figure 5.2b shows appearance for the same transition.

5.3.2 Translational Energy Gain of HOD

The translational energy gain of HOD (000) was measured by two different methods for the strong and weak collisions. For strong collisions, translational energy gain measurements of HOD were achieved by measuring the Doppler-broadened linewidths in individual high-J states of HOD. These states have rotational energy above 1000 cm^{-1} and are not populated at room temperature. The measurement of transient line profiles was performed by collecting time-dependent fractional absorption changes as a function of probe laser frequency following collisions of HOD with highly vibrationally excited pyrazine, 2-picoline and 2,6-lutidine. The line profiles at 1 μs are fit with single Gaussian functions. The full width at half max (FWHM) linewidths were determined from the fit. Translational temperatures of the scattered molecules were determined from FWHM linewidth. This method has been explained in detail in Chapter 3 and Chapter 4.

For weak collisions, measuring appearance profiles of HOD (000) is more involved. Since the low-J states are populated at room temperature, the Doppler-broadened line profile is a combination of both absorption and depletion phenomena. Figure 5.3 shows the t=1 μs transient line profile for HOD in the (000, $7_{0,7}$) state scattered from highly vibrationally excited 2,6-lutidine. The signal at line center is a strong depletion signal corresponding to population loss of the initial thermal population. There is a second component observed in the wings of the lineprofile at approximately $\Delta\nu$=0.0125 cm^{-1} from line center. The absorbing component, corresponding to molecules scattering into the (000, $7_{0,7}$) state, is of interest because it is a measure of the population and velocity distribution that results from a subset of

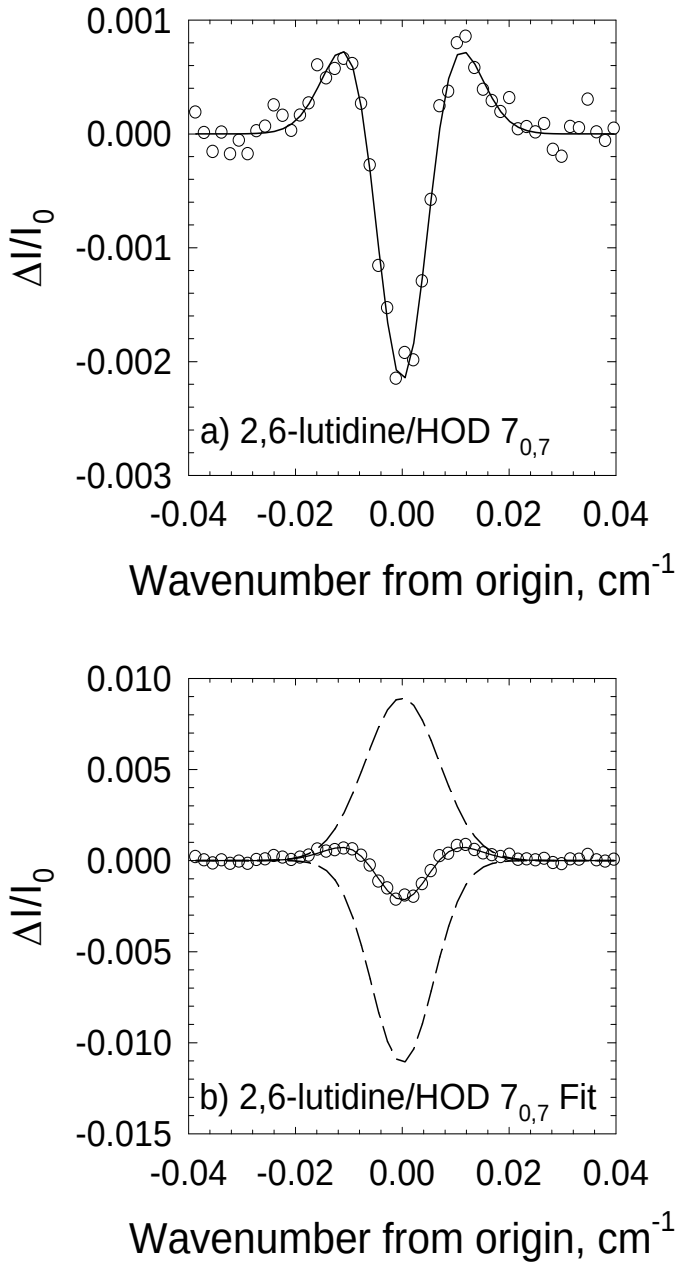

Figure 5.3. Transient absorption line profile for HOD (000, $7_{0,7}$) collected at 1 μs following UV excitation of 2,6-lutidine. The raw data and fit are shown in Figure 5.3a while the double Gaussian fit alone is shown in Figure 5.3b. The fit has been separated into its absorption (dashed line/positive going) and depletion (dashed line/negative going) components for clarity.

weak collisions. Doppler-broadened line profiles of this type are fit using a nonlinear least squares analysis to a double Gaussian function:

$$F(\nu) = I_{app}\exp\left(-4\ln 2\left(\frac{\nu-\nu_0}{\Delta\nu_{app}}\right)^2\right) - I_{dep}\exp\left(-4\ln 2\left(\frac{\nu-\nu_0}{\Delta\nu_{dep}}\right)^2\right) + F_0 \qquad \text{(Eq. 5.6)}$$

The parameters I_{app} and I_{dep} are the absorption and depletion intensities at ν_0 and $\Delta\nu_{app}$ and $\Delta\nu_{dep}$ are the full width at half maximum (FWHM) linewidths for the absorption and depletion, respectively.

Appearance linewidths were obtained for a number of HOD (000) states following collision with pyrazine, 2-picoline and 2,6-lutidine. The results are summarized in Tables 5.2, 5.3, 5.4 and plotted in Figure 5.4. The data shown are an average of three measurements and the reported uncertainty is determined by measuring multiple room temperature linewidths of a CO_2 ($10^01 \leftarrow 00^00$) transition which agreed with the known value to within 0.0005 cm^{-1}. Tables 5.2, 5.3 and 5.4 show that the average $\Delta\nu_{app}$ for HOD (000) after single collisions with pyrazine, 2-picoline and 2,6-lutidine/HOD were found to be $\Delta\nu_{app}$=0.0148±0.001, 0.0154±0.001 and 0.0147±0.001 cm^{-1}, respectively. These values correspond to average lab frame translational temperatures of T_{trans}(lab)=570±90, 610±110 and 580±110 K and average relative translational energy gains of $\langle\Delta E_{rel}\rangle$=351±49, 397±71 and 340± 63 cm^{-1}. HOD is scattered with relatively small amounts of translational energy. In addition, no distinct difference in translational energy gain is observed for collisions with pyrazine, 2-picoline, and 2,6-lutidine.

Table 5.2. Translational energy gain in HOD (000, $J_{Ka,Kc}$) low and high J states following collisions with highly vibrationally excited pyrazine (E_{vib}=37,920 cm^{-1}).

$J_{Ka,Kc}$	ν_0 (cm^{-1})	E_{rot} (cm^{-1})	$\Delta\nu_{app}$ (cm^{-1})[a]	T_{trans}(lab)[b] (K)	T_{rel}[c] (K)	$\langle\Delta E_{rel}\rangle$[d] ($cm^{-1}$)
$2_{2,0}$	3702.904	109.269	0.0136	500±75	548±82	261±39
$4_{1,3}$	3787.510	182.983	0.0146	550±83	610±92	325±49
$6_{1,6}$	3798.189	308.615	0.0150	578±87	645±97	362±54
$7_{0,7}$	3810.595	403.161	0.0139	493±74	539±81	251±38
$7_{1,6}$	3826.241	473.918	0.0141	503±75	552±83	265±40
$10_{3,7}$	3664.909	1024.568	0.0159	697±105	792±119	515±65
$11_{3,8}$	3739.334	1164.509	0.0151	604±91	677±102	395±52
$12_{1,11}$	3876.128	1220.027	0.0157	608±91	682±102	400±51
$12_{2,10}$	3893.025	1331.216	0.0156	595±89	666±100	384±49

[a] $\Delta\nu_{app}$ is the full width at half maximum (FHWM) linewidth for a specific $J_{Ka,Kc}$. Each value is an average of typically three values and has an uncertainty of 0.0007 cm^{-1}.

[b] Lab frame translational temperature for HOD (000, $J_{Ka,Kc}$). This is calculated from the following expression: $T_{trans,lab} = (mc^2/8Rln(2))(\Delta\nu_{app}/\nu_o)^2$. The uncertainty is determined from both measurement uncertainty in the linewidth and propagated error in the double Gaussian fit.

[c] Center-of-mass frame translational temperature for HOD (000, $J_{Ka,Kc}$). This is calculated from the expression: $T_{rel} = T_{trans}(lab) + (T_{trans}(lab) - 298)(m_{HOD}/m_{Donor})$

[d] Average translational energy change for HOD (000, $J_{Ka,Kc}$). This is obtained from $\langle\Delta E_{rel}\rangle = \frac{3}{2}k_B(T_{rel} - T_0)$, where T_0=298 K.

Table 5.3. Translational energy gain in HOD (000, $J_{Ka,Kc}$) low and high J states following collisions with highly vibrationally excited 2-picoline (E_{vib}=38,313 cm^{-1}).

$J_{Ka,Kc}$	ν_0 (cm^{-1})	E_{rot} (cm^{-1})	$\Delta\nu_{app}$ (cm^{-1})[a]	T_{trans}(lab)[b] (K)	T_{rel}[c] (K)	$\langle\Delta E_{rel}\rangle$[d] ($cm^{-1}$)
$2_{2,0}$	3702.904	109.269	0.0137	500±75	541±81	254±38
$4_{1,3}$	3787.510	182.983	0.0161	670±100	746±111	467±70
$6_{1,6}$	3798.189	308.615	0.0139	500±90	541±97	254±46
$7_{0,7}$	3810.595	403.161	0.0163	685±145	764±162	486±103
$7_{1,6}$	3826.241	473.918	0.0153	595±140	656±154	373±88
$11_{1,10}$	3866.368	1046.474	0.0172	733±110	822±132	546±82

Footnote a), b), c) and d) are the same as Table 5.2

Table 5.4. Translational energy gain in HOD (000, $J_{Ka,Kc}$) low and high J states following collisions with highly vibrationally excited 2,6-lutidine (E_{vib}=38,702 cm^{-1}).

$J_{Ka,Kc}$	ν_0 (cm^{-1})	E_{rot} (cm^{-1})	$\Delta\nu_{app}$ (cm^{-1}) [a]	T_{trans}(lab) [b] (K)	T_{rel} [c] (K)	$\langle\Delta E_{rel}\rangle$ [d] (cm^{-1})
$2_{2,0}$	3702.904	109.269	0.0138	514±80	552±86	265±41
$4_{1,3}$	3787.510	182.983	0.0136	477±105	509±112	220±48
$6_{1,6}$	3798.189	308.615	0.0138	610±125	665±136	383±78
$7_{0,7}$	3810.595	403.161	0.0133	559±140	605±152	320±80
$7_{1,6}$	3826.241	473.918	0.0149	484±105	517±112	228±50
$11_{1,10}$	3866.368	1046.474	0.0165	677±100	744±112	465±70
$12_{1,11}$	3876.128	1220.027	0.0169	707±106	780±117	502±75

Footnote a), b), c) and d) are the same as Table 5.2

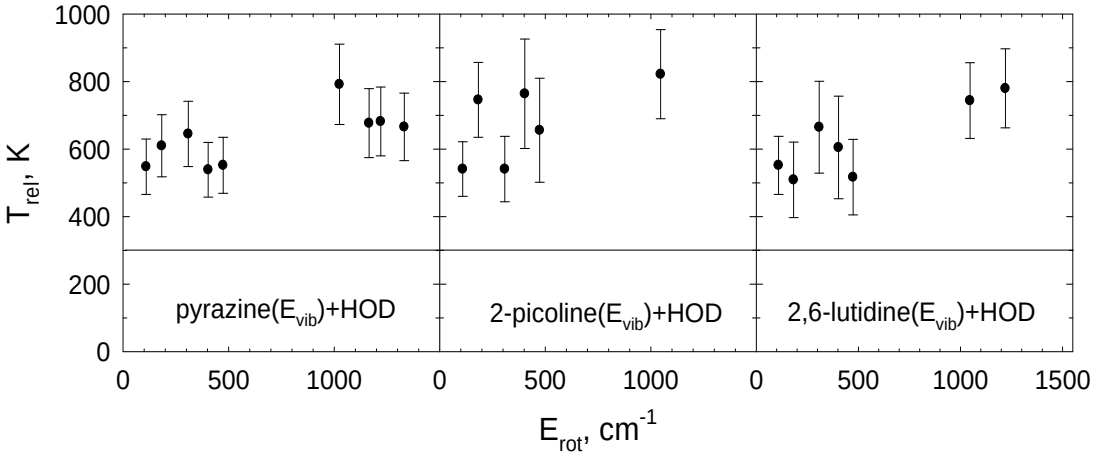

Figure 5.4. Center-of-mass translational temperatures (T_{rel}) vs. HOD (000) E_{rot} following collisions with pyrazine, 2-picoline and 2,6-lutidine. T_{rel} does not have a strong dependence on E_{rot} from 0 cm^{-1} to 1500 cm^{-1}.

Translational temperatures of the depletion components are within error of 298 K for the measurements described in the present work. Values are listed in Table 5.5. For collisions between 2,6-lutidine and HOD the average lab frame depletion temperature was found to be T_{dep}=376±71 K. Similarly, 2-picoline/HOD showed T_{dep}=368±81 K and depletion linewidth for pyrazine/ HOD collision have T_{dep}=315-350 K. It is possible that the initial distribution is centered slightly higher than room temperature suggesting that the V→RT energy transfer process is more likely for collisions of HOD molecules with higher velocity. However, that is difficult to say with any certainty given the error bars of the measurement.

5.3.3 Rotational Energy Gain of HOD

Rotational distributions for scattered HOD molecules following collisions with highly vibrationally excited pyrazine, 2-picoline and 2,6-lutidine are described in this section. Population changes for individual $J_{Ka,Kc}$ states of HOD at t=1 μs were fit with a Boltzmann distribution, as shown in Figure 5.5. The nascent rotational temperature of HOD after single collisions with highly vibrationally excited pyrazine is T_{rot}=430±50 K. For collisions of HOD with 2-picoline, T_{rot}=426±60 K. For collisions with 2,6-lutidine, T_{rot}=394±64 K. These values correspond to a rotational energy gain in HOD $\langle \Delta E_{rot} \rangle$=138±52, 133±63 and 100±67 cm^{-1}. $\langle \Delta E_{rot} \rangle$ is the average change in rotational energy based on $\left\langle \Delta E_{rot} \right\rangle = \frac{3}{2} k_B \left(T_{rot} - T_0 \right)$, in which T_0=298 K. The data show that only minor amounts of rotational energy are found in the scattered HOD molecules. The $\langle \Delta E_{rot} \rangle$ values for all three donor/HOD collision pairs are similar.

Table 5.5. Translational energy of depletion in HOD (000, $J_{Ka,Kc}$) low J states following collisions with highly vibrationally excited pyrazine (E_{vib}=37,900 cm^{-1}), 2-picoline (E_{vib}=38,313 cm^{-1}) and 2,6-lutidine (E_{vib}=38,702 cm^{-1}).

Donor Molecules	$J_{Ka,Kc}$	$\Delta\nu_{dep}$ (cm^{-1}) [a]	T_{dep} [b] (K)
pyrazine	$2_{2,0}$	0.0108	315±41
	$4_{1,3}$	0.0113	330±41
	$6_{1,6}$	0.0113	328±41
	$7_{0,7}$	0.0117	349±42
	$7_{1,6}$	0.0112	317±40
2-picoline	$2_{2,0}$	0.0114	353±43
	$4_{1,3}$	0.0125	405±45
	$6_{1,6}$	0.0108	301±39
	$7_{0,7}$	0.0125	401±45
	$7_{1,6}$	0.0122	379±43
2,6-lutidine	$2_{2,0}$	0.0118	374±44
	$4_{1,3}$	0.0119	368±43
	$6_{1,6}$	0.0126	433±48
	$7_{0,7}$	0.0122	382±44
	$7_{1,6}$	0.0113	322±40

[a] $\Delta\nu_{dep}$ is FWHM Doppler-broadened line width for population depletion from HOD states with E_{rot}=100-500 cm^{-1}.

[b] Lab-frame translational temperatures T_{dep} for depletion of initial HOD (000, $J_{Ka,Kc}$) are determined similarly to T_{trans}(lab) in footnote b in Table 5.2 using $\Delta\nu_{dep}$.

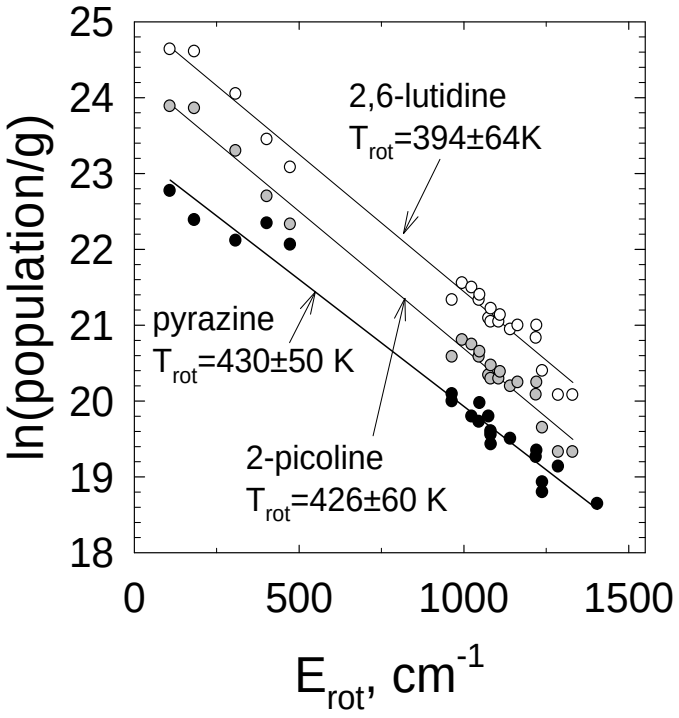

Figure 5.5. The nascent distributions of HOD (000) rotational states for collisions with highly vibrationally excited pyrazine (black circles), 2-picoline (grey crcles) and 2,6-lutidine (open circles).

Nascent rotational distributions of scattered HOD (000) molecules after single collisions with highly vibrationally excited donor are very similar all being within error of 400 K. This is in contrast with the strong collisional energy transfer results for the same donor molecules with H_2O. Specifically, the outcome of pyrazine/H_2O collisions has a nascent rotational temperature for HOD of T_{rot}=920±100 K.[136] Collisions between highly vibrationally excited 2-picoline and 2,6-lutidine and H_2O are described by rotational temperatures of T_{rot}=590±90 K and 490±80 K.[21,22] The low rotational temperature for scattered HOD molecules indicates a marked preference for weak collisions versus strong collisions relative to H_2O. The reduced rotational energy of HOD may be due to stronger interactions with the donor molecules, possibly through the nitrogen lone pair.[96,97]

5.3.4 Energy Transfer Rates from HOD (000) Appearance Measurements

State-specific bimolecular energy transfer rate constants k_{app}^{J} for Eq. 5.3 were determined using the method described in Appendix C. Values of k_{app}^{J} are listed in Tables 5.6, 5.7 and 5.8 based on transient measurements for the donor/HOD pairs. Rates for other states were extrapolated by the experimentally measured rotational distribution. These are shown in Figure 5.6. For E_{rot}<1000 cm^{-1} the difference in k_{app}^{J} for the different donors is apparent, but for E_{rot}>1000 cm^{-1} the state-specific energy transfer rate constants are almost the same for the three donor/HOD pairs. The integrated energy transfer rate constant k_{app} is determined by summing the k_{app}^{J} values for all HOD (000) rotational states. The integrated energy transfer rate constant for appearance for pyrazine/HOD is $k_{app}=(1.0\pm0.3) \times 10^{-9}$ cm^3 $molecule^{-1}$ s^{-1}.

Table 5.6. Appearance rates of HOD (000, $J_{Ka,Kc}$) due to collisions with pyrazine (E_{vib}=37,920 cm^{-1}).

Pyrazine (E_{vib}) + HOD $\xrightarrow{k^J_{app}}$ Pyrazine (E_{vib}-ΔE) + HOD (000, $J_{Ka,Kc}$).

J_{KaKc}	ν_0, cm^{-1}	E_{rot}, cm^{-1}	k^J_{app}, 10^{-12} cm^3 $molecule^{-1}$ s^{-1}
$2_{2,0}$	3702.904	109.269	13.8±4.1
$4_{1,3}$	3787.510	182.984	19.6±5.9
$6_{1,6}$	3798.189	308.616	18.8±5.6
$7_{0,7}$	3810.595	403.162	15.9±4.8
$7_{1,6}$	3826.241	473.918	12.6±3.6
$10_{2,8}$	3757.296	964.851	3.6±1.1
$10_{3,7}$	3879.275	1024.569	2.9±0.9
$11_{1,10}$	3866.368	1046.474	3.0±0.9
$11_{2,10}$	3864.729	1049.125	3.0±0.9
$12_{1,12}$	3864.216	1075.763	2.9±0.9
$9_{5,5}$	3835.743	1082.785	2.2±0.6
$9_{5,6}$	3836.070	1082.887	2.2±0.6
$11_{2,9}$	3884.079	1141.692	2.2±0.6
$12_{1,11}$	3876.128	1220.029	1.9±0.6
$12_{2,11}$	3875.159	1221.537	1.9±0.6
$10_{5,6}$	3850.937	1238.795	1.4±0.4
$10_{5,5}$	3851.730	1239.089	1.4±0.4
$11_{4,7}$	3884.345	1287.239	1.4±0.4
$13_{1,12}$	3885.844	1405.818	1.1±0.3

$k_{app} = (1.02 \pm 0.30) \times 10^{-9}$ cm^3 $molecule^{-1}$ s^{-1}

Table 5.7. Appearance rates of HOD (000, $J_{Ka,Kc}$) due to collisions with 2-picoline (E_{vib}=38,313 cm^{-1}).

2-Picoline (E_{vib}) + HOD $\xrightarrow{k^J_{app}}$ Picoline (E_{vib}-ΔE) + HOD (000, $J_{Ka,Kc}$)

J_{KaKc}	ν_0, cm^{-1}	E_{rot}, cm^{-1}	k^J_{app}, 10^{-12} cm^3 $molecule^{-1}$ s^{-1}
$2_{2,0}$	3702.904	109.269	20.9±6.3
$4_{1,3}$	3787.510	182.984	29.7±8.9
$6_{1,6}$	3798.189	308.616	28.5±8.6
$7_{0,7}$	3810.595	403.162	24.2±7.3
$7_{1,6}$	3826.241	473.918	19.2±5.8
$10_{2,8}$	3757.296	964.851	5.5±1.7
$10_{3,8}$	3860.956	995.793	5.0±1.5
$10_{3,7}$	3879.275	1024.569	4.5±1.4
$11_{1,10}$	3866.368	1046.474	4.6±1.4
$11_{2,10}$	3864.729	1049.125	4.6±1.4
$12_{1,12}$	3864.216	1075.763	4.6±1.4
$9_{5,5}$	3835.743	1082.785	3.4±1.0
$9_{5,4}$	3836.070	1082.887	3.4±1.0
$10_{4,7}$	3859.538	1106.264	3.5±1.1
$10_{4,6}$	3866.258	1110.760	3.4±1.0
$11_{2,9}$	3884.079	1141.692	3.4±1.0
$11_{3,9}$	3873.111	1164.509	3.1±0.9
$12_{1,11}$	3876.128	1220.029	2.9±0.9
$12_{2,11}$	3875.159	1221.537	2.8±0.8
$10_{5,6}$	3850.937	1238.795	2.2±0.7
$11_{4,7}$	3884.345	1287.239	2.1±0.6
$12_{2,10}$	3893.025	1331.216	2.0±0.6
$k_{app}=(1.6\pm0.48)\times10^{-9}$ cm^3 $molecule^{-1}$ s^{-1}			

Table 5.8. Appearance rates of HOD (000, $J_{Ka,Kc}$) due to collisions with 2,6-lutidine (E_{vib}=38,702 cm^{-1}).

$$\text{2,6-Lutidine } (E_{vib}) + \text{HOD} \xrightarrow{k^J_{app}} \text{Lutidine } (E_{vib}-\Delta E) + \text{HOD } (000, J_{Ka,Kc})$$

J_{KaKc}	ν_0, cm^{-1}	E_{rot}, cm^{-1}	k^J_{app}, 10^{-12} cm^3 $molecule^{-1}$ s^{-1}
$2_{2,0}$	3702.904	109.269	32.9±9.9
$4_{1,3}$	3787.510	182.984	45.3±13.6
$6_{1,6}$	3798.189	308.616	41.5±12.5
$7_{0,7}$	3810.595	403.162	34.0±10.2
$7_{1,6}$	3826.241	473.918	26.3±7.9
$10_{2,8}$	3757.296	964.851	6.2±1.9
$10_{3,8}$	3860.956	995.793	5.6±1.7
$10_{3,7}$	3879.275	1024.569	5.0±1.5
$11_{1,10}$	3866.368	1046.474	5.1±1.5
$11_{2,10}$	3864.729	1049.125	5.0±1.5
$12_{1,12}$	3864.216	1075.763	5.0±1.5
$9_{5,5}$	3835.743	1082.785	3.7±1.1
$9_{5,4}$	3836.070	1082.887	3.7±1.1
$10_{4,7}$	3859.538	1106.264	3.7±1.1
$10_{4,6}$	3866.258	1110.760	3.7±1.1
$11_{2,9}$	3884.079	1141.692	3.6±1.1
$11_{3,9}$	3873.111	1164.509	3.3±1.0
$12_{1,11}$	3876.128	1220.029	3.0±0.9
$12_{2,11}$	3875.159	1221.537	2.9±0.9
$10_{5,6}$	3850.937	1238.795	2.3±0.7
$11_{4,7}$	3884.345	1287.239	2.1±0.6
$12_{2,10}$	3893.025	1331.216	2.0±0.6
$k_{app}=(2.2\pm0.66) \times 10^{-9}$ cm^3 $molecule^{-1}$ s^{-1}			

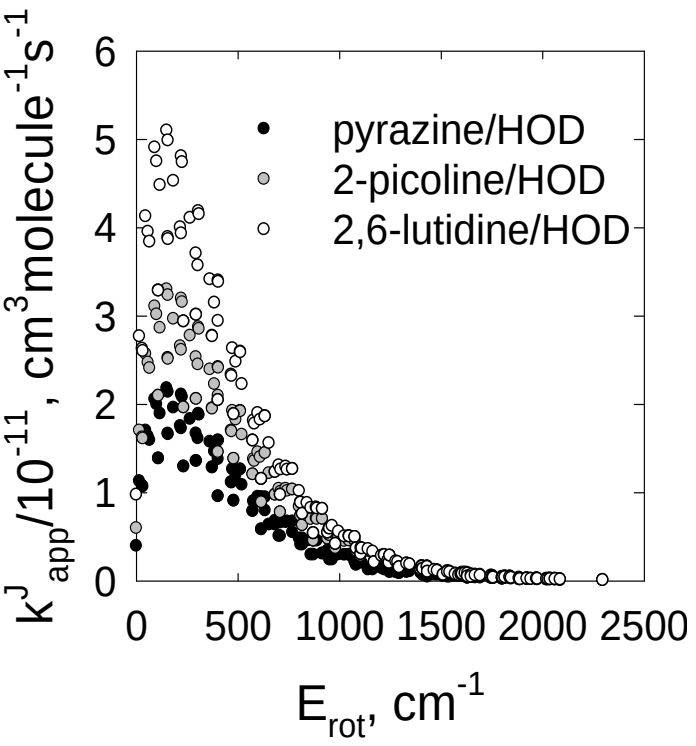

Figure 5.6. Rate constants k^J_{app} for appearance of HOD (000) following collisions with highly vibrationally excited pyrazine, 2-picoline and 2,6-lutidine. Values of k^J_{app} for HOD include a nuclear spin degeneracy of g_{ns}=6 and a rotational degeneracy of g_{rot}=2J+1 and are based on the rate constants in Tables 5.6, 5.7 and 5.8.

For 2-picoline/HOD k_{app} is $k_{app}=(1.6\pm0.5) \times 10^{-9}$ cm^3 molecule^{-1} s^{-1} and $k_{app}=(2.2\pm0.7) \times 10^{-9}$ cm^3 molecule^{-1} s^{-1} for 2,6-lutidine/HOD.

The energy transfer pathway of donor vibration to bath rotation and translation (V→RT) is the primary channel of collisional quenching for aromatic species with HOD. Collisions that induce donor vibration to bath vibration (V→V) energy transfer occur more rarely. Signals for appearance of HOD (010) are below the detection limit of our experiments. In the case of pyrazine/H_2O, collisions that produce H_2O (010) account for only ~5% of total collision rate.[125] Also, no reactive pathways have been detected that would yield HOD from a mixture of vibrationally hot donor and D_2O. For the HOD studies presented here, the integrated energy transfer rate based purely on V→RT channel represents a lower limit of collision rate.

5.3.5 Collision Rates from HOD Depletion Measurements

State-resolved population depletion measurements are also a measure of the collision rate. Collisions between highly vibrationally excited donor molecules and HOD move population out of low-J states which are populated at room temperature, such as shown in Eq. 5.4. The rate for depletion is given in Eq. 5.7, based on the idea that elastic and inelastic collisions change the velocity and/or rotational quantum state of HOD.

$$\text{Rate}_{dep}(J) = -\frac{d[HOD^J]}{dt} = k_{dep}[HOD^J]_0[Donor^E]_0 \qquad \text{(Eq. 5.7)}$$

Here $[HOD^J]_0$ is the concentration of HOD at the initial J state. $[Donor^E]_0$ is the initial concentration of highly vibrationally excited donor molecules determined from observed UV absorption. Depletion results solely from collisions, so the depletion rate is essentially the collision rate. We assume that collision rate constant does not depend on J. The depletion rate constant k_{dep} was measured for a number of HOD states. Tables 5.9, 5.10 and 5.11 list the depletion rates measured for a number of HOD states based on Eq. 5.7. The average depletion rate constants for pyrazine, 2-picoline/HOD and 2,6-lutidine/HOD are $\langle k_{dep} \rangle = (1.1 \pm 0.3) \times 10^{-9}$, $(2.3 \pm 0.7) \times 10^{-9}$ and $2.3 \pm 0.7 \times 10^{-9}$ cm^3 molecule^{-1} s^{-1}. The integrated energy transfer rate constant for V→RT energy transfer from appearance measurements are $k_{app} = (1.0 \pm 0.3) \times 10^{-9}$ cm^3 molecule^{-1} s^{-1} for pyrazine/HOD, $k_{app} = (1.6 \pm 0.5) \times 10^{-9}$ cm^3 molecule^{-1} s^{-1} for 2-picoline/HOD and $k_{app} = (2.2 \pm 0.7) \times 10^{-9}$ cm^3 molecule^{-1} s^{-1} for 2,6-lutidine/HOD. It is interesting that $k_{app} \leq k_{dep}$ for the three donor/HOD pairs studied here. This result shows that V→RT energy transfer dominates the relaxation and that V→V energy transfer is a relatively minor pathway.

5.3.6 Comparison of Collision Rates from Experiment to Lennard-Jones Collision Rates

In this section, the observed collision rates are compared with Lennard-Jones collision rates. Lennard-Jones collision rates are based on a two parameter (σ and ε) description of molecular interactions and are widely used as a reference in chemical kinetics. The Lennard-Jones collision rates for the three donor/HOD pairs are listed in Table 5.1 and have values of $k_{LJ} \sim 6.5 \times 10^{-10}$ cm^3 molecule^{-1} s^{-1} at 298 K. It is interesting but perhaps not surprising that the appearance and depletion rates reported

Table 5.9. Depletion rates of HOD (000, $J_{Ka,Kc}$) due to collisions with pyrazine (E_{vib}=37,900 cm^{-1}).

$$\text{Pyrazine } (E_{vib}) + \text{HOD } (000, J_{Ka,Kc}) \xrightarrow{k_{dep}} \text{Pyrazine } (E_{vib}-\Delta E) + \text{HOD (other states)}$$

J_{KaKc}	ν_0, cm^{-1}	E_{rot}, cm^{-1}	k_{dep}, 10^{-9} cm^3 $molecule^{-1}$ s^{-1}
$2_{2,0}$	3702.904	109.269	1.2±0.4
$4_{1,3}$	3787.510	182.984	0.9±0.3
$6_{1,6}$	3798.189	308.616	1.0±0.3
$7_{0,7}$	3810.595	403.162	1.2±0.4
$7_{1,6}$	3826.241	473.918	1.1±0.3
$\langle k_{dep} \rangle = (1.1 \pm 0.3) \times 10^{-9}$ cm^3 $molecule^{-1}$ s^{-1}			

Table 5.10. Depletion rates of HOD (000, $J_{Ka,Kc}$) due to collisions with 2-picoline (E_{vib}=38,313 cm^{-1}).

2-Picoline (E_{vib}) + HOD (000, $J_{Ka,Kc}$)

$\xrightarrow{k_{dep}}$ Picoline (E_{vib}-ΔE) + HOD (other states)

J_{KaKc}	ν_0, cm^{-1}	E_{rot}, cm^{-1}	k_{dep}, 10^{-9} cm^3 $molecule^{-1}$ s^{-1}
$2_{2,0}$	3702.904	109.269	2.3±0.7
$4_{1,3}$	3787.510	182.984	2.6±0.8
$6_{1,6}$	3798.189	308.616	1.9±0.6
$7_{0,7}$	3810.595	403.162	2.1±0.6
$7_{1,6}$	3826.241	473.918	2.4±0.7
$\langle k_{dep} \rangle = (2.3 \pm 0.7) \times 10^{-9}$ cm^3 $molecule^{-1}$ s^{-1}			

Table 5.11. Depletion rates of HOD (000, $J_{Ka,Kc}$) due to collisions with 2,6-lutidine (E_{vib}=38,702 cm^{-1}).

2,6-Lutidine (E_{vib}) + HOD (000, $J_{Ka,Kc}$)

$\xrightarrow{k_{dep}}$ Lutidine (E_{vib}-ΔE) + HOD (other states)

J_{KaKc}	ν_0, cm^{-1}	E_{rot}, cm^{-1}	k_{dep}, 10^{-9} cm^3 $molecule^{-1}$ s^{-1}
$2_{2,0}$	3702.904	109.269	2.4±0.7
$4_{1,3}$	3787.510	182.984	2.9±0.9
$6_{1,6}$	3798.189	308.616	2.7±0.8
$7_{0,7}$	3810.595	403.162	2.1±0.6
$7_{1,6}$	3826.241	473.918	1.7±0.5
$\langle k_{dep} \rangle = (2.3 \pm 0.7) \times 10^{-9}$ cm^3 $molecule^{-1}$ s^{-1}			

here for donor/HOD collisions are all larger than the Lennard-Jones collision rate. The empirical parameters σ and ε are generally determined from pure species and then combined using accepted rules to characterize collisions of mixed species. This approach inherently overlooks effects of hydrogen bonding interactions that are present in collisions of HOD with nitrogen-containing aromatic species.

The appearance and depletion rates reported here both provide a measure of the collision rate for donor/HOD collisions. The appearance rates account for the primary collision pathway of V→RT energy transfer and result from measurements of the full distribution of scattered molecules for this pathway. Rates for V→V energy transfer are at most just a few percent of the V→RT rates, so the appearance rates are a very good description of the collision rate. The depletion rates account for all collisions and in theory should be a better measure of the collision rate. However, the depletion rates are measured directly from a small number of individual HOD states and have larger uncertainty in the appearance rates. For this reason, the appearance rates k_{app} are a better description of the experimentally measured collision rates.

A comparison of the measured collision rates and the Lennard-Jones collision rates is shown in Figure 5.7. The experimentally determined collision rate is 1.7 times larger than the Lennard-Jones rate. The ratio of k_{app} to k_{LJ} for picoline/HOD collisions is 2.5 and for lutidine/HOD the ratio is 3.2. These differences may arise from hydrogen bonding and other intermolecular interactions that are not accounted for by the Lennard-Jones model. It is interesting that the observed enhancements in collision rates scale roughly with the dipole moment of the donor molecule. If the

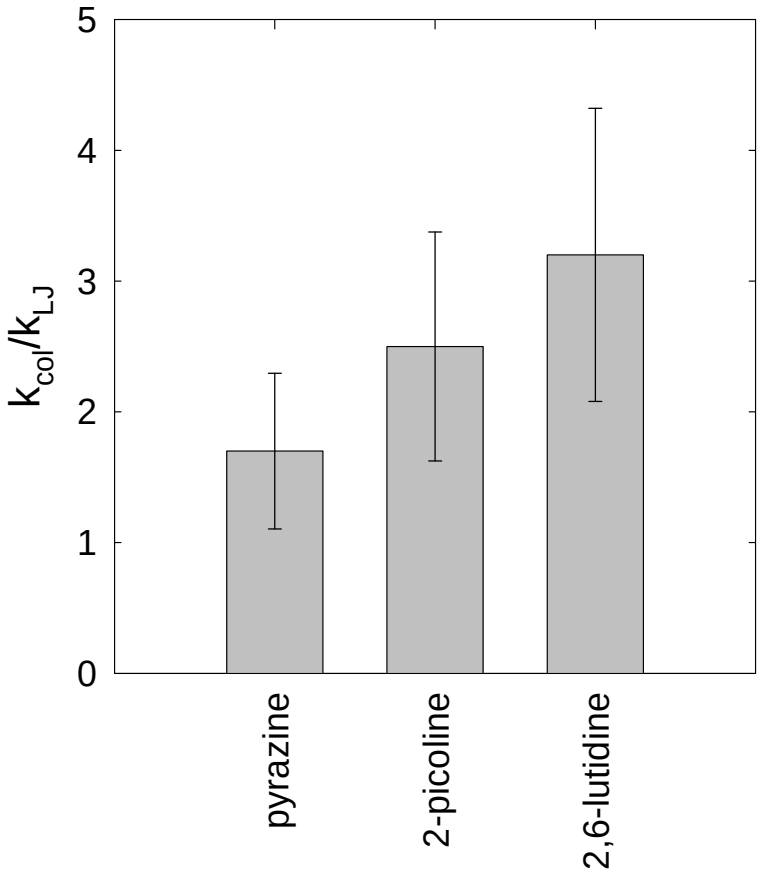

Figure 5.7. Bar graph showing the extent to which the collision rates determined experimentally in this work for collisions between highly vibrationally excited azabenzenes with HOD vary from the Lennard-Jones collision rate. The ratio of k_{col}/k_{LJ} is a lower limit because of the possibility for pathways beyond HOD (000) scattering.

enhancements are due solely to attractive interactions, then ε values would have to increase by factors of ~3.7, ~48 and ~1040 for the pyrazine/HOD, 2-picoline/HOD and 2,6-lutidine/HOD pairs. It is also possible that the effective size of the donor molecules is increased by the larger excursions from equilibrium bond length that occurs when there are large amounts of vibrational energy, thereby increasing the collision rate. For pyrazine, large amplitude motion due to ring breathing and torsion modes is likely to enhance the collision rate. Additional distortions are possible for the methyl groups of 2-picoline and 2,6-lutidine. The larger enhancements observed for the methylated donors is consistent with this idea. Based on the measured collision rates, the Lennard-Jones σ parameter would have to increase by ~1.4, ~1.8 and ~2.1 for pyrazine, 2-picoline and 2,6-lutidine to account for deviations of k_{app} from k_{LJ}. The effect hydrogen bonding on the ratio of k_{app} to k_{LJ} could be tested in future studies by measuring k_{app} for donor/bath pairs with a larger range of intermolecular interactions. The effect of molecular size due to internal excitation could be tested through energy-dependent measurements.

5.3.7 Energy Transfer Probability Distributions

In order to investigate the role of state density in collisions of HOD with highly vibrationally excited pyrazine, 2-picoline and 2,6-lutidine, complete energy transfer probability distributions were determined. This system is the first for which a complete P(ΔE) function has been presented from state-resolved experimental data. The detailed description of getting state-resolved P(ΔE) has been explained in Section 3.3.5. The following parameters were used from the experimental measurements described previously: center-of-mass translational temperatures (T_{rel} in Tables 5.2, 5.3

and 5.4), energy transfer rates for individual states (k_{app} in Tables 5.6, 5.7 and 5.8), and the temperature of the nascent rotational distribution (T_{rot} in Figure 5.5). Translational temperatures were found to be independent of E_{rot}, so the average translational temperature across all states was used. State-resolved energy transfer probabilities $P_J(\Delta E)$ were obtained using Eq. 5.9 and an energy transfer probability curve $P(\Delta E)$ was obtained by summing over all states, $P(\Delta E) = \Sigma P_J(\Delta E)$.[79,161]

$$P_J(\Delta E)\, d\Delta E = \frac{4\pi}{\mu}\frac{k_2{}^J}{k_{col}} g_f \left(\frac{\mu}{2\pi k_B T_{rel}}\right)^{\frac{3}{2}} \exp\left(-\frac{\mu g_f{}^2}{2 k_B T_{rel}}\right) d\Delta E \qquad \text{(Eq. 5.9)}$$

Here, k_B is Boltzmann's constant, μ is the reduced mass and g_f is the final velocity. The energy change ΔE is based on average initial rotational and translational energies at 298 K. Detailed information of calculating $P(\Delta E)$ for donor/HOD collision pairs is give in Appendix D. The energy transfer probability curves for pyrazine, 2-picoline and 2,6-lutidine are shown in Figure 5.8, where k_{col} is described by k_{app}. In this case collisions of pyrazine/HOD have the largest quenching probability. Figure 5.9 shows $P(\Delta E)$ curves when k_{LJ} is used as the collision rate. For this case, quenching of 2,6-lutidine has the highest probability. This illustrates the importance of accurate collision rates.

We can get average energy transfer values $\langle \Delta E \rangle$ from the energy transfer distribution function. This method is expressed using Eq. 5.10

$$\langle \Delta E \rangle = \int P(\Delta E) \Delta E \, d(\Delta E) \qquad \text{(Eq. 5.10)}$$

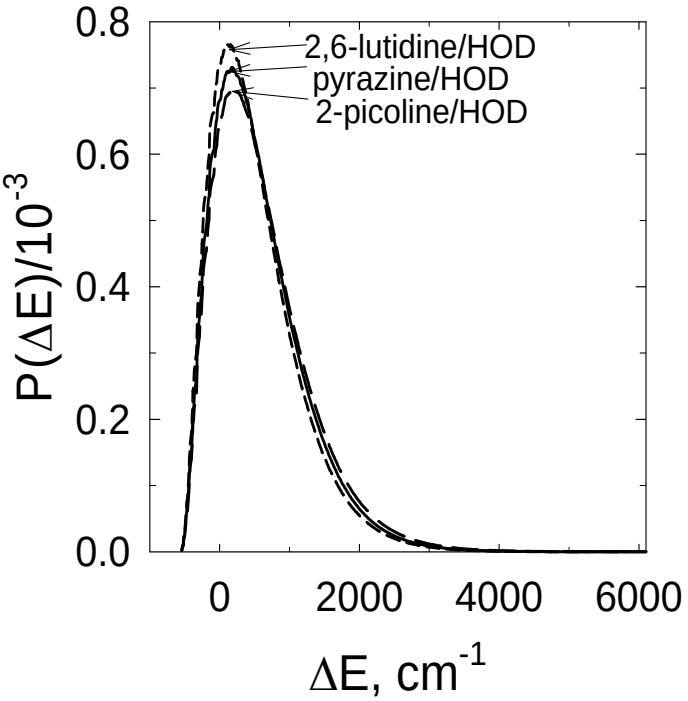

Figure 5.8. Energy transfer probability distribution functions for pyrazine/HOD (solid line), 2-picoline (long dashed line), and 2,6-lutidine (short dashed line) relative to experimentally measured collision rates.

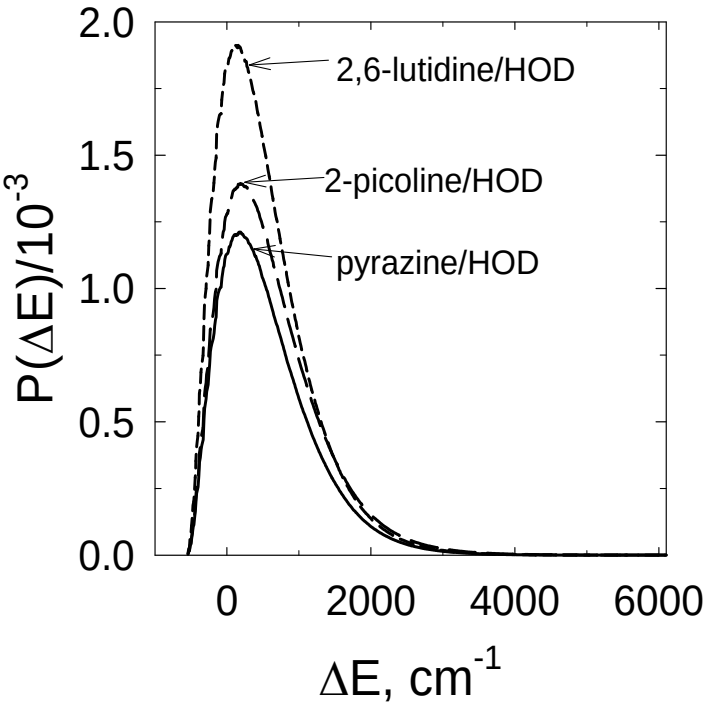

Figure 5.9 Energy transfer probability distribution functions for pyrazine/HOD (solid line), 2-picoline (long dashed line), and 2,6-lutidine (short dashed line) relative to Lennard-Jones collision rates.

When the observed collision rate is used in Eq. 5.9 (ie, $k_{col}=k_{app}$), the P(ΔE) curves in Figure 5.8 are obtained. In this case, the average energy transfer values for pyrazine/HOD, 2-picoline/HOD and 2,6-lutidine/HOD collisions are very similar: $\langle\Delta E\rangle$=554, 601 and 502 cm^{-1} respectively. The similarity of the $\langle\Delta E\rangle$ values comes directly from the observation that the HOD (000) translational and rotational distributions are nearly the same for these donors (Sections 5.3.2 and 5.3.3). When the Lennard-Jones collision rate is used for the collision rate in Eq. 5.9, the P(ΔE) curves in Figure 5.9 are obtained. In this case, the average energy transfer values are $\langle\Delta E\rangle$=918, 1157 and 1254 cm^{-1} for pyrazine, 2-picoline and 2,6-lutidine, respectively. On a per collision basis, this result implies that 2,6-lutidine loses more energy than pyrazine in collisions with HOD. But this is not consistent with the observed scattering distributions that are essentially the same for these donors. Since the Lennard-Jones model underestimates the collision rate, it overestimates the average energy transferred. An accurate description of energy transfer between ensembles of molecules requires both the P(ΔE) curve and an accurate collision rate. While the P(ΔE) curves are similar for these donors, 2,6-lutidine will be actually be quenched faster than pyrazine because it has a higher collision rate.

These P(ΔE) results reported here have interesting ramifications for the interpretation of average energy transfer results that are based on Lennard-Jones collision rates. For example, Miller and Barker found that the $\langle\Delta E\rangle$ values for quenching benzene (E_{vib}) and pyrazine (E_{vib}) by polar bath molecules such as NH_3 is about twice as large as for quenching by CO_2.[162] It is likely that the Lennard-Jones model underestimates the collision rate for polar species such as ammonia and one

cannot conclude that quenching collisions of polar species are necessarily stronger based on $\langle \Delta E \rangle$ values.

It is interesting that the energy transfer distribution functions for HOD are relatively insensitive to the identity of the donor molecule. Full distributions have not been measured for collisions of H_2O, but studies on the strong collisions of H_2O with these donors show that donor identity has a significant effect on the rotational distributions of the scattered H_2O molecules. It is likely that differences in the interaction potentials of HOD and H_2O with these donors are the reason for the observed difference in energy transfer behavior. There is evidence from microwave studies of jet cooled water-pyrazine complexes that HOD has stronger hydrogen bonding interactions than H_2O[95] and the studies reported in Chapter 4 indicate that details of the intermolecular potential surface impact the collisional energy transfer dynamics.

5.4 Conclusion

This work has examined relaxation dynamics of highly vibrationally excited pyrazine, 2-picoline and 2,6-lutidine with HOD. High resolution transient IR absorption was used to measure the full distribution of scattered HOD molecules. These studies were made possible by the development of a new approach for obtaining transient appearance measurements of low energy bath states. Doppler-broadened line profiles, rotational distributions, energy transfer rates and complete energy transfer probability distribution functions were obtained. The scattering profiles for HOD are remarkably similar for quenching the three donors in this study. The scattered HOD (000) molecules have relatively small amounts of rotational and

translational energy. No evidence was seen for collisions that put vibrational energy into HOD. The full energy transfer distribution functions show that the average energy transfer is $<\Delta E>\sim 550$ cm^{-1} for these collision pairs. The overall energy transfer rates show differences for these donors and have the order of 2,6-lutidine>2-picoline>pyrazine.

Molecular collision rates were directly determined from summing over state-specific appearance rates. The observed collision rates for these donors with HOD are all larger than the Lennard-Jones collision rate. Pyrazine/HOD collisions have a rate that is ~1.7 times the Lennard-Jones rate. For 2-picoline/HOD, the collision rate is ~2.5 times the Lennard-Jones collision rate. For 2,6-lutidine/HOD, this ratio is ~3.2. The enhancement in collision rate is likely due to hydrogen bonding interactions, internal energy of the highly excited donors or both. Studies of this type provide an important benchmark for developing more accurate models of collisional energy transfer and collision rates.

Chapter 6: Effect of Vibrational Energy on the dynamics of D-atom Abstraction Reactions of Pyridine-d_5 (E_{vib}=38,068 cm^{-1}) and 2-Picoline-d_3 (E_{vib}=38,328 cm^{-1}) with Chlorine Radical

6.1 Introduction

It is well known that increasing the energy in chemical reactions generally leads to enhancements in reaction rates.[163-169] This concept is embodied in the Arrhenius equation that describes the temperature dependence of reaction rate constants. Heating a reaction mixture deposits energy in internal and translational motion which in turn can lead to increases in rates of chemical reactions. At the microscopic level, a number of experiments have shown that for small molecules, if energy is added to reactants and that energy corresponds to motion along the reactive coordinate, substantial rate enhancements are observed. For example, Crim and coworkers showed that in reactions of HOD + Cl the OD + HCl product channel is enhanced by a factor of 40 if 4 quanta in the O-H stretch were pumped into HOD prior to reaction.[170] Zare and coworkers have observed rate enhancements in reactions of CH_4 + Cl when CH_4 is vibrationally excited.[163,165,166,171] They measured a rate enhancement of more than 30 when the one quantum of the C-H antisymmetric stretch mode was pumped. In both of these cases, the added vibrational energy corresponds to the motion along the reaction coordinate,[163] but this need not be the case. Zare and coworker have found that the CH_4 + Cl reaction is enhanced not only

by the ν_3 stretching mode, but also to lesser degrees by the symmetric stretch, bending and torsional modes.[169,172]

Different types of energy can have different effects on the rates of reaction. In direct reactions of atoms with diatomic molecules, the location of the transition state with respect to the reaction coordinate determines the type of energy that will best promote the reaction. This concept is embodied by the Polanyi Rules.[173] Reactions with "early" transition states are promoted most by translational energy in the reactants while rates for the "late" barrier reactions are enhanced by vibrational energy in the reactants. Such a clear distinction is not likely to be the case for polyatomic reactions where configuration space is quite large. Liu and coworkers explored how vibrational energy compares to translational energy in reactions of CHD_3 with Cl.[168] They found that the vibrational excitation of the CH stretch was just as effective at increasing the reaction efficiency as an equal amount of energy in translation. They also observed differences in the product states based on the type of energy in the reactants.

Understanding how internal energy affects reactions of large polyatomic molecules remains an open question. Preparing polyatomic molecules with well-defined amounts of vibrational energy in particular modes is challenging because intramolecular vibrational redistribution (IVR) often occurs before the molecules react.[174] Typical IVR lifetimes for benzene-like molecules are on the picosecond time scale. Following IVR, molecules have less energy available along the reaction coordinate, and reaction rates can be lower than expected. Sometimes the energy remaining in the reaction mode is even lower that the reaction barrier, giving no

reaction at all. In the studies described in this chapter, we have circumvented the challenges that IVR poses by preparing vibrationally excited reactants with large amount of internal energy through radiationless decay rather than putting vibrational energy directly into a single reactive mode. For example, when pyridine-d_5 absorbs light at λ=266 nm, it undergoes internal conversion from S_1 to S_0 with unity quantum yield and a lifetime of 60 ps, resulting in a vibrationally excited reactant with E_{vib}=38,068 cm^{-1} of internal energy. The energy becomes randomized throughout the molecule by IVR, leaving the C-D stretches with a average energy of $\langle E_{vib} \rangle$=985 cm^{-1}.

In this chapter, the effect of vibrational energy on D-atom abstraction reactions of highly vibrationally excited pyridines with chlorine radicals is explored. The pyridine reactants are vibrational excited by pulsed 266 nm light. Chlorine radicals are prepared simultaneously by photolysis of Cl_2 at 355 nm. The chlorine radicals have a relative translational energy of E_{rel}= 2990 cm^{-1} due to the photodissociation. The nascent DCl product are detected by high resolution transient IR absorption spectroscopy at λ=4.5 μm. Two D-atom abstraction reactions are considered here: pyridine-d_5 + Cl and 2-methyl-d_3-pyridine + Cl. The first reaction is abstraction from an aromatic carbon and the second is abstraction from a methyl carbon. As shown in Figure 6.1, the first reaction an endothermic reaction with an enthalpy of ΔH=8.8 kcal/mol. The second reaction is an exothermic reaction with an enthalpy of ΔH=-13.6 kcal/mol. For both reactions, the DCl products are characterized in terms of their vibrational, rotational and translational energy distributions and absolute rate constants are measured as a function of reactant vibrational energy.

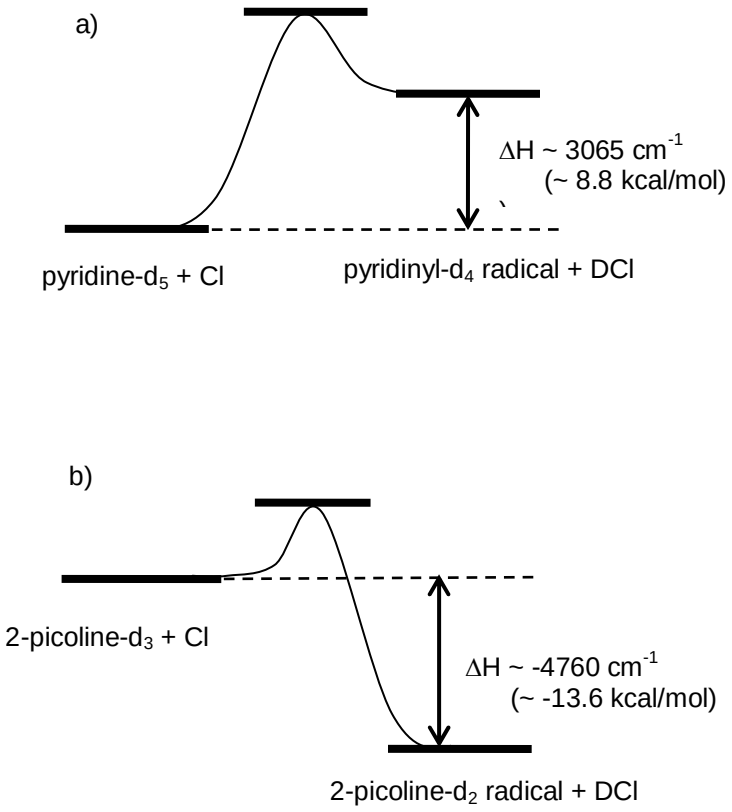

Figure 6.1. Enthalpy for reactions of pyridine-d_5 with Cl (a) and 2-picoline-d_3 with Cl (b).

6.2 Experimental Setup

High resolution transient IR absorption experiments were performed to investigate reactions of highly vibrationally excited molecules and chlorine radicals. A high resolution transient IR absorption spectrometer operating at λ=4.5 μm was modified to provide simultaneous output at λ=266 nm and λ=355 nm. Pulsed 266 nm light absorption from the 4th harmonic output from a pulsed Nd:YAG laser was used to prepare vibrationally excited pyridine molecules with E_{vib}~38,200 cm^{-1}.[62,109] Chlorine radicals were produced by photodissociation of Cl_2 by circularly polarized 355 nm light. The chlorine radicals have a relative translational energy of E_{rel}=2990 cm^{-1} in collisions with pyridine molecules. The 266 nm and 355 nm UV pulses were kept below 4.5 MW/cm^2 and 6.2 MW/cm^2, respectively, to ensure a linear dependence of the DCl transient absorption signal and the UV absorption. The UV laser beams and the single mode output of a lead salt diode laser at λ=4.5 μm were merged and copropagated through a 3 meter reaction cell. A 1:1 mixture of pyridine and chlorine gas was used. The total pressure of reactants was maintained below 50 mTorr. The DCl transient absorption signals were linear with respect to the range of pressures used in this study. Transient IR spectroscopy was used to monitor the population growth of DCl products from the reactions.

For the pyridine-d_5 + Cl study, four reactions need to be considered.

Reaction A $$\text{pyridine}-d_5(298\text{K}) + \text{Cl} \xrightarrow{k_A} \text{pyridinyl}-d_4 + \text{DCl} \qquad \text{(Eq. 6.1)}$$

Reaction B $\quad pyridine-d_5(E_{vib}) + Cl \xrightarrow{k_B} pyridinyl-d_4 + DCl$ (Eq. 6.2)

Reaction C $\quad pyridine-d_5(298K) + Cl_2 \xrightarrow{k_C} pyridinyl-d_4 + Cl + DCl$ (Eq. 6.3)

Reaction D $\quad pyridine-d_5(E_{vib}) + Cl_2 \xrightarrow{k_D} pyridinyl-d_4 + Cl + DCl$ (Eq. 6.4)

Reaction A (Eq. 6.1) shows the DCl products coming from the reaction of room temperature pyridine-d_5 and chlorine radical, while Reaction B (Eq. 6.2) describes the DCl products coming from reaction of vibrationally excited pyridine-d_5 with chlorine radical. Reactions of room temperature and vibrationally excited pyridine-d_5 with molecular chlorine are shown in Eq. 6.3 and 6.4 and labeled as Reaction C and Reaction D, respectively.

High resolution transient IR absorption was used to probe product DCl molecules as shown in Eq. 6.5.

$$DCl\ (v=0, J,V) + h\nu\ (\lambda \sim 4.6 - 5.2\ \mu m) \rightarrow DCl\ (v=1, J\pm1, V) \quad \text{(Eq. 6.5)}$$

where v is the DCl vibrational quantum number, J is the rotational quantum number and V stands for the velocity vector along the IR probe axis.

Table 6.1 describes the experimental conditions with the corresponding reactions. A static cell experiment with total pressure of over 50 mTorr showed that reaction C was not detectable in our experiment. This gives an estimated upper limit of the rate for reaction C of $k_C(J=4)<10^{-15}$ cm^3 $molecule^{-1}$ s^{-1}. Transient signals are observed for reactions A, B and D. Figure 6.2 shows the transient absorption signal

Table 6.1. Experimental conditions with the corresponding reactions for pyridine-d_5 and chlorine.

	I	II	III	IV
λ=355 nm	off	on	off	on
λ=266 nm	off	off	on	on
Reaction	C	A, C	C, D	A, B, C and D

Reaction A = S(II, ν_0) - S(II, ν_d)

Reaction B = S(IV, ν_0) - S(II, ν_0) - S(III, ν_0)

Reaction D = S(III, ν_0) - S(III, ν_d)

Here ν_0 is the line center of the IR transition and ν_d is the frequency when the IR is detuned from the transition. S(II, ν_0) stand for the transient signal measurement at case II at DCl transition line center, and S(II, ν_d) stand for the transient signal measurement at case II at detuned IR frequency. Similar notations are used in getting the signals for Reactions B and D.

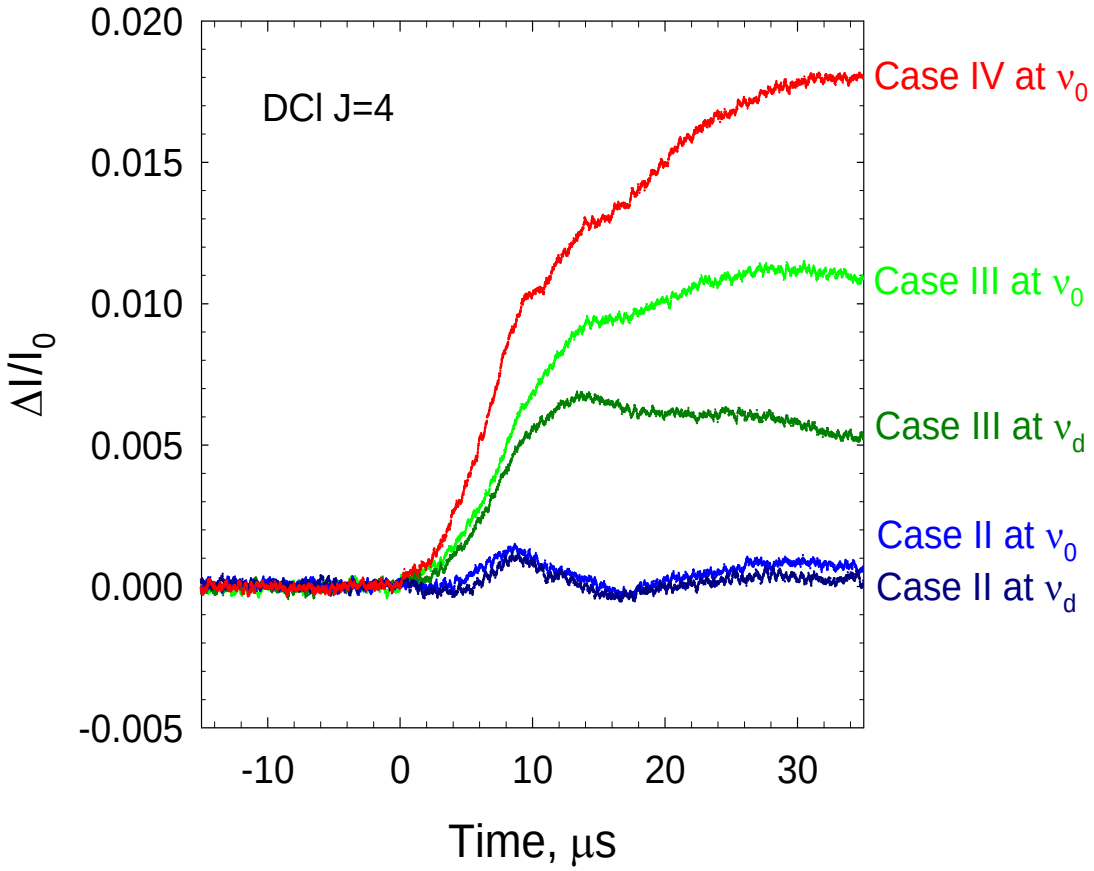

Figure 6.2. Raw fractional IR absorption signal of $D^{35}Cl$ (v=0) J=4 coming from reaction of pyridine-d_5 with chlorine. The IR frequency at line center is ν_0. The IR frequency detuned from line center is ν_d.

of DCl (v=0) J=4 under conditions II – IV. Thermal lensing and broad band IR absorption of vibrationally excited molecules also show a transient-like signal when the IR is not tuned to a DCl transition. Transient signals were collected at line center ν_0 of the IR transition and at ν_d with the IR detuned from the transition. Information about the individual reactions is obtained using the conditions outlined in Table 6.1. Signals due to reaction A are obtained using 355 nm light only (case II) and taking the difference between signal at ν_0 and at ν_d. This removes the signal due to the broad background induced by the 355 nm light. Information about reaction D is obtained in similar way using 266 nm light only (case III). In the presence of both 266 and 355 nm light (case IV), the signal has contributions from reactions A, B and D and the broad background signals. Information about reaction B is obtained by removing the signals for case II at ν_0 and for case III at ν_0 from the signal for case IV at ν_0.

Research grade Cl_2 (Airgas, 99.9+%) and DCl (Cambridge Isotope Laboratories, 98+%) were used without further purification. Pyridine-d_5 (Aldrich, 99.5 atom % D) and 2-methyl-d_3-pyridine (CDN Isotopes, 99.7 atom % D) were purified through several freeze/pump/thaw cycles prior to use.

6.3 Results and Discussion

The dynamics of the hydrogen abstraction reactions of deuterated pyridine with Cl radicals are reported here. The quantum state and recoil velocity distributions of the DCl products have been measured by transient IR absorption spectroscopy. Figure 6.3 shows the effect of pyridine vibration on the appearance of DCl (v=0) J=4 products. The lower frame of Figure 6.3 shows the DCl population appearance with

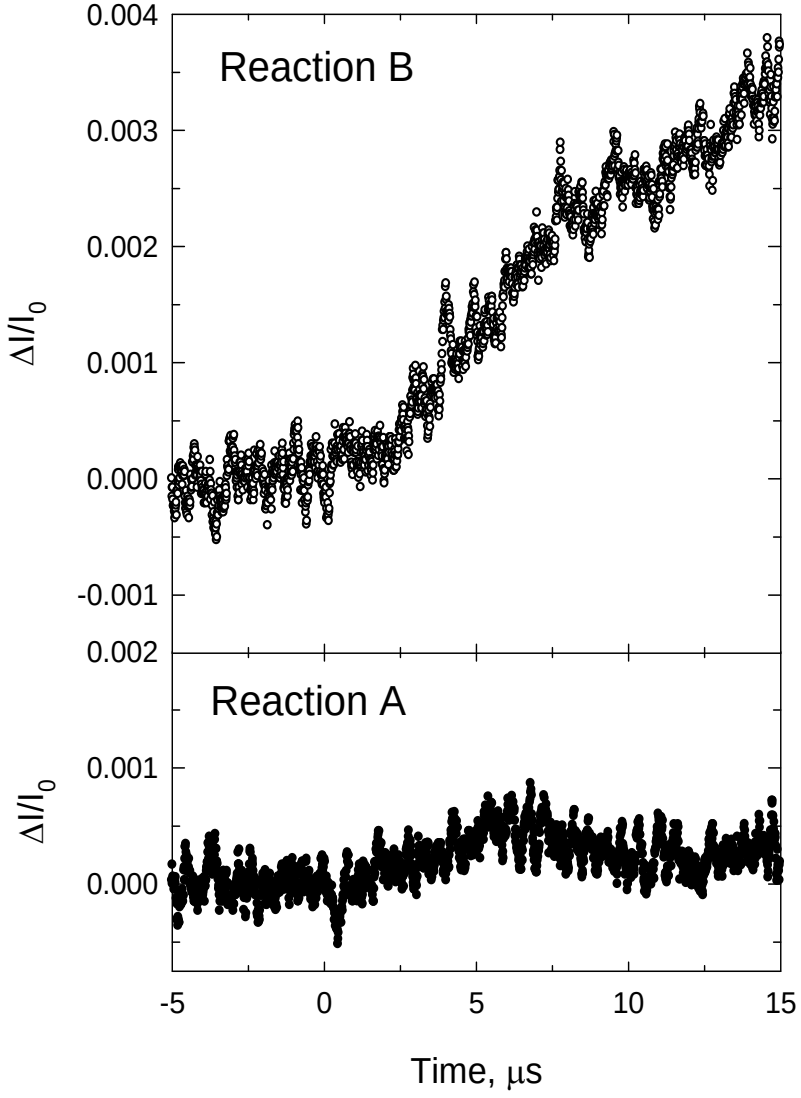

Figure 6.3. Fractional IR absorption of $D^{35}Cl$ (v=0) J=4 coming from reaction of pyridine-d_5 with chlorine radical, with and without vibrational energy (E_{vib}=38,068 cm^{-1}) in pyridine-d_5.

respect to the time coming from the reaction of room temperature pyridine-d_5 molecules with Cl (Reaction A). The upper frame of Figure 6.3 shows the DCl population growth coming from reaction of highly vibrationally excited pyridine-d_5 molecules with Cl (Reaction B). The transient signal from Reaction B has a linear growth between t=0 to 10 μs. The amount of products from Reaction A is significantly smaller. The fractional absorption signals $\Delta I/I_0$ at t=5, 10, 15 and 18 μs were used to determine the Doppler-broadened linewidths that are described in the next section.

6.3.1 Nascent Translational Energy of DCl Products

Translational energy distributions of the DCl products of Reaction B were determined from the Doppler-broadened linewidths of individual DCl (v=0) J states. Figure 6.4 shows linewidth profiles at t=5, 10, 15 and 18 μs for $D^{35}Cl$ (v=0) in the J=4 state. The frequency of the probe transition is 2141.54 cm^{-1} and the rotational energy of the J=4 state is E_{rot}=107.79 cm^{-1} based on the FTIR results from Parekunnel *et al.*[175] The linewidth profile (symbols) at each time was fit to a single Gaussian function (solid line) to extract the information of the full width of half maximum (FWHM). The FWHM is $\Delta\nu_{obs}=7.83\times10^{-3}$ cm^{-1} for $D^{35}Cl$ (v=0) J=4 state at 5 μs, which corresponds to a translational temperature of 1225 K.

The average collision time for DCl products is τ_{col}=~1 μs and the translational temperature of DCl products decreases with time due to sequential collisions with other molecules in the reaction cell. In order to get the translational energy of nascent DCl products before they undergo secondary quenching collisions, the time dependent linewidths were fit to an exponential decay and linewidths at t=1 μs were

extrapolated, as shown in Figure 6.4. For the $D^{35}Cl$ J=4 state, the lab frame translational temperature at t=1 μs is T_{trans}(lab)= 1760±350 K. The observation that the DCl products have excess translational energy is consistent with the Polanyi's rules for late barrier reactions,[173] namely that vibrational energy in the reaction coordinate makes it easier to overcome late reaction barriers and leads to products with excess translational energy. Additional measurements were performed to look for DCl products in the v=1 state, but transient signals of the DCl (v=1) product state were below the experimental detection limit. This result places an upper bound to the rate for production of the DCl (v=1) J=6 state of $k<10^{-15}$ cm^3 $molecule^{-1}$ s^{-1}. This result is also consistent with the Polanyi's rules.[173]

The Doppler-broadened line profiles and nascent translational temperatures for a number of DCl (v=0) rotational states were measured and are listed in Table 6.2. The nascent translational temperatures for the J=4, 5, 8 and 13 rotational states are between T_{trans}(lab)=900 and 1800 K. These states have rotational energies of E_{rot}=100 to 1000 cm^{-1}. We note that all DCl product states have translational energy. There appears to be a slight decreasing trend in the translational temperature for the nascent DCl products as a function of product rotational state.

We were unable to measure the Doppler-broadened linewidths for DCl products coming from Reaction A given the signal to noise levels of this study. A room temperature linewidth was used in population and rate determinations. Given that the Reaction A is endothermic and the reactant collision energy is near the activation energy, it is reasonable that the DCl products do not contain large amounts of translational energy.

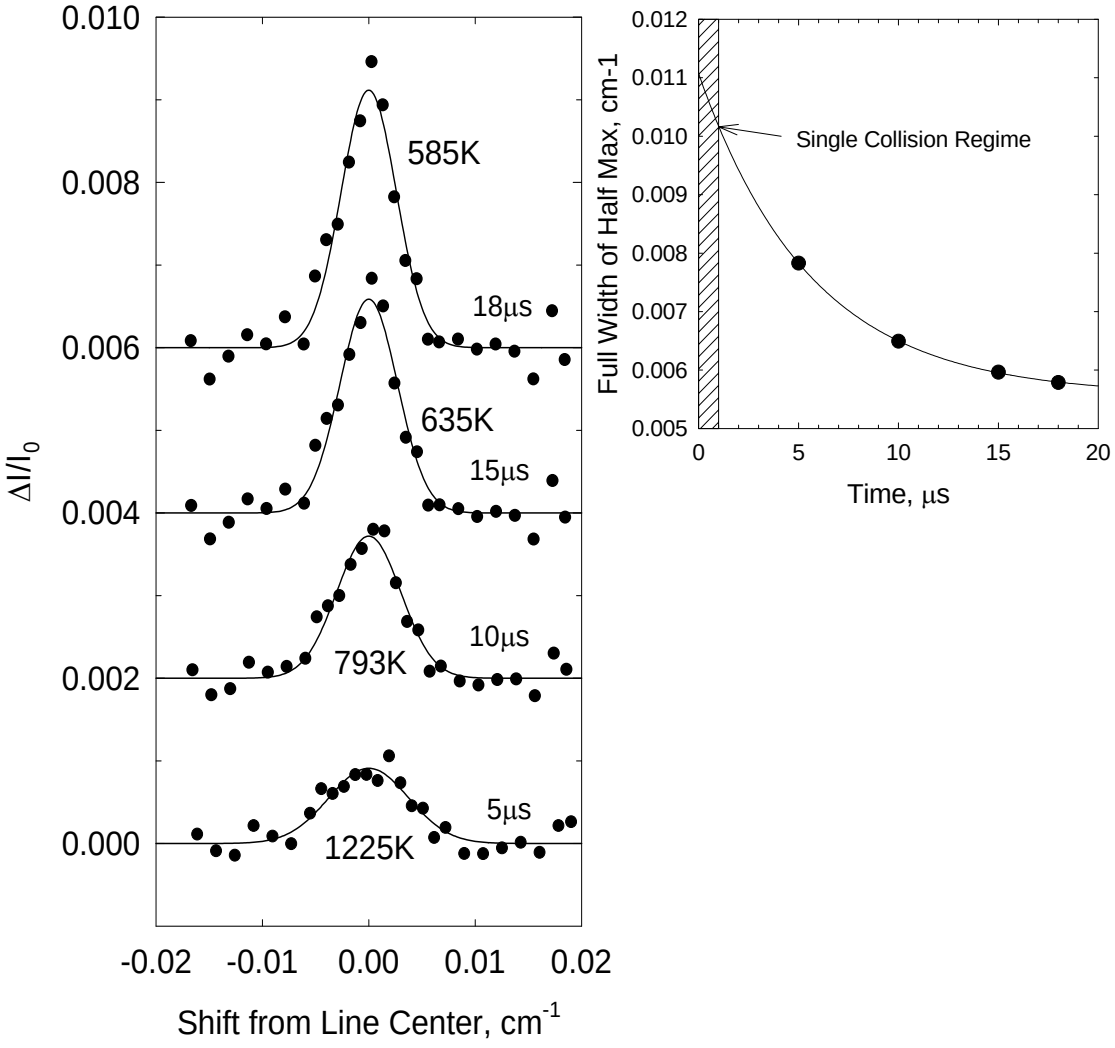

Figure 6.4. Transient absorption lineshapes for $D^{35}Cl$ (v=0) J=4 collected at t=5, 10, 15, 18 μs following UV excitation of pyridine-d_5 and photodissociation of Cl_2. The lineshapes at t=5, 10, 15, 18 μs are offset for clarity. The time evolution of the Doppler-broadened linewidths (black dots) and exponential fitting are shown on the right.

Table 6.2. Doppler-broadened linewidth measurements and lab frame translational temperatures of nascent DCl (v=0) product coming from the reaction of highly vibrationally excited pyridine-d_5 molecules and chlorine radicals at 1 μs after the 266 nm and 355 nm UV pulse.

Product State	E_{rot}, cm^{-1}	ν_0, cm^{-1}	$\Delta\nu_{obs}$, cm^{-1} a)	T_{trans}(lab), K[b)]
$D^{35}Cl$ J=4	107.79	2141.54	0.0102±0.001	1630±320
$D^{37}Cl$ J=5	161.17	2147.76	0.0091±0.001	1370±300
$D^{35}Cl$ J=8	386.39	1996.06	0.0096±0.001	1650±390
$D^{35}Cl$ J=13	976.77	1934.58	0.0069±0.001	930±270

a)The full width at half maximum linewidth at t=1 μs from fitting the t=5, 10, 15, 18 μs transient line profile to a Gaussian function. The linewidth data were plotted as a function of time, and the linewidth at 1 μs was extrapolated. The uncertainty in linewidth is ±0.001 cm^{-1} and is known by measuring a room temperature linewidth of CO_2 to 0.001 cm^{-1} precision.

b The lab frame translational temperature is found using $T_{trans}(lab) = \left(\frac{mc^2}{8k_B \ln 2}\right)\left(\frac{\Delta\nu_{obs}}{\nu_0}\right)^2$ where m is the mass of DCl, c is the speed of light, k_B is Boltzmann's constant, ν_0 is the IR transition frequency and $\Delta\nu_{obs}$ is the nascent Doppler-broadened line width.

6.3.2 Nascent Rotational Distribution of DCl Products

The rotational distributions of DCl products coming from Reactions A and B are shown in Figure 6.5. The DCl products from pyridine-d_5 (E_{vib}=38,068 cm^{-1}) + Cl reaction have a rotational distribution with T_{rot}=320±30 K. The DCl products from pyridine-d_5 (298K) + Cl reactions have a rotational temperature of T_{rot}=440±70 K. The lack of excess rotational energy in the DCl products indicates that the transition state is linear in the C-D-Cl structure. This result is consistent with studies on the CH_4 +Cl reaction from Zare[176] and coworkers and the cyclohexene + Cl reaction from Flynn and coworkers[177] who also reported v=0 products with small amounts of rotational energy.

6.3.3 Reaction Rate and Rate Enhancement

Absolute rate constants for Reactions A and B have been determined based on the appearance of product DCl (v=0) in J states. The differential rate expression for appearance of individual product states of DCl (v=0) is written as Eq. 6.6,

$$\frac{d[DCl(v=0,J)]}{dt} = k_B{}^J[\text{Pyridine}-d_5(E_{vib})]_0[Cl]_0 \qquad \text{(Eq. 6.6)}$$

where [DCl(v=0, J)] represents the population of DCl (v=0) in J rotational state, t is the time following UV excitation of pyridine-d_5, and $k_B{}^J$ is the abstraction reaction rate constant for appearance of a DCl (v=0) J state from Reaction B, [Pyridine-$d_5(E_{vib})]_0$ is the concentration of excited pyridine-d_5 molecules, and $[Cl]_0$ is the concentration of Cl radicals.

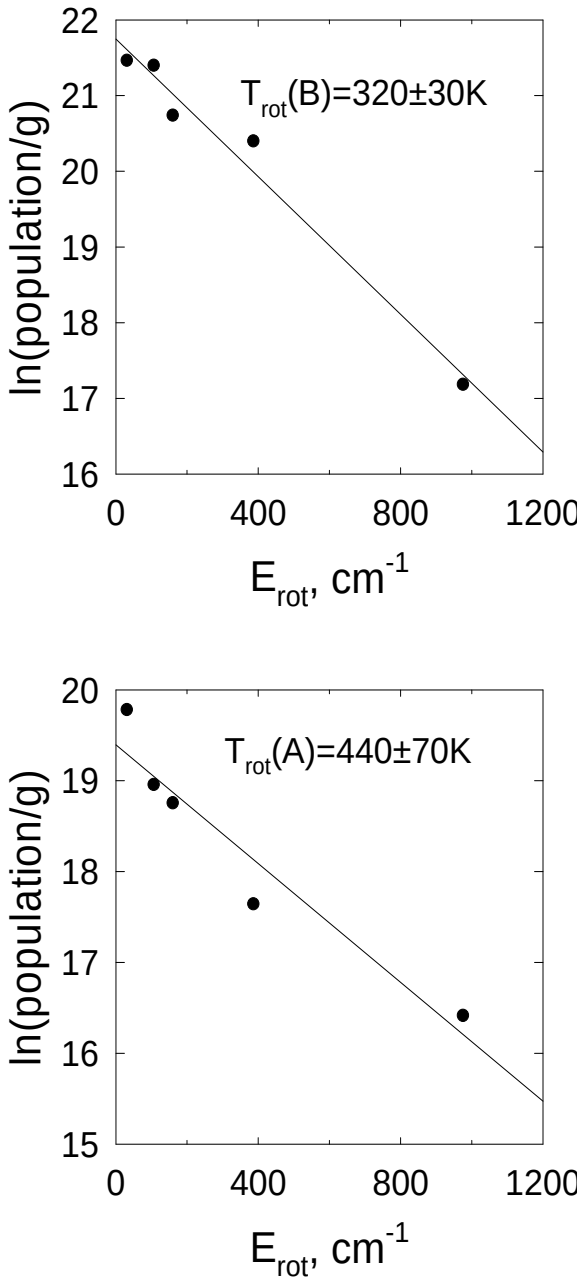

Figure 6.5. Rotational distribution of nascent DCl product coming from Reaction B and Reaction A for reaction of pyridine-d_5 with Cl.

From Figure 6.3, the transient absorption signal is linear from 0 to 10 μs. The DCl product concentration is determined from a linear fit of the data with zero offset. At t=1 μs the concentrations of the reactants are essentially the same as the values at t=0, so the concentration of reactants at t=0 μs are used. The change in concentration of a DCl product state at Δt=1 μs is determined from the fractional transmitted IR intensity at t=1 μs. [Pyridine-$d_5(E_{vib})$]$_0$ and [Cl]$_0$ are determined by measuring the number of UV photons absorbed by pyridine-d_5 and Cl_2 and dividing by the laboratory interaction volume. One 355 nm photon generates two Cl radicals from the photodissociation of Cl_2. To determine the reaction rate constants k_A^J for Reaction A, the bulk pyridine-d_5 pressure is used instead of [Pyridine-$d_5(E_{vib})$]$_0$.

The rate constants for the appearance of product DCl (v=0) in J states resulting from Reactions A and B are shown in Table 6.3. For $D^{35}Cl$ products in J=8 state, a reaction rate constant of $k_B^J=(13\pm4) \times 10^{-13}$ cm^3 molecule^{-1} s^{-1} is measured for Reaction B. The comparable rate constant for the 298K reaction is $k_A^J=(8\pm2) \times 10^{-15}$ cm^3 molecule^{-1} s^{-1}. This shows a rate enhancement of ~160 for the $D^{35}Cl$ J=8 state. A comparison in Table 6.3 shows that on average the vibrational energy in pyridine-d_5 molecules enhances the reaction rate by a factor of ~90.

Total reaction rate constants are obtained by summing over the rotational distribution of the DCl product states. The total rate constant for Reaction A is $k_A=(1.3\pm0.4) \times 10^{-13}$ cm^3 molecule^{-1} s^{-1}. The total rate constant for Reaction B is $k_B=(1.17\pm0.35) \times 10^{-11}$ cm^3 molecule^{-1} s^{-1}. Overall, the rate enhancement is 90±39 due to vibrational energy in pyridine.

Table 6.3. Reaction rate constant of nascent DCl product coming from the reaction of room temperature pyridine-d_5 with Cl (Reaction A) and reaction of highly vibrationally excited pyridine-d_5 with Cl (Reaction B).

Product State	Reaction A[a)] $k_A^J \times 10^{-15}$ $cm^3\ molecule^{-1}\ s^{-1}$	Reaction B $k_B^J \times 10^{-13}$ $cm^3\ molecule^{-1}\ s^{-1}$	Rate Enhancement k_B/k_A
$D^{37}Cl$ J=2[c)]	16±5	11±3	66±28
$D^{35}Cl$ J=4	13±4	18±5	140±60
$D^{37}Cl$ J=5	13±4	11±3	89±38
$D^{35}Cl$ J=8	8±2	13±4	156±66
$D^{35}Cl$ J=13	3±1	0.8±0.2	26±11
$k_X = \sum_{All\ J} k_X^J$ [b)]	k_A=126±38	k_B=117±35	90±39

[a)]Room temperature linewidths were used to calculated the nascent population distribution from Reaction B.

[b)]Integrated rate constant k_X is calculated by summing all the predicted rates from rotational distribution for reaction X.

[c)]$D^{37}Cl$ J=2 nascent population was calculated from the fractional absorption and the estimated linewith. The linewidth for $D^{37}Cl$ J=2 state was estimated from the linear extrapolation based on linewidth measurement for other states.

There is also evidence that translational energy promotes the A-atom abstraction reaction. In our experiments, the Cl radicals have translational energy that is near the reaction threshold. The rate constant for Reaction A with thermalized Cl radicals at 298 K has been investigated by Wine and coworkers using laser flash photolysis-resonance fluorescence technique.[178] They reported a rate constant of $k=(6.3\pm1.4) \times 10^{-14}$ cm^3 $molecule^{-1}$ s^{-1}, which is about half of the value reported here. We attribute the difference to the influence of reactant translational energy.

6.3.4 Energy Use in of D-Abstraction Reaction of Pyridine-d_5 + Cl

In order to extract information about the energy that is used in Reaction B, a complete vector analysis was applied to the data in Table 6.2. Figure 6.6 is the Newton diagram for reactive collisions of pyridine-d_5 with Cl radicals. The velocity of pyridinyl-d_4 radical after the reaction, v_3, can be expressed using the following information: the velocity of room temperature pyridine-d_5 (v_1), the velocity of Cl after 355 nm dissociation (v_2), and the velocity of DCl measured from the Doppler-broadened linewidths (v_4). The relative velocity of the reaction products, v'_{rel}, and the relative translational energy between the reaction products E'_{rel} can be expressed using the vectors v_3 and v_4. A numerical solution to v_3 was obtained by averaging over the angles and velocity spreads in the reactants and products. This yields v'_{rel} and E'_{rel}. Details of this analysis are given in Appendix E.

The energy schematic for $D^{35}Cl$ J=4 product state is presented in Figure 6.7. On the reactant side, the relative translational energy for the reactants is 2990 cm^{-1}, and the vibrational energy of pyridine-d_5 is E_{vib}=38,068 cm^{-1}. On the product side, for reactions at the meta- and para- C-D bond in pyridine-d_5 molecules, the enthalpy

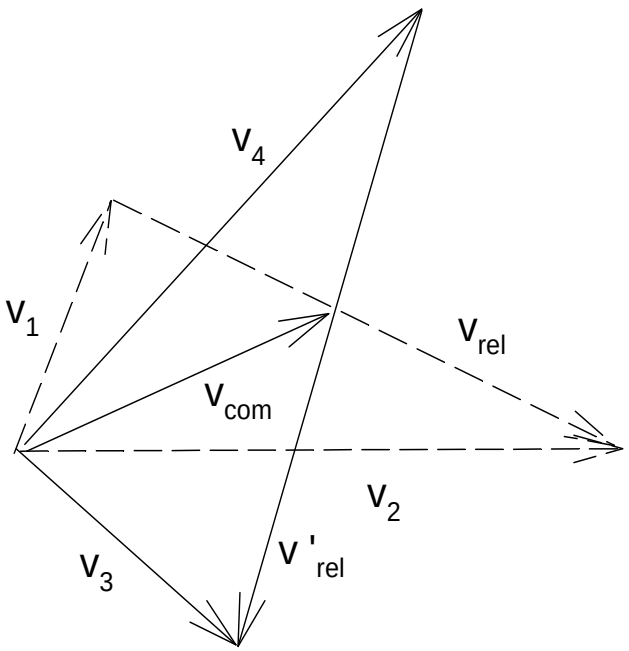

Figure 6.6. Newton diagram of D-atom abstraction reaction. $\mathbf{v_1}$ and $\mathbf{v_2}$ stand for the velocity of room temperature pyridine-d_5 and the velocity of Cl after 355 nm dissociation, respectively. The angle between $\mathbf{v_1}$ and $\mathbf{v_2}$ is θ. Their relative velocity is $\mathbf{v_{rel}}$. The velocity of pyridinyl-d_4 radical after the reaction is $\mathbf{v_3}$, and the velocity of DCl measured from the Doppler-broadened linewidths is $\mathbf{v_4}$. The angle between $\mathbf{v_3}$ and $\mathbf{v_4}$ is ϕ. The relative velocity of the reaction products is $\mathbf{v'_{rel}}$. $\mathbf{v_{com}}$ is the center of mass velocity. In this case the vector of center of mass velocity does not change before and after the D-atom abstraction reactions.

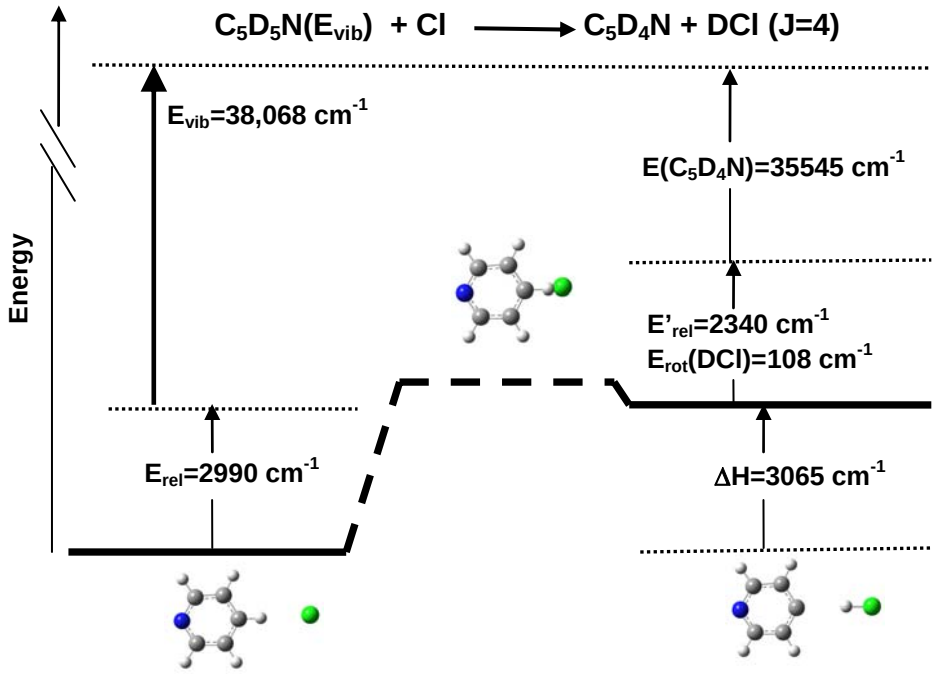

Figure 6.7. The energy schematic of the reaction of highly excited pyridine-d_5 (E_{vib}=38,068 cm^{-1}) with Cl to give $D^{35}Cl$ J=4 product. On the reactant side, the relative translational energy between pyridine-d_5 and Cl is E_{rel}=2990 cm^{-1}. Pyridine-d_5 molecules have vibrational energy of E_{vib}=38,068 cm^{-1}. The reaction is an endothermic reaction. On the product side, the reaction enthalpy is ΔH=3065 cm^{-1}. DCl v=0 J=4 products has relative translational energy of E'_{rel}=2340 cm^{-1} and rotational energy of E_{rot}=108 cm^{-1}. The energy left in pyridinyl radicals is E=33,545 cm^{-1}.

of the reaction is ΔH=3065 cm^{-1}. The $D^{35}Cl$ (v=0) J=4 product has a rotational energy of 108 cm^{-1}. The relative translational energy for product is E'_{rel}=2340 cm^{-1}. We find that most of the vibrational energy stays in the pyridinyl-d_4 radicals after the reaction.

The energy difference between pyridine-d_5 reactant and pyridinyl-d_4 product is defined as the energy used for the reaction, $E_{used}=E_{vib}-E_{rad}$. Values of E_{used} are listed in Table 6.4 and shown in Figure 6.8. The calculation is based on D-atom abstraction reaction from the meta- and para- C-D sites in pyridine-d_5 molecules. The difference in meta-, para-, ortho- abstraction will be addressed in the next paragraph. E_{used} values are independent of rotational energy and have values of ~2500-2800 cm^{-1}. These values are very close to 2200 cm^{-1}, which is the energy of one quantum of C-D stretch in pyridine-d_5. This result implies that a single quantum of C-D stretch is used in the reaction.

It is surprising to see that a large amount of vibrational energy of E_{vib}=38,068 cm^{-1} in pyridine-d_5 actually produces DCl molecules with relative small amount of translational energy and that one quantum of C-D stretch in the highly vibrationally excited pyridine-d_5 molecules is used during the reaction. On average the C-D stretch contains an average energy per mode of $\langle E\rangle$~1000 cm^{-1}. The observation that a single quantum of C-D stretch is used in the reaction is reminiscent of the results for abstraction from small molecules like CH_4, namely the local excitation in the reactive coordinate is used in the reaction and the rest of the molecule acts like a spectator. The reactant contains ~37,920 cm^{-1} of vibrational energy, but only uses 2500 cm^{-1}.

Table 6.4. Lab frame velocity of DCl product, v_4, from reaction of highly vibrationally excited pyridine-d_5 with chlorine radical, relative velocity of DCl product to pyridinyl-d_4 radical, v'_{rel}, and energy used, E_{used}, for the reaction.

States	E_{rot}, cm^{-1}	$\langle v_4 \rangle$ [a)], m/s	v'_{rel} [a)], m/s	E_{used} [a)], cm^{-1}
$D^{35}Cl$ J=4	107.79	1048±103	1482±115	2526±615
$D^{37}Cl$ J=5	161.17	1375±103	1390±114	2498±587
$D^{35}Cl$ J=8	386.39	1055±110	1490±121	2831±629
$D^{35}Cl$ J=13	976.77	926±114	1228±119	2665±587

[a)]Detailed description of calculating $\langle v_4 \rangle$, v'_{rel} and E_{used} is shown in Appendix E.

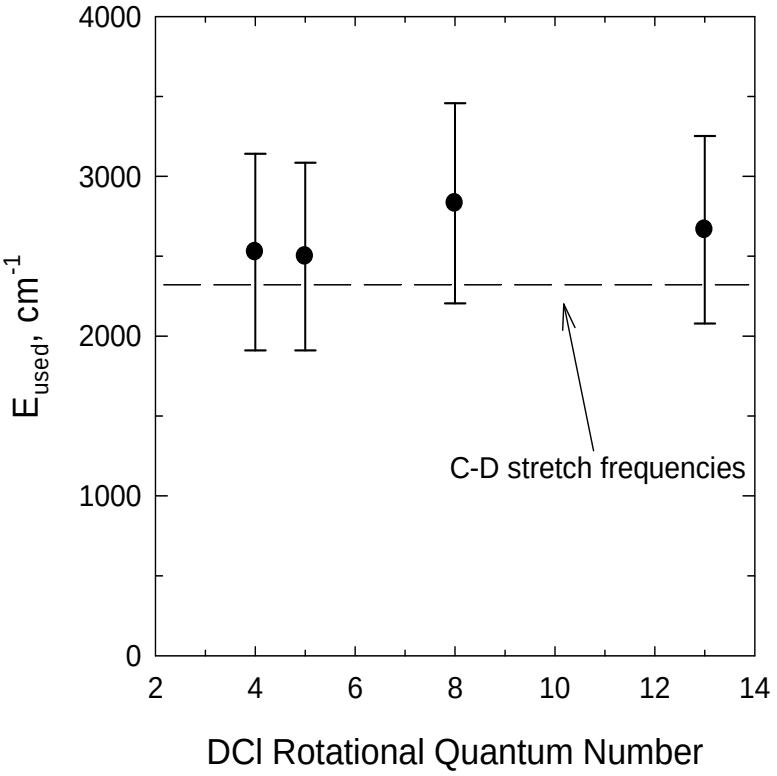

Figure 6.8. The energy used for reaction of highly excited pyridine-d_5 (E_{vib}=38,068 cm^{-1}) with Cl for different DCl (v=0) J states.

Another way to view this is that the D-atom abstraction reaction occurs on a timescale that is fast compared to the timescale of IVR.

For reactions that abstract from the ortho- C-D site, the enthalpy of the reaction is ΔH=610 cm^{-1}.[179] For this reaction the energy used for D-atom abstraction reaction is only E_{used}=70 cm^{-1}. This result means the reactions on the ortho-C-D bond occurs without using any vibrational energy in the reactant. By putting vibrational energy of 38,068 cm^{-1} into pyridine-d_5 molecules, the meta- and para- sites become available for the D-atom abstraction reaction.

6.3.5 D-atom Abstraction Reaction of Picoline-d_3 and Cl

Additional studies were performed to investigate how vibrational energy affects D-atom abstraction reactions from methylated reactants. In these studies, the D-atom abstraction involves the reaction of 2-methyl-d_3-pyridine (2-picoline-d_3) with chlorine radical. The reaction was studied using high resolution transient IR absorption at λ=4.5 μm to monitor the appearance of DCl product molecules. At 298 K, the reaction is exothermic with ΔH= -13.6 kcal/mol, as shown in Figure 6.1b. Eq. 6.7 describes Reaction A for this system.

$$2\text{-picoline}-d_3(298K) + Cl \xrightarrow{k_A} 2\text{-picoline}-d_2 + DCl \qquad \text{(Eq. 6.7)}$$

Following 266 nm excitation, 2-picoline-d_3 has a vibrational energy of E_{vib}=38,328 cm^{-1}. Eq. 6.8 describes Reaction B for this system.

$$2\text{-picoline}-d_3(E_{vib}) + Cl \xrightarrow{k_B} 2\text{-picoline}-d_2 + DCl \qquad \text{(Eq. 6.8)}$$

In both cases, photolysis of Cl_2 provides translational energy to the reactants with E_{rel}=2990 cm^{-1}.

In the first set of studies, the appearance of DCl reaction products in the v=0 state was probed. Figure 6.9 shows appearance signals for the J=6 state of DCl for Reaction A (at 298) and Reaction B (with E_{vib}). Products in the (v=0) state with J=2-8 are observed for Reaction A, but none are seen for Reaction B. This result shows that the addition of vibrational energy shuts off the pathway for the v=0 product. In contrast, DCl products in the (v=1) state are observed both for reactants at 298 K and with excess vibrational energy. Transient signals for the J=6 state of DCl (v=1) are shown in Figure 6.10. In the work reported here, DCl product state distributions were measured for the v=0 pathway. A complete characterization of the DCl (v=1) product distributions was not possible due to limited tunability in the IR laser.

Translational temperatures for the DCl (v=0) product from Reaction A at t=1 μs are similar for all the DCl product rotational states measured, T_{trans}(lab)~440±170 K, as shown in Table 6.5 and plotted in Figure 6.11. The rotational distribution of the DCl (v=0) products from Reaction A is T_{rot}=335±30 K as shown in Figure 6.12. The low rotational temperature of DCl products from this reaction suggests a linear C-D-Cl transition geometry. The relatively low translational energy of the products suggests an early transition state.

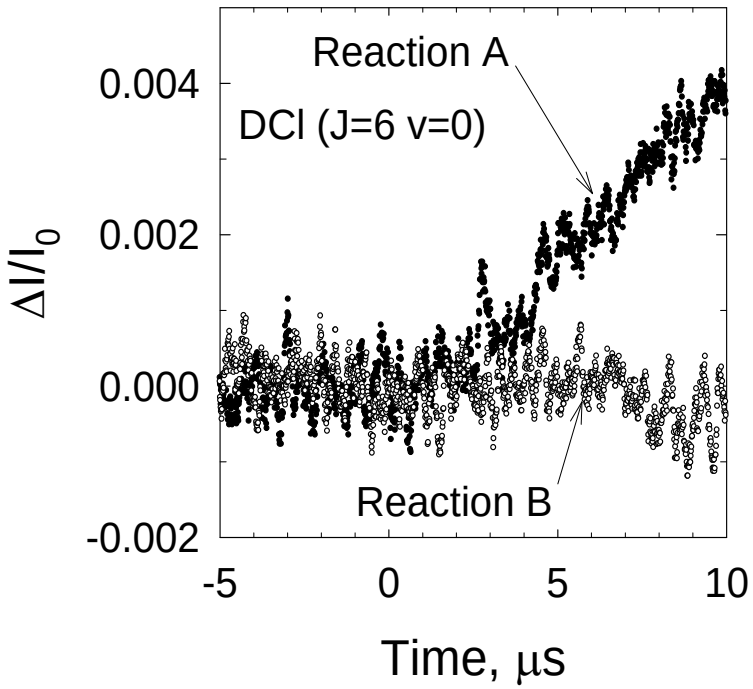

Figure 6.9. Fractional IR absorption of $D^{35}Cl$ (v=0) J=6 coming from reaction of highly vibrationally excited 2-picoline-d_3 (E_{vib}=38,328 cm^{-1}) with Cl (Reaction B, shown in circles) and reaction of room temperature 2-picoline-d_3 with Cl (Reaction A, shown in symbols).

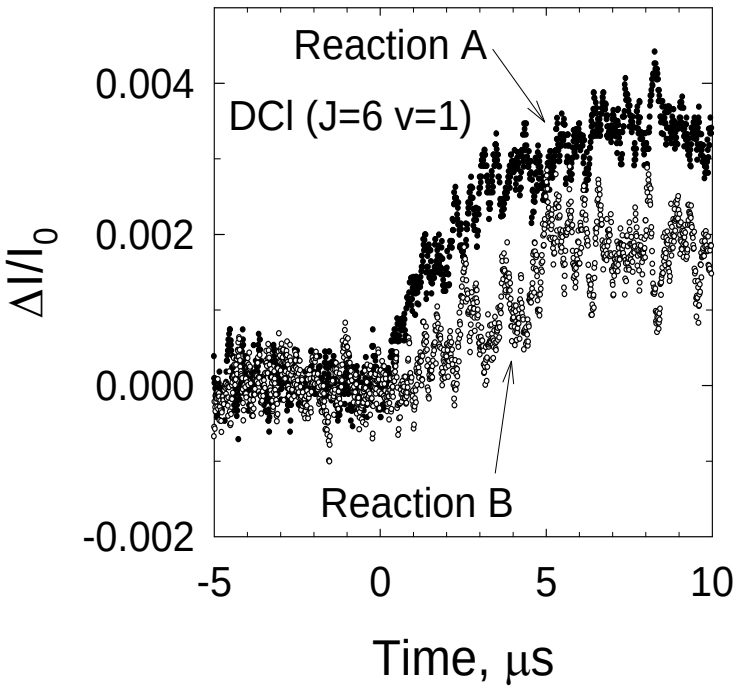

Figure 6.10. Fractional IR absorption of $D^{35}Cl$ (v=1) J=6 coming from reaction of highly vibrationally excited 2-picoline-d_3 (E_{vib}=38,328 cm^{-1}) with Cl (Reaction B, shown in circles) and reaction of room temperature 2-picoline-d_3 with Cl (Reaction A, shown in symbols).

Table 6.5. Doppler-broadened linewidth measurements and lab frame translational temperatures of nascent DCl (v=0) product coming from reaction of room temperature 2-picoline-d_3 molecules and chlorine radicals at 1 μs after the 266 nm and 355 nm UV pulse.

Product State	E_{rot}, cm^{-1}	ν_0, cm^{-1}	$\Delta\nu_{obs}$, cm^{-1} a)	T_{trans}(lab), K b)
$D^{37}Cl$ J=2	32.2539	2118.96	0.0051±0.001	440±170
$D^{37}Cl$ J=5	161.1696	2147.76	0.0054±0.001	480±180
$D^{35}Cl$ J=6	226.2287	2160.07	0.0055±0.001	470±170
$D^{35}Cl$ J=7	301.5287	2168.96	0.0054±0.001	450±170
$D^{35}Cl$ J=8	387.5189	1998.78	0.0049±0.001	370±150

a)The full width at half maximum linewidth at t= 1μs from fitting the t=5, 10, 15, 18 μs transient line profile to a Gaussian function. The linewidth data were plotted as a function of time, and the linewidth at 1 μs was extrapolated. The uncertainty in linewidth is ±0.001 cm^{-1} and is known by measuring a room temperature linewidth of CO_2 to 0.001 cm^{-1} precision.

b The lab frame translational temperature is found using $T_{trans}(lab) = \left(\frac{mc^2}{8k_B \ln 2}\right)\left(\frac{\Delta\nu_{obs}}{\nu_0}\right)^2$ where m is the mass of DCl, c is the speed of light, k_B is Boltzmann's constant, ν_0 is the IR transition frequency and $\Delta\nu_{obs}$ is the nascent Doppler-broadened line width.

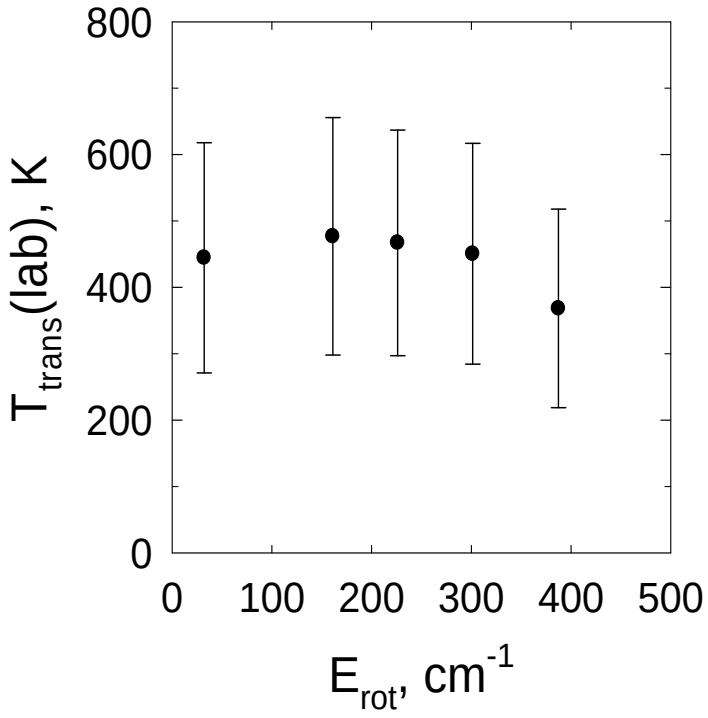

Figure 6.11. Translational partitioning for DCl (v=0) product from Reaction A of 2-picoline-d_3 with Cl.

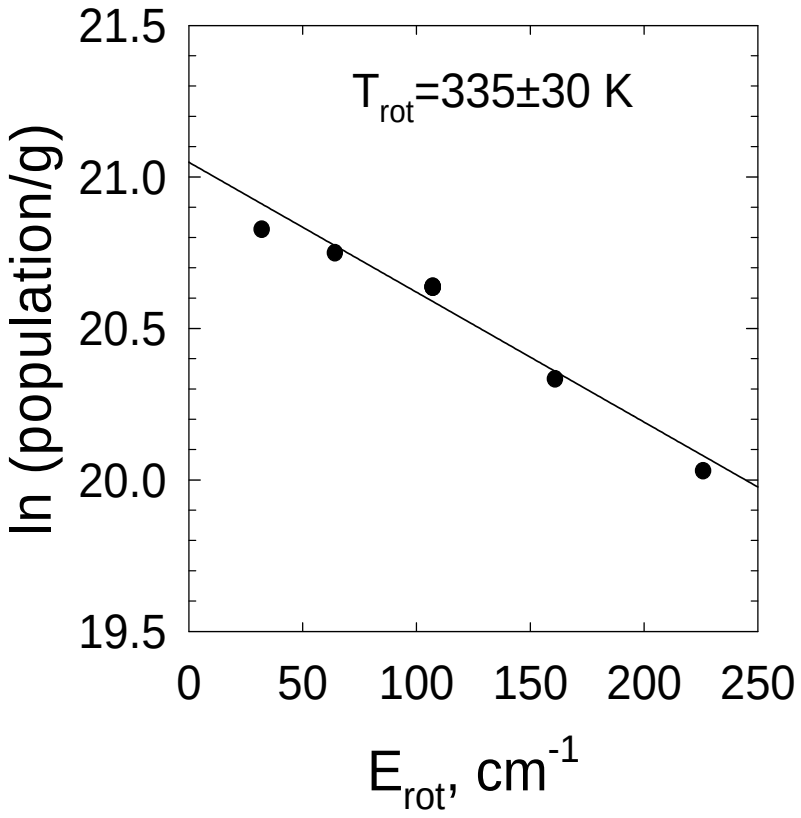

Figure 6.12. Rotational distribution of nascent DCl (v=0) product coming from Reaction A of 2-picoline-d_3 with Cl.

Rate constants for individual product states for Reaction A of 2-picoline-d_3 with Cl are listed in Table 6.6. The integrated rate constant for Reaction A with v=0 products is $k_A=(2.46\pm0.74) \times 10^{-12}$ cm^3 molecule^{-1} s^{-1}. This value is substantially larger than the rate of Reaction A of pyridine-d_5 with Cl, which is $k_A=(1.26\pm0.38) \times 10^{-13}$ cm^3 molecule^{-1} s^{-1} as shown in Section 6.3.3. The average collision rate constant is ~2.5×10^{-9} cm^3 molecule^{-1} s^{-1} for pyridine molecules and Cl (E_{rel}=2990 cm^{-1}) based on the Lennard-Jones collision rate constant in Appendix B and photodissociation of Cl_2. Thus reactions of 2-picoline-d_3 (298 K) with Cl (E_{rel}=2990 cm^{-1}) occur once every 1000 collisions. For pyridine-d_5 (298 K) with Cl (E_{rel}=2990 cm^{-1}), abstraction is much less likely and occurs once every ~19,000 collisions. Given the fact that Reaction A for 2-picoline-d_3 (298 K) is exothermic, it is reasonable that the reaction probability is higher than for the endothermic reaction of pyridine-d_5.

Measurements of the DCl product energies let us determine the internal energy of the 2-picoine-d_3 products. Table 6.7 lists the DCl velocities for individual states and the $\langle v'_{rel} \rangle$ for the reaction products. Figure 6.13 shows the energy diagram for this reaction. The energy difference between reactants and the 2-picoline-d_2 product radical is defined as the energy used for the reaction, E_{used}. Values of E_{used} are listed in Table 6.7 and plotted in Figure 6.14. The negative values of E_{used} indicate that the radical products have more energy than the reactants. As shown in Figure 6.14, the relative translational energy of Cl after photodissociation is enough to overcome the reaction barrier. The 2-picoline-d_2 radicals have an internal energy of ~7300 cm^{-1}, higher than room temperature 2-picoline-d_3. This is further evidence that Reaction A for 2-picoline-d_3 (298 K) with Cl has an early transition state, and

Table 6.6. Reaction rate constant of nascent DCl (v=0) product coming from reaction of room temperature 2-picoline-d_3 with Cl.

Product State	E_{rot}, cm^{-1}	k_A^J, $\times 10^{-14}$ $cm^3 molecule^{-1} s^{-1}$
$D^{37}Cl$ J=2	32.2539	27±8
$D^{37}Cl$ J=5	161.1696	32±10
$D^{35}Cl$ J=6	226.2287	28±8
$D^{35}Cl$ J=7	301.5287	22±7
$D^{35}Cl$ J=8	387.5189	17±5
$k_A = \sum_{All\ J} k_A^J$ [a)]		k_A=246±74

[a)]Integrated rate k_A for DCl (v=0) products is calculated by summing all the predicted rates from rotational distribution.

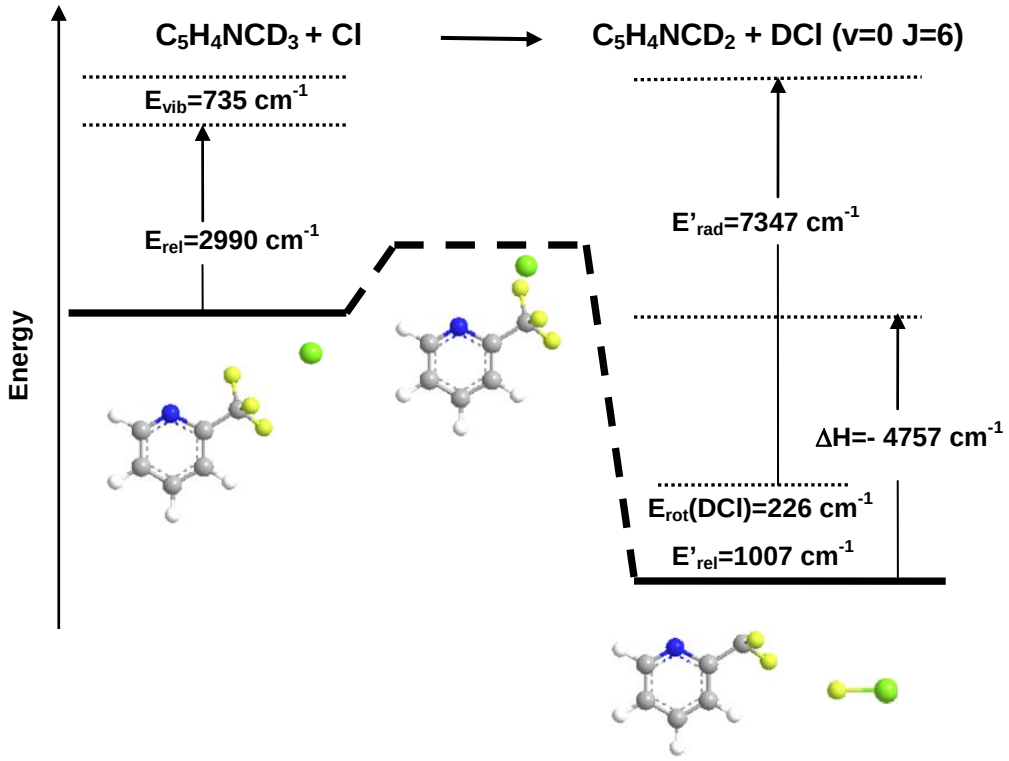

Figure 6.13. The energy schematic of the reaction of room temperature 2-picoline-d_3 with chlorine radical to give $D^{35}Cl$ (v=0) J=6 product. On the reactant side, the relative translational energy between 2-picoline-d_3 and Cl is E_{rel}=2990 cm^{-1}. Room temperature 2-picoline-d_3 molecules have vibrational energy of E_{vib}=735 cm^{-1}. The reaction is an exothermic reaction. On the product side, the reaction enthalpy is ΔH= -4757 cm^{-1}. DCl v=0 J=6 products has relative translational energy of E'_{rel}=1007 cm^{-1} and rotational energy of E_{rot}=226 cm^{-1}. The energy left in 2-picoline-d_2 radicals is E=7347 cm^{-1}.

Table 6.7. Lab frame velocity of DCl product, v_4, from reaction of room temperature 2-picoine-d_3 with chlorine radical, relative velocity of DCl product to 2-picoline-d_2 radical, v'_{rel}, and energy used, E_{used}, for the reaction.

Product State	E_{rot}, cm^{-1}	$\langle v_4 \rangle$, m/s	v'_{rel}, m/s	E_{used}, cm^{-1} [a)]
$D^{37}Cl$ J=2	32.2539	533±104	939±101	-6672±561
$D^{37}Cl$ J=5	161.1696	552±103	955±102	-6508±563
$D^{35}Cl$ J=6	226.2287	561±103	953±101	-6612±593
$D^{35}Cl$ J=7	301.5287	551±102	945±100	-6553±592
$D^{35}Cl$ J=8	387.5189	498±101	903±97	-6639±587

[a)] E_{used} is the energy used for the reaction which is calculated from

$$E_{used} = E_{rel} + E_{vib} + E_{rot,2\text{-picoline}-d3} - \Delta H - E'_{rel} - E'_{rot,DCl} - E_{rot,2\text{-picoline}-d2},$$

where rotational energy of 2-picoline-d_3 molecules and 2-picoline-d_2 radicals, $E_{rot,2\text{-picoline}-d3}$ and $E_{rot,2\text{-picoline}-d2}$, are approximately the same due to a collinear D-atom abstraction reaction mechanism. ΔH is calculated based on the bond dissociation energy of different C-D site in 2-picoline-d_3 molecules. For breaking the C-D bond, ΔH=-4757 cm^{-1}. $E'_{rel} = \frac{\mu' v'^{2}_{rel}}{2}$, where $\mu' = \frac{m_3 m_4}{m_3 + m_4}$. m_3 is the mass of 2-picoline-d_3 radicals. E_{vib}(298K)=735 cm^{-1}.

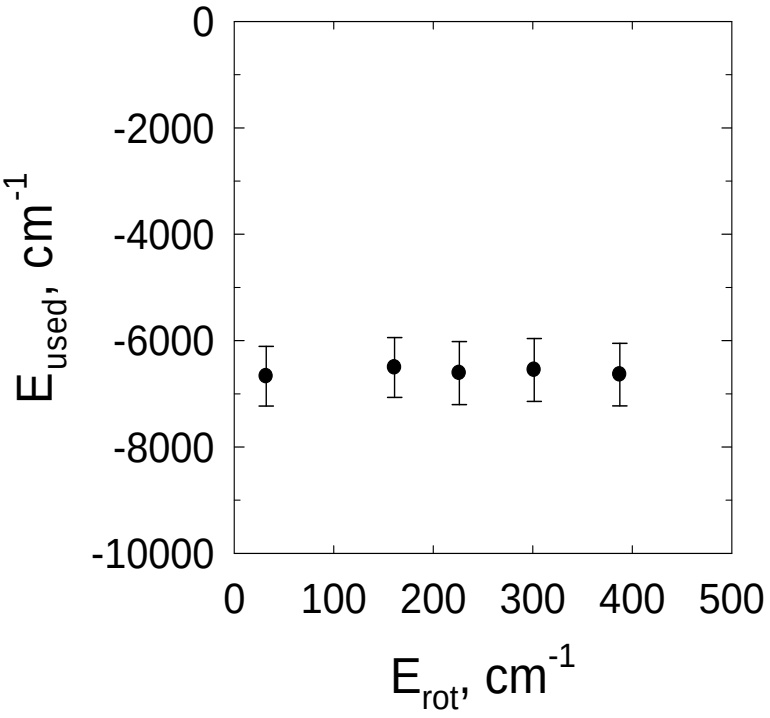

Figure 6.14. The energy used for reaction of room temperature 2-picoline-d_3 with Cl for different DCl (v=0) J states.

that the energy released by the bond-breaking and bond-making process is in the reactant-like product, which is the picoline radical. The fact that v=1 products are observed for this reaction is consistent with these ideas. Early energy release would put translational energy into the D atom along the C-D bond. This type of ballistic D atom would tend to promote vibration in the DCl products. It would be interesting to measure the v=0 and v=1 products as a function of translational energy in the reactants.

It is revealing that vibrational energy enhances D-atom abstraction reactions of pyridine-d_5 but shuts off similar reactions of 2-picoline-d_3, at least for the v=0 products. The C-D stretching modes of 2-picoline-d_3 are similar to the C-D stretches of pyridine-d_5 with $\nu \sim 2200$ cm^{-1}. Figures 4.7 and 6.15 show the average energy content in individual modes when these reactants are vibrationally excited with $E_{vib} \sim 38{,}200$ cm^{-1}. The C-D stretches of pyridine-d_5 have an average energy of $\langle E \rangle \sim 1000$ cm^{-1}, indicating that ~45% of the excited molecules have a C-D stretch in the v=1 state. For 2-picoline-d_3, the C-D stretches have $\langle E \rangle \sim 750$ cm^{-1}, corresponding to ~34% of the excited molecules with one of the C-D stretches in the v=1 state. This relatively small change in population does not account for the observed signal differences in the Reactions B of pyridine-d_5 and 2-picoline-d_3. It is likely that the methyl rotor has a larger effect. When 2-picoline-d_3 is vibrationally excited, the CD_3 methyl rotor goes from a 3-fold hindered rotor[180,181] with a frequency of ν=170 cm^{-1} [182,183] to a free rotor with an average energy of $\langle E \rangle \sim 1500$ cm^{-1}. This is illustrated in Figure 6.16. Reactions that proceed through a linear transition state and lead to the v=0 products are much less likely when 2-picoline-d_3 is vibrationally excited. As a

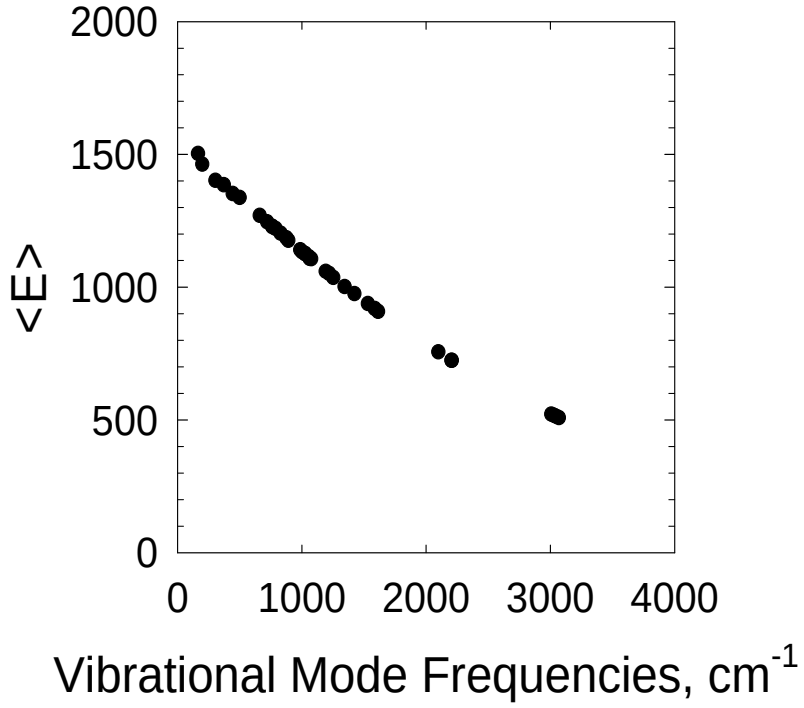

Figure 6.15. Average energy per mode for highly vibrationally excited 2-picoline-d_3 (E_{vib}=38,328 cm^{-1}). Average energy per mode increases as the mode frequency decreases.

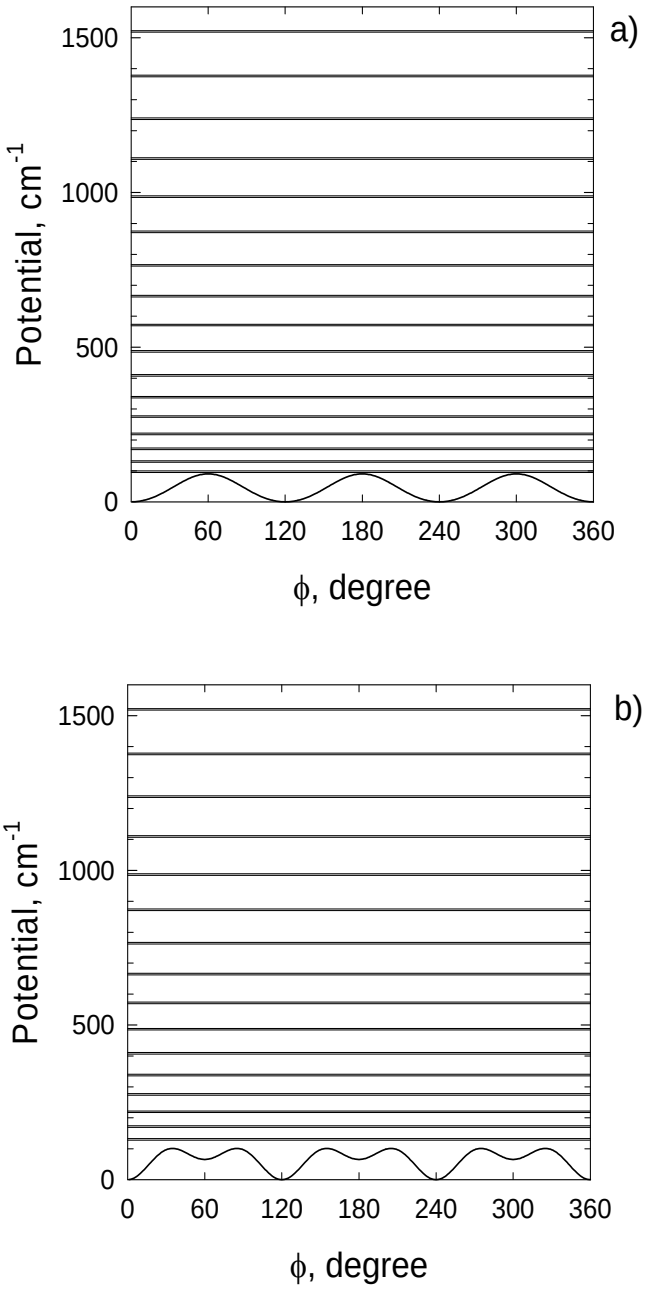

Figure 6.16. The free rotor energy level of CD_3 rotation in 2-picoline-d_3 with the potentials of CD_3 rotation in the (a) ground and (b) first excited C-D stretching vibrational states. In both case the methyl group is a free rotor with $\langle E \rangle \sim 1500$ cm^{-1} when 2-picoline-d_3 has vibrational energy of E_{vib}=38,328 cm^{-1}. Each free rotor energy level has a degeneracy of 2. The free rotor energy levels are estimated by

treating the rotation of CD_3 as a rigid rotor with the rotational constant of CD_3 B_{CD3}=3.7061 cm^{-1}. The value of B_{CD3} is estimated from $B_{CD3} = \frac{B_{CH3}}{\sqrt{2}}$. Here B_{CH3}=5.2412 cm^{-1} and is given by rotational constant of CH_4 along the B axis.[184] The potential of CD_3 rotation is given by $V(\phi) = \frac{1}{2}V_3(1-\cos 3\phi) + \frac{1}{2}V_6(1-\cos 6\phi)$.[181] For ground C-D stretching vibrational state V_3=90.4 cm^{-1} and V_6= -4.1 cm^{-1}.[181] It turns out that the V_6 potential is too small and V(ϕ) appears to be a 3-fold potential. This is shown in Figure a). V_3=65.33 cm^{-1} and V_6= 64.11 cm^{-1} if CD_3 rotation is coupled with one quantum of C-D stretching vibration.[181] This shows a 6-fold potential in Figure b).

free rotor, the CD_3 group has D atoms that are less localized in space and are likely to have higher frequencies for torsional motion than the hindered rotor. The fact that the DCl (v=1) products are observed in reactions of vibrationally excited 2-picoline-d_3 shows that additional pathways open up when the rotor motion of the reactant is excited.

6.4 Conclusion

A rate enhancement of ~90 due to reactant vibrational energy of E_{vib}=38,068 cm^{-1} was observed for the reaction of pyridine-d_5 molecules with chlorine radicals. The rate enhancement for making DCl (v=0) products is attributed to the vibrational excitation of the C-D stretching modes. Analysis of the product energies indicates that the amount of vibrational energy used is very similar to the energy in a single quantum of the C-D stretch. The product energy distributions indication that the reaction proceeds through a linear transition state with an activation barrier that is late with respect to product formation. The reaction products are found to have excess translational energy. These results are consistent with predictions based on Polanyi's rules for atom-diatom reaction, namely that vibrational energy is effective at enhancing late transition states and that products of such reactions have excess translational energy. Late transition states are generally associated with endothermic reactions. The fact that only single quanta of energy are used in these reactions indicates that the reactions occur on a time-scale that is fast relative to IVR in pyridine.

In contrast, the presence of 38,328 cm^{-1} of vibrational energy in 2-picoline-d_3 inhibits D-atom abstraction reactions that produce DCl (v=0). This inhibition is most

likely related to the fact that the CD_3 group in 2-picoline-d_3 goes from a hindered rotor at 298 K to a free rotor when 2-picoline-d_3 is vibrationally excited. The DCl (v=0) product state distributions for the reaction at 298 K show that the 2-picoline-d_2 radical gains large amounts of vibrational energy, even though it already contains more that ~38,000 cm^{-1}. These results show that the transition state is early with respect to the reaction coordinate. Early transition states are generally associated with exothermic reactions. When 2-picoline-d_3 is vibrationally excited, DCl products in the v=1 state have been observed at least for one rotational product state. A rate enhancement of ~5 is observed for the v=1 state due to vibrational excitation. Full product distribution measurement should reveal the nature of the v=1 pathway.

Chapter 7: Conclusion

7.1 Summary and Conclusion

The dynamics of collisional quenching and chemical reactions of highly vibrationally excited molecules has been investigated in this thesis using high resolution transient IR absorption spectroscopy. This approach yields detailed information about the state- and energy-resolved product distributions and absolute rates for energy transfer and reactive collisions of high energy molecules. A number of molecular collision pairs were chosen to investigate the influence of molecular structure, vibrational state density and intermolecular interactions on the exchange of energy in collisions. The role of vibrational energy on chemical reactions was investigated for two types of abstraction reactions. These studies provide insight into the mechanisms that control chemical reactions and collisional energy transfer for molecules in high temperature environments. The results presented in this thesis represent important benchmarks for the development of new theoretical models of high energy molecular collisions.

Four projects are presented in this thesis. In the first, the effect of alkylation was studied. The collisional energy transfer dynamics of highly vibrationally excited 2-ethyl-pyridine (E_{vib}=38,568 cm^{-1}) and 2-propyl-pyridine (E_{vib}=38,867 cm^{-1}) with CO_2 was studied and compare to previous results on pyridine (E_{vib}=37,920 cm^{-1}) and 2-methyl-pyridine (2-picoline) (E_{vib}=38,313 cm^{-1}). Results show that for the strong

collisions, the alkylated donors impart less rotational and translational energy to CO_2 than pyridine does. 2-propyl-pyridine consistently imparts more translational energy in collisions than 2-ethyl-pyridine does and has larger energy transfer rates. Of the alkylated donors, 2-methyl-pyridine and 2-propyl-pyridine have larger probabilities for strong collisional energy transfer than 2-ethyl-pyridine does. The data indicate two competing processes are present: strong collisions are reduced for donors with longer alkyl chains by lowering the average energy per mode but longer alkyl chain have increased flexibility and higher state densities that enhance energy loss via strong collisions.

A second study investigated how preferential hydrogen bonding interactions impacts the energy transfer dynamics. The collisional energy transfer dynamics of highly vibrationally excited pyridine (E_{vib}=37,920 cm^{-1}), pyridine-d_5 (E_{vib}=38,068 cm^{-1}) and pyridine-f_5 (E_{vib}=38,836 cm^{-1}) with H_2O has been investigated. These donor have the same number of vibrational modes and similar internal energies. H_2O (000) molecules are scattered from pyridine-h_5 and pyridine-d_5 with rotational distributions with T_{rot}=890 K. H_2O (000) acquires less rotational energy in collisions with pyridine-f_5. In this case, T_{rot}=550 K. The recoil energy distributions are similar for the three donors with T_{rel}=400-700 K. A torque-inducing mechanism was proposed that involves directed movement of water between σ- and π-hydrogen bonding interactions with the pyridine donors. The experimental results are consistent with this mechanism, and with effects due to the state density energy dependence of the highly excited donor molecules. Differences in vibrational mode frequencies of the hot donor molecules did not explain the experimental results.

A third project uses a new experimental approach to measure state-resolved energy transfer profiles for weak collisions. This enables full energy transfer profiles to be measured directly. The strong and weak collisions of highly vibrationally excited pyrazine (E_{vib}=37,900 cm^{-1}), 2-methyl-pyridine (2-picoline) (E_{vib}=38,313 cm^{-1}) and 2,6-dimethyl-pyridine (2,6-lutidine) (E_{vib}=38,702 cm^{-1}) with HOD was explored to investigate how donor structure influences collisional quenching. Collision rate were directly determined from experimental measurements and compared to Lennard-Jones models. The Lennard-Jones model underestimates the collision rate for highly vibrationally excited azabenzenes with HOD. Hydrogen bonding interactions are not included in the Lennard-Jones model.

The fourth project in this thesis investigated how high level of vibrational energy influences D-atom abstraction reactions. DCl product molecules were probed using high resolution transient IR absorption spectroscopy. The reactions of highly vibrationally excited pyridine-d_5 (E_{vib}=38,068 cm^{-1}) and 2-methyl-d_3-pyridine (2-picoline-d_3) (E_{vib}=38,328 cm^{-1}) with chlorine radicals were studied. A rate enhancement of ~90 was observed for the reaction of highly vibrationally excited pyridine-d_5 and chlorine radical relative to the room temperature reaction. The DCl product was vibrationally and rotationally cold following the reaction but with more relative translational energy, which is consistent with Polanyi's rule for late barrier reactions that occurs through a linear transition state.[173] Energy equal to one quantum of C-D stretch was used in the D-atom abstraction reaction. Reactions of 2-methyl-d_3-pyridine (2-picoline-d_3) (E_{vib}=38,328 cm^{-1}) with chlorine radicals forms vibrationally excited DCl products. DCl (v=0) products were observed for the

reaction at 298 K, but vibrational energy inhibits this product channel. The role of free rotors in abstraction reaction is discussed.

7.2 Future Direction

The studies presented here offer new insights into the dynamics of collisions involving highly excited molecules. The work extends our understanding of how energy content, intermolecular interactions and molecular structure influence energy flow and reactive pathways. The techniques developed in this thesis provide new tools for the next generation of experiments on molecular collisions. These techniques offer exciting new opportunities for measuring full distributions of state-resolved profiles for energy transfer and chemical reactions. The results presented here suggest new areas for future research.

The project on strong collisions of alkylated molecules suggests that molecules with propyl chains (and thus greater structural flexibility) have a greater propensity for strong collisions. There is evidence that ring-forming mechanisms may be active as well in ethylated pyridines. Such process reduces impulsive energy transfer leading to large ΔE values by constraining large amplitude motion. New research should address the role of impulsive collisions due to whip-like motion in high energy molecules by studying the collisional relaxation of other alkyl-substituted donor molecules. Future experiments on strong collisional quenching of highly vibrationally excited 4-n-propyl-pyridine and 2-tert-butyl-pyridine with CO_2 are suggested to answer these questions. In 4-n-propyl-pyridine, the alkyl chain is far away from the nitrogen lone pair, thus making it more difficult to form transient ring-structure. The tert-butyl group in 2-tert-butyl-pyridine is not so flexible as methyl

group in 2-methyl-pyridine due to its bulkiness. The study of 2-tert-butyl-pyridine/CO_2 will provide detailed information about the internal rotor in strong collisional quenching. A number of studies indicate that the low frequency vibrational modes in donor molecules act as gateways that enhance vibrational relaxation.[72,73] It would be interesting to know how the strong collision dynamics are affected by hindering the rotation of the torsional motion in highly vibrationally excited donor molecules.

Preferential hydrogen bonding is another interesting topic. One reason that H_2O has more rotational energy after single collisions with highly vibrationally excited pyridine-h_5 and pyridine-d_5 than pyridine-f_5 may be the 'shuttling' mechanism discussed in Chapter 4. Through this process, hydrogen bonding of H_2O switches between the σ- and the π- bonding sites of the pyridine ring. The idea is that multiple bonding sites act as a catapult and direct H_2O into rotational motion during collisions. The strong collision of highly vibrationally excited pyridine-h_5, pyridine-d_5 and pyridine-f_5 with DCl is suggested, where the hydrogen bonding interactions still exist. Also, it would be interesting to explore the strong collision dynamics of highly vibrationally excited pyridine-h_5, pyridine-d_5 and pyridine-f_5 with CO_2, where such strong hydrogen bonding interaction is not present at all.

The novel way of probing weak collisions of highly vibrationally excited donors with HOD provides insight into the direct collision rate measurements. For all the donor/HOD pairs, the collision rate measurements deviate from Lennard-Jones collision rate. As the donor molecule becomes increasingly methylated, the deviation from Lennard-Jones collision rates with the measured collision rates became larger.

This means the description of Lennard-Jones potential is not an accurate model to describe the intermolecular potential of donor/HOD. Simulations with better potential than the Lennard-Jones models are suggested for those systems. On the other hand, future experiments on the weak collisions of highly vibrationally excited donor molecules with CO_2 are suggested to test if Lennard-Jones intermolecular potential gives a better description on donor/CO_2.

The mode selective vibrational driven reactions of highly vibrationally excited pyridine-d_5 and 2-methyl-d_3-pyridine (2-picoline-d_3) with chlorine radical have been studied to understand the mechanism of the D-atom abstraction reaction. Future studies of reactions of toluene-d_8 ($C_5D_5CD_3$), touluene-d_3 ($C_5H_5CD_3$) and touluene-d_5 ($C_5D_5CH_3$) with chorine radical are suggested to fully understand the mechanism of early barrier and late barrier reaction. Another direction to go is the vibrational energy dependence of rate enhancement. A good candidate to study is the vibrationally excited azulene-d_8 (C_8D_8) with chlorine radical. With 532 nm photon excitation, the average energy in C-D stretch in vibrationally hot azulene-d_8 is about half of the 266 nm photon excitation. It would be interesting to know weather the D-atom abstraction reaction rate enhancement is reduced accordingly.

Appendix A: F-center Laser Single Mode Tuning Procedure

An F-center laser is a solid state laser which uses a Li-doped KCl crystal to achieve laser output. This appendix provides detailed information on the procedure for getting single frequency scanning from the F-center laser. A Kr ion laser with a pump power of < 3.0 W at λ=647 nm output is used to pump crystal #2 (KCl:Li) in the F-center laser. The F-center crystal absorbs λ=647 nm light and fluoresces. The fluorescence is amplified by the F-center laser cavity which is defined by an end mirror and a diffraction grating mirror. Coarse tuning is achieved by scanning the grating mirror. A piezoelectric tunable etalon is used to select a single cavity mode. A pair of CaF_2 galvo plates each with 5 mm thickness is used for fine frequency tuning.

Before installing the crystal into the F-center laser chamber, the laser chamber needs to be tested for vacuum integrity and thermal conductivity. One must pump the laser chamber to a base pressure less than 1 micron and seal it for 24 hours to check the rate of pressure increase. A normal rate of pressure increase is less than 2 micron/hour. Failing to achieve an absolute pressure of at least 1 micron could be a result of too much gas absorbed in the molecular sieves. To address this issue one must open the cryopump chamber to get the molecular sieves out and bake them if necessary. Once the laser chamber can hold vacuum, the ion vacuum pump can be turned on and the thermal conductivity is tested. Fill the dewar above the laser chamber with liquid nitrogen and test the resistor reading on a multimeter. The

resistance is inversely related to the temperature. At room temperature the resistance is about 25 Ω. An adequate thermal connection between the dewar and the crystal assembly requires that the resistance go from 300 Ω (263 K) to 10 kΩ (98 K) within 5 min. Install the F-center crystal in complete darkness at 300K. Process the crystal by exposing it to a 50 W lamp at resistance ~38 Ω (~253 K) for 30 to 45 min. This will allow enough movement of F-centers for lasing.

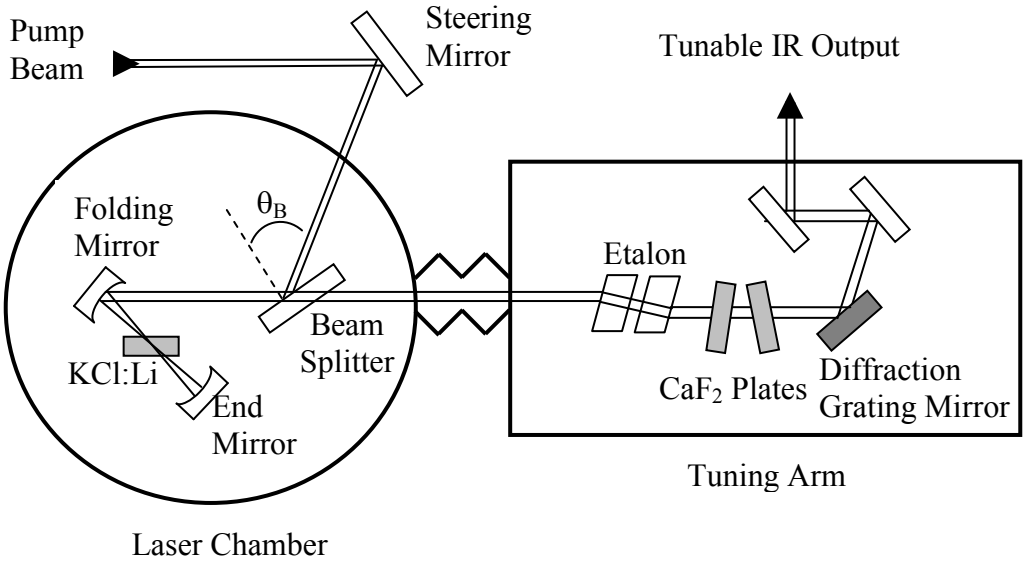

Figure A.1. Burleigh F-center Laser

Once the crystal chamber is thermally stable at liquid nitrogen temperatures, it can be aligned. First, released the tuning arm vacuum and remove the etalon and CaF_2 galvo plates from the tuning arm for ease of alignment. Scan the laser to λ~2.64 μm, which corresponds to the maximum ouput for Crystal #2 using the grating. Then introduce the Kr laser pump beam. One must take care to perfectly send the beam onto a good spot on the KCl:Li crystal by adjusting the steering mirror and focusing the Kr beam on the crystal by adjusting the end mirror. Turning the end mirror

clockwise results in a tighter focus and higher gain. A clear spot from the red tracer beam (~1 mm diameter) will be observed before the etalon position at this point. Check the back reflection of the Kr pump beam from the beam splitter and make sure the back reflection overlaps with the Kr pump beam. In the tuning arm, the back reflection of the tracer beam from the diffraction grating mirror must be aligned to overlap with the input tracer beam. Now, the F-center laser is close to lasing. Put a 1 μs rise time InSb detector at the tunable IR output position to monitor the output from the F-center laser. When the signal is chopped one should be able to see a square wave signal with ~100 mV amplitude. This signal corresponds to the fluorescence of the Li:KCl crystal. Slightly change the diffraction grating mirror knob to optimize the vertical alignment and look for a signal jump on the InSb detector.

Failure of lasing could result from a number of reasons. Most of the time is the alignment. One should carefully check the alignment step by step during troubleshooting.

Another possible reason is the Kr pump power could be below the lasing threshold. The lasing threshold for different crystals varies depending on crystal age and quality. In our F-center laser, the Kr pump power has to be above 1.1 W with 647 nm output to get lasing with crystal #2 and typically 1.7 W pump power was used to find lasing. However, the Kr laser pump beam power can not be too high or one will find rollover, which means the F-center crystal output efficiency decreases with the increase of Kr laser pump power. The way to check for rollover is to increase the Kr pump power and monitor F-center laser power output to find the point where an increased Kr laser power does not yield an increased F-center laser output power. At

the rollover point, the heat accumulated in the crystal is equal to heat dissipated through liquid nitrogen cooling. If the F-center laser is pumped with a higher power than rollover point, the heat will accumulate on crystal and cooling will not be enough to dissipate the heat. This will result in damaging in the F-center crystal. The resistance of the F-center cold finger is another indicator for rollover. If the resistance is below 1 kΩ, this indicates the Kr pump power is beyond rollover. With good cooling, the resistance is between 15 to 20 kΩ (90 K in temperature) with the Kr laser pump power ~2.8 W. Low rollover power indicates the cooling is not good. In this situation it is advisable to warm up the dewar to room temperature and use room temperature dry nitrogen to remove ice at the bottom of the dewar. Break the dewar's vacuum and reapply thermal grease onto cold finger if necessary. Another reason for not observing lasing is the position of InSb detector. During alignment, the output direction of F-center laser will change slightly, thus the position of InSb detector needs to be changed accordingly. Pay attention to the appearance of hairy signal during alignment. If this happens, it is usually the case that the F-center is lasing but the detector is not at the right spot for detection. Other less common problems include poor choice in Kr laser wavelength, closed intracavity iris, or poor choice in the F-center laser crystal position.

Once the lasing is found, the next step is to achieve single mode lasing. Align the etalon with a He-Ne laser (see Burleigh F-center laser manual) and put it into the tuning arm. Perfect alignment will be when one fringe or no fringe shows up for the back reflection which is almost co-linear with the input beam. Use a power meter to watch the output power and mount the etalon with the laser optics set for max power.

This means setting the end mirror fully clockwise. Use a Fabry-Perot etalon (a pair of high reflection flat mirrors with 15 cm distance with free spectral range 0.03 cm^{-1}) to analyze the 10% output signal of laser. Turn on the piezoelectric tunable etalon to suppress all the accessory modes and let the fundamental show up. The procedure for doing this is not difficult. Tune the end mirror counter clockwise while adjusting other optics for power. After many turns the Fabry-Perot signal will simplify and converge on 1-2 modes. With the Fabry-Perot etalon operating at ~800 V and 50 Hz triangle waveform, the spectrum of fundamental should repeat 2 to 3 times during each ramp. If the laser is operating at signal mode, only the fundamental spectrum shows up. The way to suppress accessory modes is by continuing to back off the focusing end mirror.

When single mode lasing is achieved, a Burleigh wavemeter is used to read the output frequency from the laser. Send 100% of the IR beam to the wavemeter and align it to get a stable reading. Note that even though the output power is high, the reading on the wavemeter will not show up or show up an unstable reading if the wavemeter is not perfectly aligned. One way to check the alignment of wavemeter is to check the fringe given by the photodiode detector in the wavemeter. A homogeneous fringe signal will be observed if the wavemeter is properly aligned and the F-center laser has single mode output.

Once the laser has single mode output, the galvo plates need to be put into laser tuning arm to get further tunability. The galvo plates are a pair of CaF_2 plates with 5 mm thickness placed at the Brewster angle from the laser beam. The rotation of galvo plates requires a triangle wave input (usually a 0.0625 Hz frequency, 1 V

amplitude) of voltage to the galvo driver. By rotating the CaF_2 plate pair, the length of laser cavity is changed, and the single mode output frequency changes. Lock the piezoelectric etalon to a cavity mode and start to rotate the galvo plates. The lock should hold and the laser will start scanning. Adjust the amplitude of etalon servo gain to match the etalon scan with the movement of the galvo plates. Watch the wavemeter and the Fabry-Perot signals at the same time, they should change simultaneously if the single mode scan is achieved. This is called an open-loop feed-forward control as been described by Kasper *et al*.[185]

The F-center laser transient IR absorption spectrometer probes at ~2.7 μm with a 0.0005 cm^{-1} resolution. At λ=~2.7 μm, numerous molecules have absorption. For instance, H_2O (001←000), HOD (001←000), and CO_2 (10^01←00^00) transitions are within the tuning range of the F-center Laser using Crystal #2. Several hot bands of H_2O such as (011←010) are also here. The different probing range enabled us to study different molecules to investigate collision dynamics.

Appendix B: Calculating the Lennard-Jones Collision Rate Constants

The collision rate constants for donor/bath were determined using a Lennard-Jones(LJ) potential[186] given by

$$k_{LJ} = \left(\frac{8k_B T}{\pi\mu}\right)^{\frac{1}{2}} \Omega^{(2,2)*} \pi\sigma^2 \qquad \text{(Eq. B.1)}$$

The collision integral $\Omega^{(2,2)*}$ is a function of the reduced temperature T*:

$$\Omega^{(2,2)*} = 1.16145(T^*)^{-0.14874} + 0.52487\exp\{-0.7732T^*\} + 2.16178\exp\{-2.43787T^*\} \qquad \text{(Eq. B.2)}$$

$$T^* = \frac{k_B T}{\varepsilon} \qquad \text{(Eq. B.3)}$$

The Lennard-Jones parameters σ and ε/k_B for the mixed donor/bath systems are obtained using established combining rules.[186]

$$\sigma = \frac{1}{2}(\sigma_{donor} + \sigma_{bath}) \qquad \text{(Eq. B.4)}$$

$$(\varepsilon/k_B) = ((\varepsilon/k_B)_{donor}\,(\varepsilon/k_B)_{bath})^{\frac{1}{2}} \qquad \text{(Eq. B.5)}$$

For donor/CO_2, σ_{CO_2}=4.50 Å, $(\varepsilon/k_B)_{CO_2}$=190.0 K.[151] Parameters for pyridine and 2MP come from critical temperatures T_c and critical volume V_c.[187] Lennard Jones parameters values for 2EP and 2PP were not found in the literature and were estimated based pyridine and 2MP values and trends in benzene series and cyclopentane series[188] as shown in Figure B.1. Lennard-Jones parameters and rate constants are listed in Table B.1.

For donor/H_2O, σ_{H_2O}=2.65 Å, $(\varepsilon/k_B)_{H_2O}$=380.0 K.[151] Lennard-Jones collision rate constants are shown in Table B.2. Lennard-Jones collision rate constants for donor/HOD are listed in Table B.3. Values of σ_{HOD} and $(\varepsilon/k_B)_{HOD}$ are the same as those for H_2O. Only mass differences are considered in the calculation.

Table B.1. Lennard-Jones rate constants and parameters for pyridine series with CO_2.

Donor	σ_{donor}, Å[a)]	σ_{DB}, Å[b)]	$(\varepsilon/k_B)_{donor}$, K	$(\varepsilon/k_B)_{DB}$, K[d)]	k_{LJ},10^{-10}cm^3 s^{-1} molecule^{-1}
Pyr	5.23[a)]	4.87	465.0[c)]	297.2	5.58
2MP	5.58[a)]	5.04	465.7[c)]	297.5	5.86
2EP[e)]	6.06[e)]	5.28	503.5[e)]	309.3	6.39
2PP[e)]	6.40[e)]	5.45	523.5[e)]	315.4	6.76

[a)] Calculated using critical volume: $\sigma^3 \approx \frac{9}{8}\frac{v_c}{\pi N_A}$,[187] where V_c is listed in Table B.4 and N_A is Avogadro's number.

[b)] LJ parameter σ_{DB} during the donor/bath collision.

[c)] Calculated using critical temperature: $\varepsilon \approx \frac{3}{4}T_c$,[187] where T_c is listed in Table B.4.

[d)] LJ parameter ε_{DB} during the donor/bath collision.

[e)] σ_{donor} and $(\varepsilon/k_B)_{donor}$ for 2EP and 2PP were calculated based on data in Figure B.1 and values listed in Table B.1.

Table B.2. Lennard-Jones rate constants and parameters for pyridine series with H_2O.

Donor	σ_{donor}, Å[a]	σ_{DB}, Å[b]	$(\varepsilon/k_B)_{donor}$, K	$(\varepsilon/k_B)_{DB}$, K[d]	k_{LJ}, 10^{-10}cm^3 s^{-1} molecule^{-1}
Pyridine-h_5	5.25[a]	3.95	465.0[c]	420.4	6.15
Pyridine-d_5[e]	5.25[e]	3.95	465.0[e]	420.4	6.12
Pyridine-f_5[f]	5.70[f]	4.18	432.2[f]	405.2	6.44

[a] Calculated using critical volume: $\sigma^3 \approx \frac{9}{8}\frac{V_c}{\pi N_A}$,[187] where V_c is listed in Table B.4 and N_A is Avogadro's number.

[b] LJ parameter σ_{DB} during the donor/bath collision.

[c] Calculated using critical temperature: $\varepsilon \approx \frac{3}{4}T_c$,[187] where T_c is listed in Table B.4.

[d] LJ parameter ε_{DB} during the donor/bath collision.

[e] σ_{donor} and $(\varepsilon/k_B)_{donor}$ values are the same for pyridine-h_5 and pyridine-d_5.

[f] σ_{donor} and $(\varepsilon/k_B)_{donor}$ for pyridine-f_5 were calculated based on data in Figure B.2. As shown in Figure B.2, critical temperatures, T_c, and critical volumes, V_c, for pyridine-f_5 were determined from values for C_6H_6, C_6H_5F, $C_6H_2F_4$, C_6HF_5, C_6F_6, and pyridine-h_5.[188]

Table B.3. Lennard-Jones rate constants and parameters for pyridine series with HOD.

Donor	σ_{donor}, Å[a]	σ_{DB}, Å[b]	$(\varepsilon/k_B)_{donor}$, K[c]	$(\varepsilon/k_B)_{DB}$, K[d]	k_{LJ}, 10^{-10}cm^3 s^{-1} molecule^{-1}
Pyrazine	5.35	4.00	435.5	406.8	6.19
2-Picoline	5.57	4.11	465.8	420.7	6.44
2,6-Lutidine	5.88	4.27	467.9	421.7	6.86

[a] Calculated using critical volume: $\sigma^3 \approx \frac{9}{8}\frac{v_c}{\pi N}$,[187] where V_c is listed in Table B.4 and N_A is Avogadro's number.

[b] LJ parameter σ_{DB} during the donor/bath collision.

[c] Calculated using critical temperature: $\varepsilon \approx \frac{3}{4}T_c$,[187] where T_c is listed in Table B.4.

[d] LJ parameter ε_{DB} during the donor/bath collision.

Table B.4. Critical temperatures T_c and critical volume V_c of molecules.

Donor	T_c, K [a)]	V_c, cm^3 [a)]
Cyclopentane (C_5H_{10})	511.7	260
Methyl-Cyclopentane (C_6H_{12})	532.73	319
Ethyl-Cyclopentane (C_7H_{14})	569.5	375
Benzene (C_6H_6)	562.16	259
Toluene(C_7H_8)	591.79	316
Ethyl-benzene (C_8H_{10})	617.2	374
Propyl-benzene (C_9H_{12})	638.32	440
Butyl-benzene ($C_{10}H_{14}$)	660.5	497
Pyridine (C_5H_5N)	620	243
2-methyl-pyridine (C_6H_7N)	621	292
Fluoro-benzene (C_6H_5F)	560.09	269
1,2,3,4-Tereafluoro-benzene ($C_6H_2F_4$)	550.83	313
Pentafluoro-benzene (C_6HF_5)	530.97	324
Hexafluoro-benzene (C_6F_6)	516.73	335
2,6-dimethyl-pyridine (C_7H_9N)	623.8	343 [b)]

[a)] Data are from CRC Handbook of Chemistry and Physics.[188] See Section 6 in Ref[188].

[b)] V_c for 2,6-dimethyl-pyridine is estimated from extrapolation of V_c values for pyridine and 2-methyl-pyridine.

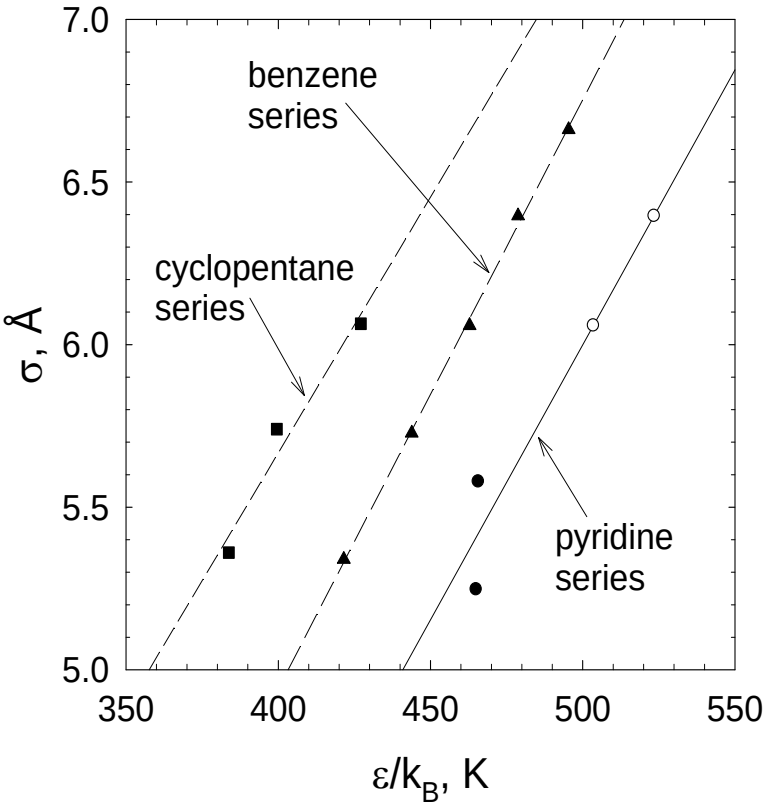

Figure B.1. The linear relationship between σ and ε/k_B for two series of alkylated cyclic molecules (benzene and cyclopentane) is used to estimate parameters for alkylated pyridines with CO_2. Triangles (▲) are for the benzene series: (in order from lower to higher ε/k_B) benzene, methylbenzene, ethylbenzene, propylbenzene and butylbenzene[188]. Squares (■) are for the cyclopentane series: (in order from lower to higher ε/k_B) cyclopentane, methyl-cyclopentane and ethyl-cyclopentane[188].

Circles (●) are for the pyridine series, with open circles for estimated values for 2EP and 2PP. The pyridine series is assumed to have a similar linear relationship as the other ring molecules and a slope that is the average of the benzene and cyclopentane values. σ values for 2EP and 2PP are assumed to be the same as for the ring molecules with the same alkyl chains.

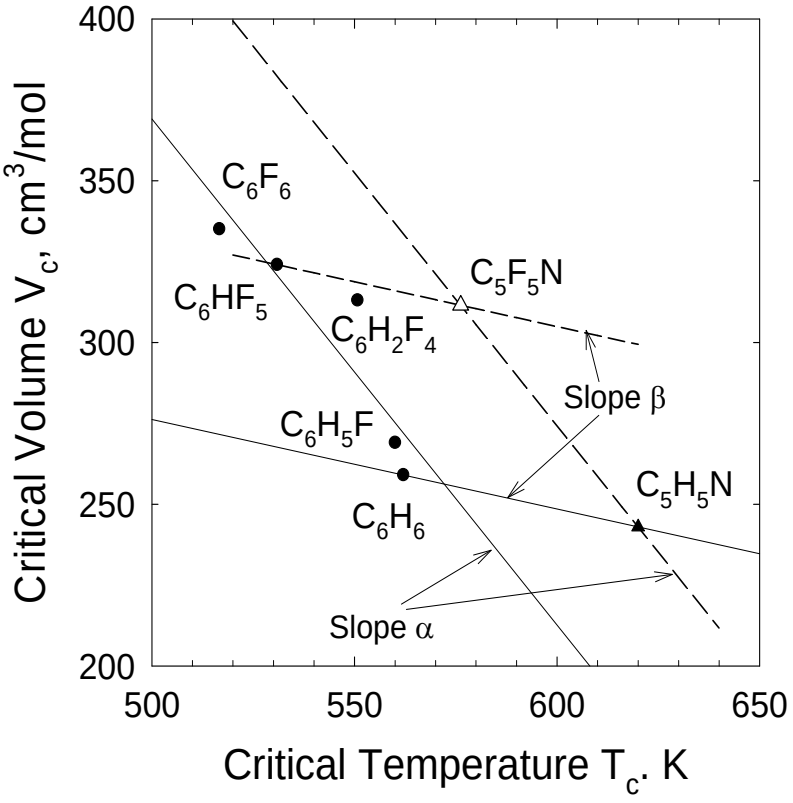

Figure B.2. Critical temperatures, T_c, and critical volumes, V_c, for pyridine-f_5 were determined from values for C_6H_6, C_6H_5F, $C_6H_2F_4$, C_6HF_5, C_6F_6, and C_5H_5N.[188] Circles (•) are values for the benzene and fluoro-benzene series, with a linear fit that has slope α as shown. A solid triangle (▲) is for C_5H_5N. Second linear fit through C_6H_6 and C_5H_5N has slope β as shown. The open triangle shows the estimated values for pyridine-f_5 (C_5F_5N). The slopes α and β were used to estimate the critical values for C_5F_5N.

Appendix C: Calculating the Energy Transfer Rates for H_2O and HOD

The H_2O and HOD rate calculations are described below for the process

Pyrazine (E_{vib}) + H_2O or HOD

$$\xrightarrow{k_2^J} \text{Pyrazine } (E_{vib}-\Delta E) + H_2O \text{ or HOD } (000, J_{Ka,Kc}, V) \qquad \text{(Eq. C.1)}$$

where k_2^J stands for the rate constant for appearance of H_2O or HOD (000, $J_{Ka,Kc}$, V) states. For H_2O experiments, at short times, the concentration of highly vibrationally excited pyrazine molecules [pyrazine^E] and bulk H_2O concentration [H_2O] can be considered constant. So the initial concentration [pyrazine^E]$_0$ and [H_2O]$_0$ are used. The time dependent population change of a single rotational state is

$$\frac{d[H_2O^J]}{dt} = k_2^J[H_2O]_0[\text{pyrazine}^E]_0 \qquad \text{(Eq. C.2)}$$

Here [H_2O^J] is the concentration of a rotational state of H_2O which is not initially populated at room temperature but is populated due to collisions with highly vibrationally excited pyrazine molecules. The rate constant is defined by

$$k_2^J = \frac{[H_2O^J]}{[H_2O]_0[\text{pyrazine}^E]_0 \Delta t} \qquad \text{(Eq. C.3)}$$

in units of $cm^{-3}molecule^{-1}sec^{-1}$. Δt is 1 μs.

To calculate $[H_2O^J]$,

$$[H_2O^J] = \frac{n}{V} = \frac{P_{H_2O^J}}{RT} \qquad \text{(Eq. C.4)}$$

where n is the number of moles, V is the volume, $P_{H_2O^J}$ is the transient "pressure" of H_2O in the state J, R is the gas constant and T is room temperature, 298 K.

The Beer-Lambert Law gives

$$P_{H_2O^J} = \frac{-\ln(I_t/I_0)}{\alpha_J \ell} \qquad \text{(Eq. C.5)}$$

where I_t/I_0 is the transmittance T(t) at 1 μs, ℓ is the path length in cm and α_J is the state-specific absorption coefficient.

The state specific absorption coefficient α_J is defined as

$$\alpha_J = \frac{S_{HITRAN} f_0 N}{f_V f_J} \qquad \text{(Eq. C.6)}$$

where S_{HITRAN} is the line strength reported in HITRAN database[81], f_0 scales for the Doppler-broadened linewidth, N is the number density per Torr at the temperature of S_{HITRAN}, and f_V and f_J are the fractional populations in the specific vibrational and rotational states probed, respectively.

$$f_0 = \frac{2\sqrt{\ln 2/\pi}}{\Delta\nu_{dop}} \qquad \text{(Eq. C.7)}$$

$\Delta\nu_{dop}$ is the J-specific FWHM linewidth at temperature of S_{HITRAN}. For a transient measurement, $\Delta\nu_{obs}$ is used instead. Other useful relationships include

$$N = \frac{n}{PV} = \frac{1}{RT} = 3.24\times10^{16} \text{ molecule cm}^{-3} \text{ torr}^{-1} \qquad \text{(Eq. C.8)}$$

$$f_V = \frac{g_V e^{-\frac{E_{vib}}{k_B T}}}{Q_{vib}} \text{ and } f_J = \frac{g_{NS} g_J e^{-\frac{E_{rot}}{k_B T}}}{Q_{rot}} \qquad \text{(Eq. C.9)}$$

where g_V, g_{NS} and g_J are the degeneracies for vibration, nuclear spin and rotation for H_2O molecules, respectively. $g_V = 1$, $g_{NS} = 3$ for K_a+K_c = odd, $g_{NS} = 1$ for K_a+K_c = even and $g_J = 2J+1$. k_B is Boltzmann constant. E_{vib} and E_{rot} are vibrational and rotational energy level and Q_{vib} and Q_{rot} are vibrational and rotational partition functions.

$$Q_{vib} = \frac{1}{\prod_i (1 - e^{-E_i/k_B T})^{g_i}} \qquad \text{(Eq. C.10)}$$

where E_i is the energy of the i^{th} vibrational mode, and g_i is the degeneracy of the i^{th} vibrational mode. For H_2O molecules, ν_1 = 3657.1 cm^{-1}, ν_2 = 1594.8 cm^{-1}, ν_3 = 3755.8 cm^{-1}, and all three vibrations are singly degenerate. Q_{vib} =1.007 for H_2O at 298 K.

$$Q_{rot} = \frac{S}{\sigma}\sqrt{\frac{\pi(k_B T)^3}{ABC}} \qquad \text{(Eq. C.11)}$$

where σ is the molecular symmetry number. A, B and C are the moments of inertia along the a, b and c axis. S is the nuclear spin factor, $S = \Pi(2I_i + 1)$, where I_i is the nuclear spin of atom i. I_i = 0.5 for H, I_i = 1 for D and I_i = 0 for ^{16}O. For H_2O, σ = 2, A = 27.87 cm^{-1}, B = 14.52 cm^{-1}, C = 9.31 cm^{-1} and S = 4. For H_2O, Q_{rot} = 170.38 at T = 296 K.

$[H_2O]_0$ is determined by the baratron pressure reading and converted to spectroscopic pressure in molecules cm^{-3}. $[pyrazine^E]_0$ is calculated using Eq. C.12.

$$[pyrazine^E]_0 = \frac{UV_{abs}}{E_{266}\,\pi\, r^2\, \ell} \qquad \text{(Eq. C.12)}$$

where UV_{abs} is the amount of UV light absorbed in mJ, E_{266} is the photon energy at 266 nm, *r* is the optical radius of UV light and ℓ is the cell length.

For HOD molecules, ν_1 = 2726.7 cm^{-1}, ν_2 = 1402.2 cm^{-1}, ν_3 = 3707.5 cm^{-1}, and all three vibrations are singly degenerate. Q_{vib} = 1.0011, g_{NS} = 6, S = 6 and σ = 1. For HOD, Q_{rot} = 849.88 at T = 296 K. S_{HITRAN} needs to be divided by the isotopic abundance which is 0.031% to get the pure HOD HITRAN line strength[81]. An equilibrium 1:1 mixture of

H_2O and D_2O consists of 49.4% HOD.[160] $[HOD]_0$ is determined by 49.4% of the pressure reading and converted to spectroscopic pressure in molecules cm^{-3}.

Appendix D: Fortran Program for Calculating Energy Transfer Probability for Pyrazine/HOD

The Fortran files used for calculating the energy transfer probability function P(ΔE) for pyrazine/HOD are listed below. The file 'water_gen_pyrazine.f90' is used to calculate the energy transfer probability function, $P_J(\Delta E)$, for each of the HOD $J_{Kc,Kc}$ state. For this example, the average relative translational temperature for scattered HOD (000) is $\langle T_{trans,rel} \rangle$=635 K, and the initial HOD energy is E_i=540 cm^{-1}. The initial HOD energy, E_i, is determined by a 298 K distribution, where room temperature HOD translational and rotational energies are summed to be 540 cm^{-1}.

water_gen_pyrazine.f90

```
MODULE global_dim
        IMPLICIT NONE
        SAVE
        INTEGER, PARAMETER :: record_num = 1000
        REAL, PARAMETER :: t = 635
        CHARACTER(LEN=9), DIMENSION(1001) :: InputJ
        REAL, DIMENSION(1001) :: InputErotf,k2jcal
        INTEGER :: k

END MODULE global_dim

PROGRAM WaterGeneral
        USE global_dim
        IMPLICIT NONE

        CHARACTER(LEN=20) :: MyOutputFile
        REAL :: Erotf,Enot,k2j
        INTEGER :: j

        DO k=1,record_num
        CALL SetupVariables(Erotf,Enot,k2j,MyOutputFile)
        CALL RunCalculations(Erotf,Enot,k2j,MyOutputFile)
```

```
        END DO

END PROGRAM WaterGeneral

SUBROUTINE SetupVariables(Erotf,Enot,k2j,MyOutputFile)
        USE global_dim
        IMPLICIT NONE


        !Dim variables
        INTEGER :: i,n,open_error,io_error, EnotInt
        CHARACTER(LEN=20) :: MyInputFile
        CHARACTER(LEN=9) :: MyJKaKc
        CHARACTER(LEN=20), INTENT(OUT) :: MyOutputFile
        REAL, INTENT(OUT) :: Erotf,Enot,k2j
        REAL :: OldEnot

        PRINT *,"> Starting Setup subroutine"

        !Get inputs from keyboard
        !PRINT *,"Please enter the name of the input file:"
        !READ '(A)',MyInputFile
        MyInputFile = "allstate.txt"

        !PRINT *,"Enter JKaKc:"
        !READ '(F5.0)',MyJKaKc

        !MyOutputFile = MyJKaKc".out"

        !Open input file
        PRINT *,"> Opening input file connection"
        OPEN(UNIT=10, FILE=MyInputFile, STATUS="OLD", &
                ACTION="READ", IOSTAT=open_error)

        !Catch errors
        IF (open_error /= 0) THEN
                PRINT *,"Error: could not open files."
                STOP
        END IF

        !Fill input arrays
        PRINT *,"> Filling input arrays"
        DO i=1,record_num
                READ (10,200,IOSTAT=io_error)InputJ(i),InputErotf(i),k2jcal(i)
200             FORMAT(A9,T10,F7.3,T24,F18.6)
                IF (io_error < 0) EXIT
        END DO

        !n will equal the number of records read
        n = i - 1

        !Find the Erotf for the JKaKc we want to use
        PRINT *,"> Finding Erotf for JKaKc"
                        Erotf = InputErotf(k)
                        k2j = k2jcal(k)
                        MyJKaKc = InputJ(k)
```

MyOutputFile = MyJKaKc

```
        !Calculate to get Enot
        PRINT *,"> Performing setup calculations"
        Enot = 450 + (Erotf - 1006.116)
        Enot = Enot / 10
        EnotInt = Int(Enot)
        EnotInt = EnotInt * 10
        Enot = Real(EnotInt)
        OldEnot = Enot
        Enot = Enot * 1.986e-23

        !Use the correct calculation
        PRINT *,"> Selecting correct calculation and using it"


        PRINT *,"***********************"
        PRINT *,"* USING THESE VALUES: *"
        PRINT *,"InputJ(j):"
        PRINT *,InputJ(k)
        PRINT *,"MyJKaKc:"
        PRINT *,MyJKaKc
        PRINT *,"Erotf:"
        PRINT *,Erotf
        PRINT *,"Enot:"
        PRINT *,OldEnot
        PRINT *,"k2j:"
        PRINT *,k2j
        PRINT *,"***********************"


        !Perform calculation on Erotf
        Erotf = Erotf * 1.986e-23

        !Clean up file connection
        CLOSE(10)

        PRINT *,"> Returning arguments to main program"

END SUBROUTINE SetupVariables

SUBROUTINE RunCalculations(Erotf,Enot,k2j,MyOutputFile)
        USE global_dim
        IMPLICIT NONE


        !Dim variables
        CHARACTER(LEN=20), INTENT(IN) :: MyOutputFile
        REAL, INTENT(IN) :: Erotf,Enot,k2j
        INTEGER :: i,n,open_error
        REAL :: NewK,klj,dErot,dE,mu,gi,pi,p,gi2,d,gf,gf2,Eroti,Step

        PRINT *,"> Starting Calculations subroutine"

        !Open the filename passed in for writing
```

```
        PRINT *,"> Opening connection to output file"
        OPEN(UNIT=20, FILE=MyOutputFile, STATUS="NEW", &
                ACTION="WRITE", IOSTAT=open_error)

        !Catch errors
        IF (open_error /= 0) THEN
                PRINT *,"Error: could not open files."
                STOP
        END IF

        !Do initial calculations
        PRINT *,"> Beginning calculations"
        NewK = 1.38066e-23
        mu = (80*19)/(80+19)*1.66056e-27
        pi = 3.14159
        gi2 = 8*NewK*298/(pi*mu)
        gi = SQRT(gi2)
        Eroti = 300*1.986e-23
        klj = 6.19e-10
        Step = 10*1.986e-23

        !Do a loop - calculate at each iteration and write iteration to file
        PRINT *,"> Starting file-writing loop"
        n = 1000
        DO i=2,1000
                dE = Enot+Step*(i-1)
                dErot = Erotf-Eroti
                gf2 = 2/mu*(dE-dErot)+gi2
                gf = SQRT(gf2)
                p = 4*pi/mu*k2j/klj*gf*(mu/(2*pi*NewK*t))**1.5*EXP(-mu*gf2/(2*NewK*t))
                d = dE/1.986e-23
                p = p*1.986e-23
                IF (p .LT. 0) THEN
                        p = 0.0
                END IF

                WRITE(20,300)p,d
300             FORMAT(2x,e9.4,2x,f7.1)
        END DO

        PRINT *,"> Finished file writing; closing file connection"

        !Clean up the file connection
        CLOSE(10)

        PRINT *,"> PROGRAM FINISHED!"

END SUBROUTINE RunCalculations
```

The program ‘water_gen_pyrazine.f90’ reads the file ‘Allstate.txt’ under the same folder and runs the calculation. The ‘Allstate.txt’ file is listed below. The first column

provides the output file name for each $J_{Ka,Kc}$ state. The second column is the corresponding rotational energy and the third column is the bimolecular energy transfer rate constant for that state. Each row will give an output file, which contains the energy transfer distribution function for that $J_{Ka,Kc}$ state. The 'Allstate.txt' file includes all HOD (000) states listed in HITRAN database[81].

Allstate.txt

000.out	0	0.000000000003961	(Line 1)
101.out	15.5082	0.000000000011298	(Line 2)
… …			
… …			
18018.out	2296.384	0.000000000000081	(Line Final)

The program 'add_all_files.f90' reads all the $P_J(\Delta E)$ output files and adds the $P_J(\Delta E)$ values according to an energy increment. The program 'add_all_files.f90' reads an input file named 'All.txt' under the same folder to run the calculation, as described later.

add_all_files.f90

```
MODULE global_dim
        IMPLICIT NONE
        SAVE
        INTEGER, PARAMETER :: record_num = 10000
        REAL, DIMENSION(10001) :: File1First,File1Second,File2First,File2Second

END MODULE global_dim

PROGRAM AddTwoFiles
        USE global_dim
        IMPLICIT NONE

        CHARACTER (LEN=9), DIMENSION(10001) :: file1,file2,sum12
        CHARACTER(LEN=20) ::  MyInputFile
        INTEGER :: i,j,open_error,io_error
        CHARACTER(LEN=9) :: f1,f2,sum
```

```
        MyInputFile = "all.txt"

        !Open input file
        PRINT *,"> Opening input file connection"
        OPEN(UNIT=10, FILE=MyInputFile, STATUS="OLD", &
                ACTION="READ", IOSTAT=open_error)



        !Catch errors
        IF (open_error /= 0) THEN
                PRINT *,"Error: could not open files."
                STOP
        END IF

        PRINT *,"***********************"
        PRINT *,"* USING THESE VALUES: *"
        PRINT *,"inputfile:"
        PRINT *, MyInputFile
        PRINT *,"***********************"



        !Fill input arrays
        PRINT *,"> Filling input arrays"
        DO i=1,record_num
                READ (10,200,IOSTAT=io_error)file1(i),file2(i),sum12(i)
200             FORMAT(A9,T11,A9,T22,A9)

        END DO

        Do j=1,181
        !Do file work
        f1=file1(j)
        f2=file2(j)
        sum=sum12(j)
        CALL RunCalculation(f1,f2,sum)
        End Do

END PROGRAM AddTwoFiles

SUBROUTINE RunCalculation(f1,f2,sum)
        USE global_dim
        IMPLICIT NONE

        INTEGER :: Count1,Count2,i2,i3,i4,i5,n1,n2,open_error,io_stat
        CHARACTER(LEN=20) :: file_name1,file_name2,output_file,found
        REAL :: first_one,first_two,second_one,second_two,added_num
        CHARACTER(LEN=9) :: f1,f2,sum


        file_name1=f1
        file_name2=f2
        output_file=sum
```

```
        !Open files
        OPEN(UNIT=10, FILE=file_name1, STATUS="OLD", &
                ACTION="READ", IOSTAT=open_error)

        OPEN(UNIT=20, FILE=file_name2, STATUS="OLD", &
                ACTION="READ", IOSTAT=open_error)

        OPEN(UNIT=30, FILE=output_file, STATUS="NEW", &
                ACTION="WRITE", IOSTAT=open_error)

        !Catch errors
        IF (open_error /= 0) THEN
                PRINT *,"Error: could not open files."
                STOP
        END IF

        PRINT *,"> Finished opening files."

        !Fill each array separately

        PRINT *,"> Filling file arrays."

        DO Count1=1,record_num
                READ (10,200,IOSTAT=io_stat)File1First(Count1),File1Second(Count1)
200             FORMAT(2x,e9.4,2x,f7.1)
                IF (io_stat < 0) EXIT
        END DO

        DO Count2=1,record_num
                READ (20,200,IOSTAT=io_stat)File2First(Count2),File2Second(Count2)
                IF (io_stat < 0) EXIT
        END DO

        PRINT *,"> Finished filling file arrays."

        !Get number of records read
        n1 = Count1 - 1
        n2 = Count2 - 1

        PRINT *,"> Iterating through first file."

        !Step through first file
        DO i2=1,n1
                first_one = File1First(i2)
                first_two = File1Second(i2)
                !Step through second file for a match
                DO i3=1,n2
                        second_one = File2First(i3)
                        second_two = File2Second(i3)
                        IF (second_two .EQ. first_two) THEN
                                added_num = first_one + second_one
                                !Write the match
                                WRITE(UNIT=30,FMT=300)added_num,second_two
300                             FORMAT(2x,e9.4,2x,f7.1)
                                found = "true"
                        END IF
```

```
            END DO

            !If no match, write the record from first file
            IF (found /= "true") THEN
                  WRITE(UNIT=30,FMT=300)first_one,first_two
            END IF
            found = "false"
      END DO

      PRINT *,"> Finished iterating through first file."

      PRINT *,"> Iterating through second file."

      found = "false"

      !Step through the second file
      DO i4=1,n2
            second_one = File2First(i4)
            second_two = File2Second(i4)
            !Step through the first file
            DO i5=1,n1
                  first_one = File1First(i5)
                  first_two = File1Second(i5)
                  IF (first_two .EQ. second_two) THEN
                        found = "true"
                  END IF
            END DO
            IF (found /= "true") THEN
                  WRITE(UNIT=30,FMT=300)second_one,second_two
            END IF
            found = "false"
      END DO

      PRINT *,"> Finished iterating through second file."

      !Finally, clean up.

      PRINT *,"> Cleaning up."

      CLOSE(10)
      CLOSE(20)
      CLOSE(30)

      PRINT *,"> DONE!"

      !STOP

END SUBROUTINE RunCalculation
```

The file ‘All.txt’ is listed below. The first two columns provide the names of the files that need to be summed and the third column gives the output file name resulting

from that addition step. The summed energy transfer probability is given in the file 'sum.out'.

All.txt

000.out	101.out	1.out	(Line 1)
1.out	111.out	2.out	(Line 2)
2.out	… ...	... ...	
... ...	... ...	... ...	
… ...	... ...	179.out	
179.out	18018.out	sum.out	(Line Final-1)
sum.out	00000.out	end.out	(Line Final)

A plot of the file 'sum.out' is the complete energy transfer probability distribution function P(ΔE). The P(ΔE) function for scatter HOD (000) after single collisions with highly vibrationally excited pyrazine molecules is shown in Figure D.1.

For calculating complete energy transfer probability distribution functions of scattered HOD (000) after single collisions with highly vibrationally excited 2-picoline and 2,6-lutidine molecules, parameters in the files 'water_gen_pyrazine.f90' and 'Allstate.txt' need to be changed accordingly. For calculating the complete energy transfer probability distribution functions of donor/H_2O, the file 'All.txt' also need to be modified. A summary of the measured translational and rotational temperatures is given in Table D.1. Measured energy transfer rates and calculated Lennard-Jones collision rates are also included. For H_2O, an assumption is made in order to get complete energy transfer probability function. This assumption is that low J states have the same rotational and translational distribution as the high J states, only based on strong collisional energy transfer data from experiments.

Table D.1. Summary of measured translational and rotational temperatures, collision rates and Lennard-Jones collision rates for donor/bath pairs.

Donor (E_{vib}) + Bath $\xrightarrow{k_2^J}$ Donor (E_{vib}-ΔE) + Bath (000, $J_{Ka,Kc}$)

Donor/Bath	T_{rot}, K	T_{rel}, K	k_{int} 10^{-9} cm^3 molecule^{-1} s^{-1}	k_{LJ} 10^{-10} cm^3 molecule^{-1} s^{-1}
Pyrazine/HOD	430	635	1.03	6.19
Picoline/HOD	440	678	1.57	6.44
Lutidine/HOD	369	625	2.18	6.86
Pyrazine/H_2O	920	636	0.79	6.33
Pyridine-h_5/H_2O	892	674	0.69	6.15
Pyridine-d_5/H_2O	891	531	0.73	6.12
Pyridine-f_5/H_2O	534	612	1.05	6.44
Picoline/H_2O	590	662	2.22	6.58
Lutidine/H_2O	490	635	5.04	7.02

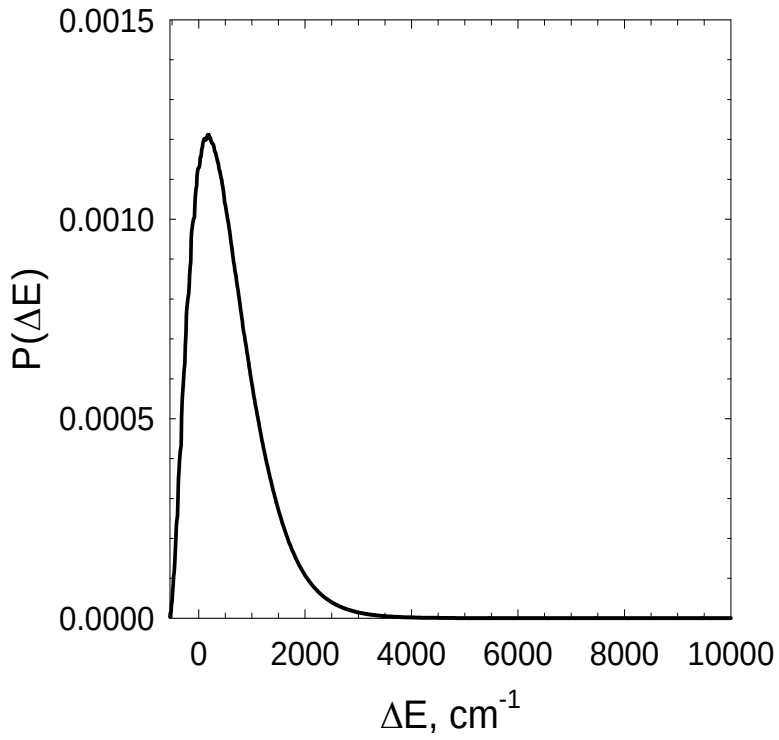

Figure D.1. Complete energy transfer probability function for scatter HOD (000) after single collisions with highly vibrationally excited pyrazine molecules.

Appendix E: Calculation of Energy Use in Reaction of Pyridine-d_5 + Cl

In the reaction of pyridine-d_5 (E_{vib}=38,068 cm^{-1}) with Cl, the average lab-frame velocity of DCl products, $\langle v_4 \rangle$, is calculated from Eq. E.1.

$$\langle v_4 \rangle = \sqrt{\frac{3kT_{trans,lab}}{m_4}} \qquad \text{(Eq. E.1)}$$

where m_4 is the mass of DCl product, k is the Boltzmann constant and T_{trans}(lab) is lab frame translational temperature. T_{trans}(lab) is determined from the measured linewidths for nascent DCl products.

As shown in Figure E.1, the relative velocity of the reaction products is the vector difference of the lab frame velocity vectors $\mathbf{v_3}$ and $\mathbf{v_4}$, where $\mathbf{v_3}$ is the velocity of pyridinyl-d_4 radical. The product relative velocity, v'_{rel} is calculated by Eq. E.2.

$$\langle v'_{rel} \rangle = \left(\left(\frac{m_1 \langle v_1 \rangle}{m_3} \right)^2 + \left(\frac{m_2 \langle v_2 \rangle}{m_3} \right)^2 + \langle v_4 \rangle^2 + \frac{m_4}{m_3} \langle v_4 \rangle^2 + f(\theta, \varphi) \right)^{1/2} \qquad \text{(Eq. E.2)}$$

where $f(\theta, \varphi)$ is the angle-dependent cross term. θ is defined as the angle of $\mathbf{v_1}$ and $\mathbf{v_2}$. φ is the angle of $\mathbf{v_3}$ and $\mathbf{v_4}$. Based on the assumption that the angular distributions are

isotropic, a numerical integration over θ and φ was performed. The value of f(θ, φ) is small and is only 0.5% of $\mathbf{v'_{rel}}$. It is therefore dropped out of the $\mathbf{v'_{rel}}$ calculation. In Eq. E.2, m_1, m_2 and m_3 are the masses of pyridine-d_5, Cl, and pyridinyl-d_4 radicals, respectively. $\mathbf{v_1}$ and $\mathbf{v_2}$ are the velocities of pyridine-d_5 and chlorine radical. The spread in $\mathbf{v'_{rel}}$ include the velocity spread in $\mathbf{v_1}$, $\mathbf{v_2}$ and $\mathbf{v_4}$.

The spread in velocity of the DCl product, $\mathbf{v_4}$, is determined by the uncertainty of Doppler-broadened linewidths measurement as shown in Table 6.3 in Chapter 6. The velocity spread of pyridine-d_5 (298K) is determined by a Maxwell-Boltzmann distribution in Eq. E.3.

$$P(E) = 4\pi\left(\frac{m_1}{2\pi k_B T}\right)^{\frac{3}{2}} \frac{E}{m_1} e^{-\left(\frac{E}{k_B T}\right)} \qquad \text{(Eq. E.3)}$$

Here E is the translational energy of pyridine-d_5 molecule and T=298 K. The translational energy distribution of pyridine-d_5 is shown in Figure E.2. The average translational energy is $\langle E_{trans}\rangle$=313 cm^{-1}. To account for 70% of pyridine-d_5 molecules, the spread in energy is $\langle \Delta E_{trans}\rangle$=230 cm^{-1}. This corresponds to a velocity of $\langle v_1\rangle$=297±110 m/s. The method for determining the velocity spread of Cl from 355 nm photodissociation of Cl_2 is given by Zare and coworkers.[189] Figure E.3 shows the translational energy distribution of Cl after 355 nm photodissociation of Cl_2. This distribution is fit to a Gaussian function to obtain the most probable energy value and its spread. The translational energy of Cl is $\langle E_{Cl}\rangle$=4182±921 cm^{-1}. This corresponds to a velocity of $\langle v_2\rangle$=1674±184 m/s. We also note that the ^{35}Cl and ^{37}Cl have different

velocities from photodissociation. The natural abundance ratio of $^{35}Cl^{35}Cl$, $^{35}Cl^{37}Cl$ and $^{37}Cl^{37}Cl$ is 9:6:1. However, this velocity difference is less that 5% of the $\mathbf{v_2}$ values and is neglected in our calculation. Only the translational energy of ^{35}Cl for dissociation of $^{35}Cl^{35}Cl$ is considered.

The energy used, E_{used}, is defined as the vibrational energy used for the reaction. E_{used} is calculated from Eq. E.4.

$$E_{used} = E_{rel} + E_{vib} + E_{rot,pyridine-d5} - \Delta H - E'_{rel} - E'_{rot,DCl} - E_{rot,pyridinyl-d4} \qquad \text{(Eq. E.4)}$$

where rotational energy of pyridine-d_5 molecules and pyridinyl-d_4 radicals, $E_{rot,pyridine-d5}$ and $E_{rot,pyridinyl-d4}$, are assumed to be approximately the same based on the collinear D-atom abstraction reaction mechanism. The relative translational energy E_{rel} is determined from $E_{rel} = \frac{\mu v_{rel}^2}{2}$, where the reduced mass of reactant is $\mu = \frac{m_1 m_2}{m_1 + m_2}$, $\langle v_{rel} \rangle = \sqrt{\langle v_1 \rangle^2 + \langle v_2 \rangle^2}$ and ΔH is the enthalpy of reaction. Abstraction can occur from different C-D sites on pyridine-d_5 molecules. For breaking meta- and para- C-D bonds, ΔH=3065 cm^{-1}, while for breaking the ortho- C-D bond, ΔH=610 cm^{-1}.[179] The product relative translational energy is $E'_{rel} = \frac{\mu' v'^2_{rel}}{2}$, where $\mu' = \frac{m_3 m_4}{m_3 + m_4}$, and The vibrational energy in pyridine-d_5 is E_{vib}=38,068 cm^{-1}.

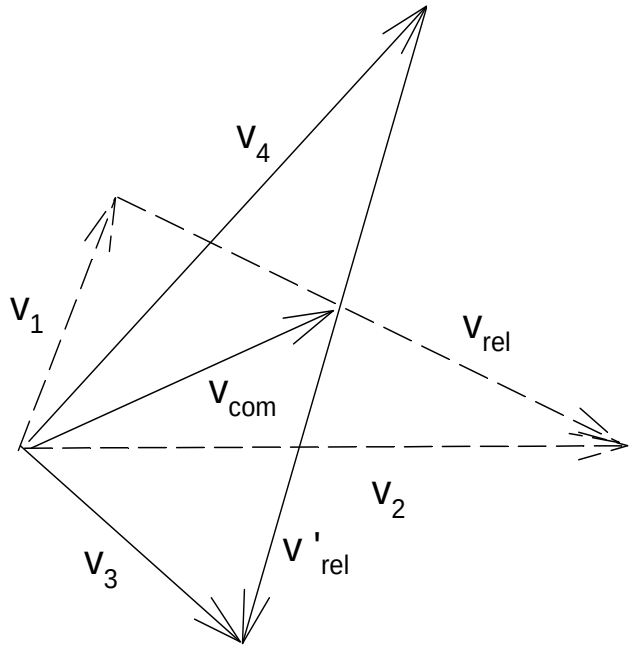

Figure E.1. Newton Diagram of the reaction of pyridine-d_5 with Cl. $\mathbf{v_1}$ and $\mathbf{v_2}$ stand for the velocity of room temperature pyridine-d_5 and the velocity of Cl after 355 nm dissociation, respectively. The angle between $\mathbf{v_1}$ and $\mathbf{v_2}$ is θ. Their relative velocity is $\mathbf{v_{rel}}$. The velocity of pyridinyl-d_4 radical after the reaction is $\mathbf{v_3}$, and the velocity of DCl measured from the Doppler-broadened linewidths is $\mathbf{v_4}$. The angle between $\mathbf{v_3}$ and $\mathbf{v_4}$ is ϕ. The relative velocity of the reaction products is $\mathbf{v'_{rel}}$. $\mathbf{v_{com}}$ is the center of mass velocity. In this case the vector of center of mass velocity does not change before and after the D-atom abstraction reactions.

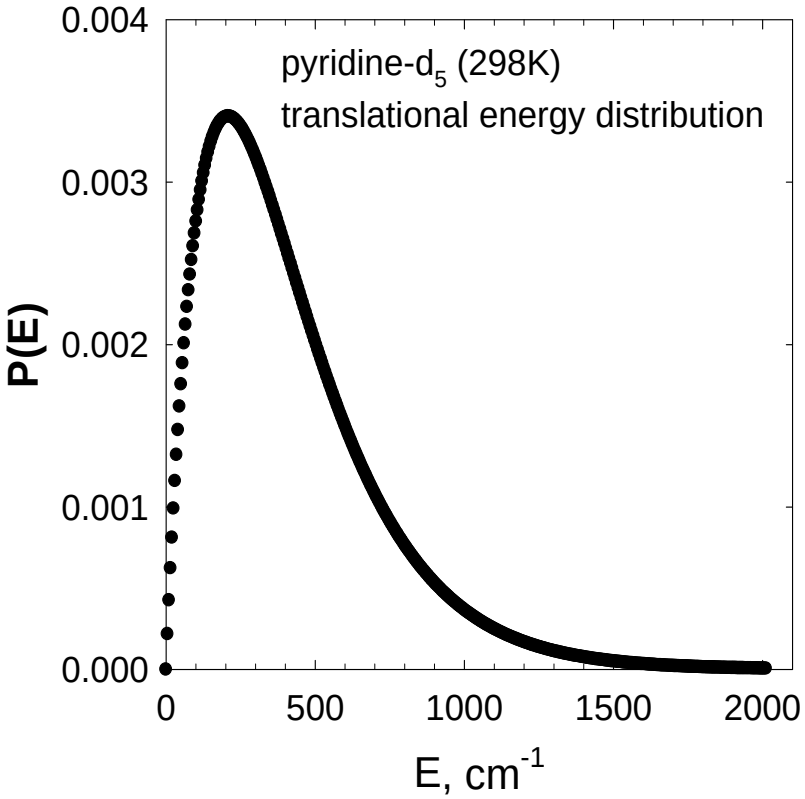

Figure E.2. Translational energy distribution of room temperature pyridine-d_5 molecules.

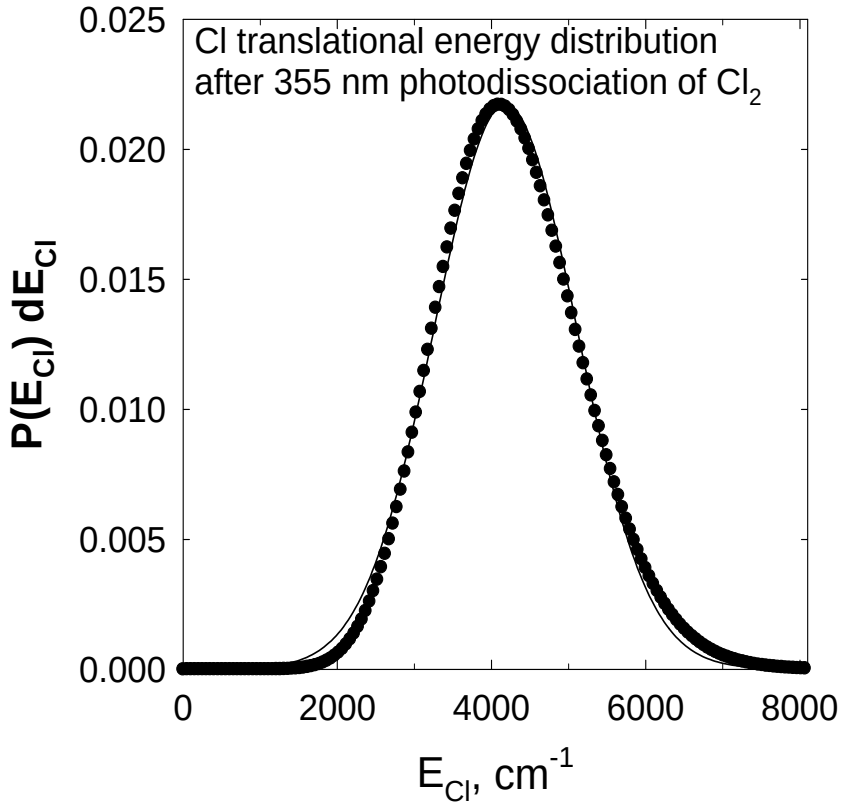

Figure E.3. Translational energy distribution of Cl after 355 nm photodissociation. A Gaussian function fitting is shown by the solid line.

References

(1) Weston, R. E., Jr.; Flynn, G. W. *Annu. Rev. Phys. Chem.* **1992**, *43*, 559-589.

(2) Oref, I.; Tardy, D. C. *Chem. Rev.* **1990**, *90*, 1407-1445.

(3) Krajnovich, D. J.; Parmenter, C. S.; Catlett, D. L. *Chem. Rev.* **1987**, *87*, 237-288.

(4) Robinson, P. J.; Holbrook, K. A. *Unimolecular Reactions*; Wiley-Interscience: London, 1972.

(5) Rossi, M. J.; Pladziewicz, J. R.; Barker, J. R. *J. Chem. Phys.* **1983**, *78*, 6695-6708.

(6) Barker, J. R.; Golden, R. E. *J. Phys. Chem.* **1984**, *88*, 1012-1017.

(7) Shi, J.; Barker, J. R. *J. Chem. Phys.* **1988**, *88*, 6219-6227.

(8) Troe, J. *J. Chem. Phys.* **1992**, *97*, 288-292.

(9) Hippler, H.; Otto, B.; Troe, J. *Ber. Bunsen-Ges. Phys. Chem. Chem. Phys.* **1989**, *93*, 428-434.

(10) Hartland, G. V. Q., D.; Dai, H. L. *J. Chem. Phys.* **1995**, *102*, 8677.

(11) Liu, C. L.; Hsu, H. C.; Lyu, J. J.; Ni, C. K. *J. Chem. Phys.* **2005**, *123*, 131102.

(12) Liu, C. L.; Hsu, H. C.; Lyu, J. J.; Ni, C. K. *J. Chem. Phys.* **2006**, *124*, 054302.

(13) Liu, C. L.; Hsu, H. C.; Ni, C. K. *Phys. Chem. Chem. Phys.* **2005**, *7*, 2151-2155.

(14) Luther, K.; Reihs, K. *Ber. Bunsen-Ges. Phys. Chem. Chem. Phys.* **1988**, *92*, 442-445.

(15) Lenzer, T.; Luther, K.; Reihs, K.; Symonds, A. C. *J. Chem. Phys.* **2000**, *112*, 4090-4110.

(16) Hold, U.; Lenzer, T.; Luther, K.; Symonds, A. C. *J. Chem. Phys.* **2003**, *119*, 11192-11211.

(17) Grigoleit, U.; Lenzer, T.; Luther, K. *Z. Phys. Chem. (Muenchen, Ger.)* **2000**, *214*, 1065-1085.

(18) Lenzer, T.; Luther, K.; Reihs, K.; Symonds, A. C. *J. Chem. Phys.* **2000**, *112*, 4090-4110.

(19) Hold, U.; Lenzer, T.; Luther, K.; Reihs, K.; Symonds, A. C. *J. Chem. Phys.* **2000**, *112*, 4076-4089.

(20) Hold, U.; Lenzer, T.; Luther, K.; Symonds, A. C. *J. Chem. Phys.* **2003**, *119*, 11192-11211.

(21) Elioff, M. S.; Fang, M.; Mullin, A. S. *J. Chem. Phys.* **2001**, *115*, 6990-7001.

(22) Elioff, M. S.; Fang, M.; Mullin, A. S. *J. Chem. Phys.* **2002**, *117*, 6880-6880.

(23) Park, J.; Shum, L.; Lemoff, A. S.; Werner, K.; Mullin, A. S. *J. Chem. Phys.* **2002**, *117*, 5221-5233.

(24) Miller, E. M.; Murat, L.; Bennette, N.; Hayes, M.; Mullin, A. S. *J. Phys. Chem. A* **2006**, *110*, 3266-3272.

(25) Kohlmaier, G. H.; Rabinovitch, B. S. *J. Chem. Phys.* **1963**, *38*, 1692-1708.

(26) Kohlmaier, G. H.; Rabinovitch, B. S. *J. Chem. Phys.* **1963**, *38*, 1709-1714.

(27) Simons, J. W.; Rabinovitch, B. S.; Setser, D. W. *J. Chem. Phys.* **1964**, *41*, 800-805.

(28) Tardy, D. C.; Rabinovitch, B. S.; Larson, C. W. *J. Chem. Phys.* **1966**, *45*, 1163-1172.

(29) Troe, J. *J. Chem. Phys.* **1977**, *66*, 4745-4757.

(30) Borjesson, L. E. B.; Nordholm, S. *J. Phys. Chem.* **1995**, *99*, 938-944.

(31) Borjesson, L. E. B.; Nordholm, S.; Andersson, L. L. *Chem. Phys. Lett.* **1991**, *186*, 65-72.

(32) Nordholm, S.; Freasier, B. C.; Jolly, D. L. *Chem. Phys.* **1977**, *25*, 433-449.

(33) Nilsson, D.; Nordholm, S. *J. Chem. Phys.* **2003**, *119*, 11212-11220.

(34) Lenzer, T.; Luther, K.; Nilsson, D.; Nordholm, S. *J. Phys. Chem. B* **2005**, *109*, 8325-8331.

(35) Nilsson, D.; Nordholm, S. *J. Phys. Chem. A* **2006**, *110*, 3289-3296.

(36) Brown, N. J.; Miller, J. A. *J. Chem. Phys.* **1984**, *80*, 5568-5580.

(37) Schranz, H. W. *Theochem - J. Mol. Struc.* **1996**, *368*, 119-124.

(38) Whyte, A. R.; Lim, K. F.; Gilbert, R. G.; Hase, W. L. *Chem. Phys. Lett.* **1988**, *152*, 377-381.

(39) Schranz, H. W.; Troe, J. *J. Phys. Chem.* **1986**, *90*, 6168-6175.

(40) Barker, J. R.; Yoder, L. M.; King, K. D. *J. Phys. Chem. A* **2001**, *105*, 796-809.

(41) Clarke, D. L.; Oref, I.; Gilbert, R. G.; Lim, K. F. *J. Chem. Phys.* **1992**, *96*, 5983-5998.

(42) Clarke, D. L.; Thompson, K. C.; Gilbert, R. G. *Chem. Phys. Lett.* **1991**, *182*, 357-362.

(43) Clary, D. C.; Gilbert, R. G.; Bernshtein, V.; Oref, I. *Faraday Discuss.* **1995**, 423-433.

(44) Lenzer, T.; Luther, K.; Troe, J.; Gilbert, R. G.; Lim, K. F. *J. Chem. Phys.* **1995**, *103*, 626-641.

(45) Bruehl, M.; Schatz, G. C. *J. Phys. Chem.* **1988**, *92*, 7223-7229.

(46) Schatz, G. C.; Lendvay, G. *J. Chem. Phys.* **1997**, *106*, 3548-3557.

(47) Lendvay, G.; Schatz, G. C. *J. Phys. Chem.* **1991**, *95*, 8748-8753.

(48) Brunsvold, A. L.; Garton, D. J.; Minton, T. K.; Troya, D.; Schatz, G. C. *J. Chem. Phys.* **2004**, *121*, 11702-11714.

(49) Bernshtein, V.; Oref, I. *Chem. Phys. Lett.* **1999**, *300*, 104-108.

(50) Bernshtein, V.; Oref, I. *J. Phys. Chem. A* **2001**, *105*, 10646-10650.

(51) Bernshtein, V.; Oref, I. *J. Chem. Phys.* **2003**, *118*, 10611-10622.

(52) Lim, K. F. *J. Chem. Phys.* **1994**, *101*, 8756-8767.

(53) Lim, K. F. *J. Chem. Phys.* **1994**, *100*, 7385-7399.

(54) Linhananta, A.; Lim, K. F. *Phys. Chem. Chem. Phys.* **2002**, *4*, 577-585.

(55) Bernshtein, V.; Oref, I. *J. Phys. Chem. B* **2005**, *109*, 8310-8319.

(56) Grigoleit, U.; Lenzer, T.; Luther, K.; Mutzel, M.; Takahara, A. *Phys. Chem. Chem. Phys.* **2001**, *3*, 2191-2202.

(57) Lenzer, T.; Luther, K. *J. Chem. Phys.* **1996**, *104*, 3391-3394.

(58) Higgins, C.; Ju, Q.; Seiser, N.; Flynn, a. G. W.; Chapman, S. *J. Phys. Chem. A* **2001**, *105*, 2858-2866.

(59) Higgins, C. J.; Chapman, S. *J. Phys. Chem. A* **2004**, *108*, 8009-8018.

(60) Yoder, L. M.; Barker, J. R. *J. Phys. Chem. A* **2000**, *104*, 10184-10193.

(61) Sushida, K.; Fujita, M.; Yamazaki, I.; Baba, H. *Bull. Chem. Soc. Jpn.* **1983**, *56*, 2228-2233.

(62) Yamazaki, I.; Murao, T.; Yamanaka, T.; Yoshihara, K. *Faraday Trans. Chem. Soc.* **1983**, 395-405.

(63) Yamazaki, I.; Sushida, K.; Baba, H. *J. Chem. Phys.* **1979**, *71*, 381-387.

(64) Nelson, D. D., Jr.; Schiffman, A.; Lykke, K. R.; Nesbitt, D. J. *Chem. Phys. Lett.* **1988**, *153*, 105-111.

(65) Miller, J. A.; Pilling, M. J.; Troe, E. *P. Combust. Inst.* **2005**, *30*, 43-88.

(66) Fernandez-Ramos, A.; Miller, J. A.; Klippenstein, S. J.; Truhlar, D. G. *Chem. Rev.* **2006**, *106*, 4518-4584.

(67) DeSain, J. D.; Klippenstein, S. J.; Miller, J. A.; Taatjes, C. A. *J. Phys. Chem. A* **2003**, *107*, 4415-4427.

(68) DeSain, J. D.; Taatjes, C. A.; Miller, J. A.; Klippenstein, S. J.; Hahn, D. K. *Faraday Discuss.* **2001**, *119*, 101-120.

(69) Walker, R. W.; Morley, C. In *Low Temperature Combustion and Autoignition*; Pilling, M. J., Ed.; Elsevier: Amsterdam, 1997.

(70) Tardy, D. C.; Song, B. H. *J. Phys. Chem.* **1993**, *97*, 5628-5632.

(71) Toselli, B. M.; Barker, J. R. *J. Chem. Phys.* **1992**, *97*, 1809-1817.

(72) Linhananta, A.; Lim, K. F. *Phys. Chem. Chem. Phys.* **1999**, *1*, 3467-3471.

(73) Linhananta, A.; Lim, K. F. *Phys. Chem. Chem. Phys.* **2000**, *2*, 1385-1392.

(74) Bernshtein, V.; Oref, I. *J. Phys. Chem. A* **2006**, *110*, 1541-1551.

(75) Bernshtein, V.; Oref, I. *J. Phys. Chem. A* **2006**, *110*, 8477-8487.

(76) Yuan, L. W.; Du, J.; Mullin, A. S. *J. Chem. Phys.* **2008**, *129*, 014303.

(77) Liu, Q.; Du, J.; Havey, D. K.; Li, Z.; Miller, E. M.; Mullin, A. S. *J. Phys. Chem. A* **2007**, *111*, 4073-4080.

(78) Yamazaki, I.; Murao, T.; Yoshihara, K.; Fujita, M.; Sushida, K.; Baba, H. *Chem. Phys. Lett.* **1982**, *92*, 421-424.

(79) Michaels, C. A.; Flynn, G. W. *J. Chem. Phys.* **1997**, *106*, 3558-3566.

(80) Roney, P. L.; Findlay, F. D.; Buijs, H. L.; Cann, M. W. P.; Nicholls, R. W. *Appl. Opt.* **1978**, *17*, 2599-2604.

(81) Rothman, L. S.; Jacquemart, D.; Barbe, A.; Benner, D. C.; Birk, M.; Brown, L. R.; Carleer, M. R.; Chackerian, C.; Chance, K.; Coudert, L. H.; Dana, V.; Devi, V. M.; Flaud, J. M.; Gamache, R. R.; Goldman, A.; Hartmann, J. M.; Jucks, K. W.; Maki, A. G.; Mandin, J. Y.; Massie, S. T.; Orphal, J.; Perrin, A.; Rinsland, C. P.; Smith, M. A. H.; Tennyson, J.; Tolchenov, R. N.; Toth, R. A.; Vander Auwera, J.; Varanasi, P.; Wagner, G. *J. Quant. Spectrosc. Radiat. Transfer* **2005**, *96*, 139-204.

(82) Michaels, C. A.; Lin, Z.; Mullin, A. S.; Tapalian, H. C.; Flynn, G. W. *J. Chem. Phys.* **1997**, *106*, 7055-7071.

(83) Lenzer, T.; Luther, K. *J. Chem. Phys.* **1996**, *105*, 10944-10953.

(84) Stein, S. E.; Rabinovitch, B. S. *J. Chem. Phys.* **1973**, *58*, 2438-2445.

(85) Green, J. H. S.; Barnard, P. W. B. *J. Chem. Soc.* **1963**, 640-643.

(86) Werner, H.-J.; Knowles, P. J.; Lindh, R.; Manby, F. R.; Schutz, M.; Celani, P.; Korona, T.; Rauhut, G.; Amos, R. D.; Bernhardsson, A.; Berning, A.; Cooper, D. L.; Deegan, M. J. O.; Dobbyn, A. J.; Eckert, F.; Hampel, C.; Hetzer, G.; Lloyd, A. W.; McNicholas, S. J.; Meyer, W.; Mura, M. E.; Nicklass, A.; Palmieri, P.; Schumann, U.; Stoll, H.; Stone, A. J.; Tarroni, R.; T. Thosteinsson, v. MOLPRO, a package of ab initio programs.

(87) Draeger, J. A. *Spectrochim. Acta, Part A* **1985**, *41A*, 607-627.

(88) Baer, T.; Hase, W. L. *Unimolecular Reaction Dynamics: Theory and Experiments*; Oxford University Press: New York, 1996.

(89) Guckian, K. M.; Schweitzer, B. A.; Ren, R. X. F.; Sheils, C. J.; Tahmassebi, D. C.; Kool, E. T. *J. Am. Chem. Soc.* **2000**, *122*, 2213-2222.

(90) Hunter, C. A. *Chem. Soc. Rev.* **1994**, *23*, 101-109.

(91) Coates, G. W.; Dunn, A. R.; Henling, L. M.; Dougherty, D. A.; Grubbs, R. H. *Angew. Chem., Int. Ed. Engl.* **1997**, *36*, 248-251.

(92) Nadykto, A. B.; Yu, F. Q. *Chem. Phys. Lett.* **2007**, *435*, 14-18.

(93) Aloisio, S.; Hintze, P. E.; Vaida, V. *J. Phys. Chem. A* **2002**, *106*, 363-370.

(94) Smith, I. W. M.; Ravishankara, A. R. *J. Phys. Chem. A* **2002**, *106*, 4798-4807.

(95) Caminati, W.; Favero, L. B.; Favero, P. G.; Maris, A.; Melandri, S. *Angew. Chem., Int. Ed.* **1998**, *37*, 792-795.

(96) Havey, D. K.; Liu, Q.; Li, Z.; Elioff, M.; Mullin, A. S. *J. Phys. Chem. A* **2007**, *111*, 13321-13329.

(97) Havey, D. K.; Liu, Q.; Li, Z.; Elioff, M.; Fang, M.; Neudel, J.; Mullin, A. S. *J. Phys. Chem. A*. **2007**, *111*, 2458-2460.

(98) Danten, Y.; Tassaing, T.; Besnard, M. *J. Phys. Chem. A* **1999**, *103*, 3530-3534.

(99) Alkorta, I.; Rozas, I.; Elguero, J. *J. Fluorine Chem.* **2000**, *101*, 233-238.

(100) Rozas, I.; Alkorta, I.; Elguero, J. *J. Phys. Chem. A* **1997**, *101*, 9457-9463.

(101) Furutaka, S.; Ikawa, S. *J. Chem. Phys.* **2002**, *117*, 751-755.

(102) Atwood, J. L.; Hamada, F.; Robinson, K. D.; Orr, G. W.; Vincent, R. L. *Nature* **1991**, *349*, 683-684.

(103) Suzuki, S.; Green, P. G.; Bumgarner, R. E.; Dasgupta, S.; Goddard, W. A.; Blake, G. A. *Science* **1992**, *257*, 942-944.

(104) Engdahl, A.; Nelander, B. *J. Phys. Chem.* **1987**, *91*, 2253-2258.

(105) Gotch, A. J.; Zwier, T. S. *J. Chem. Phys.* **1992**, *96*, 3388-3401.

(106) Wormald, C. J.; Wurzberger, B. *Phys. Chem. Chem. Phys.* **2000**, *2*, 5133-5137.

(107) Elioff, M. S.; Fraelich, M.; Sansom, R. L.; Mullin, A. S. *J. Chem. Phys.* **1999**, *111*, 3517-3525.

(108) Liu, Q.; Havey, D. K.; Mullin, A. S. *J. Phys. Chem. A* **2008**, *112*, 9509-9515.

(109) Villa, E.; Amirav, A.; Lim, E. C. *J. Phys. Chem.* **1988**, *92*, 5393-5397.

(110) Alani, K.; Phillips, D. *J. Phys. Chem.* **1970**, *74*, 4046-4052.

(111) Wong, K. N.; Colson, S. D. *J. Mol. Spectrosc.* **1984**, *104*, 129-151.

(112) Long, D. A.; Steele, D. *Spectrochimi. Acta.* **1963**, *19*, 1791-1795.

(113) Romanini, D.; Lehmann, K. K. *J. Chem. Phys.* **1993**, *98*, 6437-6444.

(114) Maris, A.; Favero, L. B.; Danieli, R.; Favero, P. G.; Caminati, W. *J. Chem. Phys.* **2000**, *113*, 8567-8573.

(115) Mitchell, D. G.; Johnson, A. M.; Johnson, J. A.; Judd, K. A.; Kim, K.; Mayhew, M.; Powell, A. L.; Sevy, E. T. *J. Phys. Chem. A* **2008**, *111*, 13330-13338.

(116) Wu, F.; Weisman, R. B. *J. Chem. Phys.* **1999**, *110*, 5047-5055.

(117) Mullin, A. S.; Michaels, C. A.; Flynn, G. W. *J. Chem. Phys.* **1995**, *102*, 6032-6045.

(118) Wall, M. C.; Mullin, A. S. *J. Chem. Phys.* **1998**, *108*, 9658-9667.

(119) Clarkson, J. R.; Baquero, E.; Shubert, V. A.; Myshakin, E. M.; Jordan, K. D.; Zwier, T. S. *Science* **2005**, *307*, 1443-1446.

(120) Cottrell, T. L.; McCoubrey, J. C. *Molecular Energy Transfer in Gases*; Butterworths, 1961.

(121) Keeton, R. G.; Bass, H. E. *J. Acoust. Soc. Am.* **1976**, *60*, 78-82.

(122) Yardley, J. T. *Introduction to Molecular Energy Transfer*; Academic Press Inc., 1980.

(123) Sharma, R. D.; Brau, C. A. *J. Chem. Phys.* **1969**, *50*, 924-&.

(124) Sharma, R. D. *Phys. Rev.* **1969**, *177*, 102-107.

(125) Elioff, M. S.; Sansom, R. L.; Mullin, A. S. *J. Phys. Chem. A* **2000**, *104*, 10304-10311.

(126) Zarembowitch, J.; Bokobza-Sebagh, L. *Spectrochim. Acta, Part A* **1976**, *32A*, 605-615.

(127) Orchard, S. W.; Ramsden, J. *Int. J. Chem. Kinet.* **1982**, *14*, 43-53.

(128) Rizzo, T. R.; Crim, F. F. *J. Chem. Phys.* **1982**, *76*, 2754-2756.

(129) Larson, C. W.; Rabinovitch, B. S. *J. Chem. Phys.* **1969**, *51*, 2293-2308.

(130) Barker, J. R.; Toselli, B. M. *Int. Rev. Phys. Chem.* **1993**, *12*, 305-338.

(131) Heymann, M.; Hippler, H.; Plach, H. J.; Troe, J. *J. Chem. Phys.* **1987**, *87*, 3867-3874.

(132) Rossi, M. J.; Pladziewicz, J. R.; Barker, J. R. *J. Chem. Phys.* **1983**, *78*, 6695-6708.

(133) Ashfold, M. N. R.; Baggott, J. E. *Advances in Gas-Phase Photochemistry and Kinetics: Bimolecular Collisions*; Science and Behavior Books: Palo Alto, 1989.

(134) Toselli, B. M.; Walunas, T. L.; Barker, J. R. *J. Chem. Phys.* **1990**, *92*, 4793-4804.

(135) Yerram, M. L.; Brenner, J. D.; King, K. D.; Barker, J. R. *J. Phys. Chem.* **1990**, *94*, 6341-6350.

(136) Fraelich, M.; Elioff, M. S.; Mullin, A. S. *J. Phys. Chem. A* **1998**, *102*, 9761-9771.

(137) Michaels, C. A.; Mullin, A. S.; Park, J.; Chou, J. Z.; Flynn, G. W. *J. Chem. Phys.* **1998**, *108*, 2744-2755.

(138) Elioff, M. S.; Wall, M. C.; Lemoff, A. S.; Mullin, A. S. *J. Chem. Phys.* **1999**, *110*, 5578-5588.

(139) Li, Z. M.; Korobkova, E.; Werner, K.; Shum, L.; Mullin, A. S. *J. Chem. Phys.* **2005**, *123*, 174306.

(140) Sevy, E. T.; Lin, Z.; Flynn, G. W. *Abstr. Papers Am. Chem. Soc.* **1997**, *214*, 4-PHYS.

(141) Luther, K.; Reihs, K. *Ber. Bunsen-Ges. Phys. Chem. Chem. Phys.* **1988**, *92*, 442-445.

(142) Chan, S. C.; Rabinovitch, B. S.; Bryant, J. T.; Spicer, L. D.; Fujimoto, T.; Lin, Y. N.; Pavlou, S. P. *J. Phys. Chem.* **1970**, *74*, 3160-3176.

(143) Lendvay, G.; Schatz, G. C. *J. Phys. Chem.* **1992**, *96*, 3752-3756.

(144) Utz, A. L.; Tobiason, J. D.; Carrasquillo, E.; Fritz, M. D.; Crim, F. F. *J. Chem. Phys.* **1992**, *97*, 389-396.

(145) Troe, J. *J. Chem. Phys.* **1977**, *66*, 4758-4775.

(146) Snavely, D. L.; Zare, R. N.; Miller, J. A.; Chandler, D. W. *J. Phys. Chem.* **1986**, *90*, 3544-3549.

(147) Barrett, J. C. *J. Chem. Phys.* **2007**, *126*, 074312.

(148) Barrett, J. C. *J. Chem. Phys.* **2002**, *116*, 8856-8862.

(149) Ford, I. J. *Proc. Inst. Mech. Eng. C, J. Mech. Eng. Sci.* **2004**, *218*, 883-899.

(150) Oxtoby, D. W. *J. Phys.: Condens. Matter* **1992**, *4*, 7627-7650.

(151) Hirschfelder, J. O.; Curtiss, C. F.; Bird, R. B. *Molecular Theory of Gases and Liquids*; John Wiley and Sons: New York, 1964.

(152) Xue, B.; Han, J.; Dai, H.-L. *Phys. Rev. Lett.* **2000**, *84*, 2606-2609.

(153) Durant, J. L.; Kaufman, F. *Chem. Phys. Lett.* **1987**, *142*, 246.

(154) Hinchen, J. J.; Hobbs, R. H. *J. Chem. Phys.* **1976**, *65*, 2732-2739.

(155) Mourits, F. M.; Rummens, F. H. A. *Can. J. Chem.* **1977**, *55*, 3007.

(156) Whetton, N. T.; Lawrance, W. D. *J. Phys. Chem.* **1992**, *96*, 3717-3723.

(157) Tasic, U. S.; Parmenter, C. S. *J. Phys. Chem. B* **2004**, *108*, 10325-10333.

(158) Michael, J. V.; Su, M. C.; Sutherland, J. W.; Carroll, J. J.; Wagner, A. F. *J. Phys. Chem. A* **2002**, *106*, 5297-5313.

(159) Sushida, K.; Yamazaki, I.; Baba, H. *Oyo Denki Kenkyusho Hokoku* **1980**, *32*, 36-44.

(160) Pyper, J. W.; Christensen, L. D. *J. Chem. Phys.* **1975**, *62*, 2596-2599.

(161) Wall, M. C.; Stewart, B. A.; Mullin, A. S. *J. Chem. Phys.* **1998**, *108*, 6185-6196.

(162) Miller, L. A.; Barker, J. R. *J. Chem. Phys.* **1996**, *105*, 1383-1391.

(163) Simpson, W. R.; Rakitzis, T. P.; Kandel, S. A.; Lev-On, T.; Zare, R. N. *J. Phys. Chem.* **1996**, *100*, 7938-7947.

(164) Zhou, J. G.; Lin, J. J.; Zhang, B. L.; Liu, K. P. *J. Phys. Chem. A* **2004**, *108*, 7832-7836.

(165) Kim, Z. H.; Alexander, A. J.; Bechtel, H. A.; Zare, R. N. *J. Chem. Phys.* **2001**, *115*, 179-183.

(166) Kim, Z. H.; Bechtel, H. A.; Zare, R. N. *J. Am. Chem. Soc.* **2001**, *123*, 12714-12715.

(167) Kandel, S. A.; Rakitzis, T. P.; Lev-On, T.; Zare, R. N. *Chem. Phys. Lett.* **1997**, *265*, 121-128.

(168) Yan, S.; Wu, Y. T.; Zhang, B. L.; Yue, X. F.; Liu, K. P. *Science* **2007**, *316*, 1723-1726.

(169) Bechtel, H. A.; Camden, J. P.; Brown, D. J. A.; Martin, M. R.; Zare, R. N.; Vodopyanov, K. *Angew. Chem., Int. Ed.* **2005**, *44*, 2382-2385.

(170) Thoemke, J. D.; Pfeiffer, J. M.; Metz, R. B.; Crim, F. F. *J. Phys. Chem.* **1995**, *99*, 13748-13754.

(171) Simpson, W. R.; Rakitzis, T. P.; Kandel, S. A.; Orrewing, A. J.; Zare, R. N. *J. Chem. Phys.* **1995**, *103*, 7313-7335.

(172) Kim, Z. H.; Bechtel, H. A.; Camden, J. P.; Zare, R. N. *J. Chem. Phys.* **2005**, *122*, 084303.

(173) Polanyi, J. C. *Acc. Chem. Res.* **1972**, *5*, 161-168.

(174) Nesbitt, D. J.; Field, R. W. *J. Phys. Chem.* **1996**, *100*, 12735-12756.

(175) Parekunnel, T.; Hirao, T.; Le Roy, R. J.; Bernath, P. F. *J. Mol. Spectrosc.* **1999**, *195*, 185-191.

(176) Kim, Z. H.; Bechtel, H. A.; Zare, R. N. *J. Chem. Phys.* **2002**, *117*, 3232-3242.

(177) Park, J. H.; Lee, Y. S.; Hershberger, J. F.; Hossenlopp, J. M.; Flynn, G. W. *J. Am. Chem. Soc.* **1992**, *114*, 58-63.

(178) Zhao, Z.; Huskey, D. T.; Olsen, K. J.; Nicovich, J. M.; McKee, M. L.; Wine, P. H. *Phys. Chem. Chem. Phys.* **2007**, *9*, 4383-4394.

(179) Kiefer, J. H.; Zhang, Q.; Kern, R. D.; Yao, J.; Jursic, B. *J. Phys. Chem. A* **1997**, *101*, 7061-7073.

(180) Bergeat, A.; Cavagnat, D.; Lapouge, C.; Lespade, L. *J. Phys. Chem. A* **2000**, *104*, 9233-9243.

(181) Dreizler, H.; Rudolph, H. D.; Maeder, H. *Z. Naturforsch., A: Phys. Sci.* **1970**, *25*, 25-35.

(182) Long, D. A.; George, W. O. *Spectrochimi. Acta.* **1963**, *19*, 1777-1790.

(183) Yoshikai, K.; Hieida, T.; Nibu, Y.; Shimada, H.; Shimada, R. *Bull. Chem. Soc. Jpn.* **1990**, *63*, 1529-1531.

(184) Herzberg, G. *Electronic Spectra and Electronic Structure of Polyatomic Molecules (Molecular Spectra and Molecular Structure, Vol. III*; Van Nostrand Reinhold Company Inc., 1966.

(185) Kasper, J. V. V.; Pollock, C. R.; Curl, R. F.; Tittel, F. K. *Appl. Opt.* **1982**, *21*, 236-247.

(186) Lim, K. F. *Quantum Chem. Program Exchange Bull.* **1994**, *14*, 3.

(187) Mcquarrie, D. A. *Statistical Mechanics*; University Science Books: New York, 2000.

(188) Lide, D. R. *CRC Handbook of Chemistry and Physics*; CRC Press Inc., 2004-2005.

(189) Van der Zande, W. J.; Zhang, R.; Zare, R. N.; McKendrick, K. G.; Valentini, J. J. *J. Phys. Chem.* **1991**, *95*, 8205-8207.